In situ Observation of Surface Atoms/Molecules and their Dynamic Chemical Processes on a $TiO_2(110)$ Single Crystal Oxide Surface by Means of Scanning Tunneling Microscopy

By Shushi Suzuki

A Thesis Submitted to The University of Tokyo in Fulfillment
of the Requirements for the Degree of Doctor of Science

December, 1999

Contents

Chapter 1 General Introduction 1

Chapter 2 Experimental 37

Chapter 6 Direct viewing of surface acidity of $TiO_2(110)$ by in situ STM Observation of Adsorbed Ammonia 98

Chapter 7 The Condensation Reaction of Pyridine on $TiO_2(110)$: STM Observation in the Presence of the Reactant Atmosphere 121

Chapter 8 Hydrogen Adatoms on $TiO_2(110)$-(1x1) Characterized by Scanning Tunneling Microscopy and Electron Stimulated Desorption 134

Chapter 9 Concluding Remarks 147

Acknowledgment 150

Chapter 1

General Introduction

1.1 Introduction

One major objective of surface science is characterizing and improving the surface reactions of heterogeneous catalysts, where structural, chemical, and electronic properties are of crucial importance. The heterogeneous catalysts are, however, complex; polycrystalline materials such as metal supported oxides. Their inherent inhomogeneity in catalysts brings much difficulty of identification of the surface properties for catalytic performance. For example, interaction between metal and oxide of a metal supported oxide catalyst can enhance the reactivity in many cases, however the role of the metal and the support, and their interface is not well understood. While acid-base property or oxidation-reduction property of the surface is conventionally used as an indicator of the catalytic performance of metal oxide catalysis, the structural and compositional information of the influence on the surface reaction has been still lacking. In general, metal oxide surfaces reveal defect structures such as vacancies, steps, kinks, and facets. These defects are considerably related to the activity of most chemisorption and catalytic reactions. From a microscopic point of view, the defect sites are composed of atom assemblies having the reduced coordination and unsaturated valences. Therefore, for further progress of catalysis chemistry, it is indispensable to characterize the feature of each atom at an atomic level such as coordination number of the atom, bond length between the atom and adsorbates, and electronic structure localized on the sites. Successfulness of characterization at the atomic level as the first step will provide the development of an understanding of catalytic performance efficiently.

The use of ultrahigh vacuum (UHV) equipment and the development of many techniques for studying surface science have an enormous increase in understanding of surface physics and chemistry, and have a chance to contribute the development of new catalysis, sensors, and semiconductor–based devices. These techniques employ photons, electrons, and ions to determine surface structure, surface composition, and adsorbates; done with ever-increasing spatial resolution, time resolution, and energy resolution. Among these surface science techniques, scanning tunneling microscopy (STM) has become the premier technique. What makes STM of particular value is its ability to probe a small area of the surface in real space with atomic resolution, while many other techniques obtain information by averaging over a large area of the surface.

Since STM invention by Binnig, Rohrer, and coworkers [1, 2] in 1982, STM has been well established as a powerful technique to observe surface structures with atomic resolution in real space. STM relies on quantum mechanical tunneling. An atomically sharp tip is brought within a few Angstroms of a surface using an arrangement of piezoelectric transducers and a voltage is applied between the tip and the sample surface. At small separations the wave functions for electron states at the surface overlap with the wave functions associated with the tip and electrons may tunnel into or out of the surface, depending on the bias polarity. The tunnel current for STM measurements is typically of the order of 0.1-2.0 nA. There is an obvious requirement that the sample should be conductive enough to allow passage of the tunnel current. Many reviews of STM studies about the fundamentals of STM, various observation results, and theoretical analysis on STM images [3-5] have been already published since 1980s. STM can be operated in situ under variable pressures from ultra high vacuum (UHV) to a few atmospheres, and at different temperatures. A huge amount of STM studies have been reported on surface structures of semiconductor and metals with and without adsorbates. Chemisorption induced reconstructions of the surfaces were also observed by STM. Some of these observations in real-space provided direct evidence for determinations of surface structure, and moreover direct view of locally distributed reconstruction. In addition, STM-based techniques have been invented and developed as scanning probe microscopy (SPM). SPM include atomic force microscopy (AFM) that is applicable to an insulator surface. More detail information of STM and its theoretical treatments are described in Chapter 2.

In contrast to successful application of STM to semiconductor and metal surfaces, one can find few examples of STM works on oxide surfaces before 1990; atomically resolved images from cleavage surfaces of layered oxide superconductors such as $Bi_2Sr_2CaCu_2O_8$ [6], $Tl_2Ba_2CaCu_2O_8$ [7], and $YBa_2Cu_3O_{7-x}$ [8]. Within a past decade, many of the difficulties such as the conductivity requirement have been overcome in studying these surfaces and there is now a rapidly growing body of work where STM has provided definite information about surface structure of metal oxides.

In addition to atomic resolution, STM can be operated continuously in the order of second. Hence, STM do not only have an ability to reveal the influence of non-periodic structures on the activity of molecular adsorption and/or reactivity, but also have an great potential to show dynamism of surface chemical processes. Such dynamic study has been already applied to reveal surface reactions on semiconductor and metal surfaces in many cases, although that has not been much done it on metal oxide surfaces. Sequential visualizing of the oxide surfaces is still difficult; much effort is required to obtain steady tunneling current during imaging a surface without adsorbates. The difficulties notwithstanding, detail knowledge of the surface reactions is a necessary prerequisite for more understanding and progress catalysis chemistry further. Besides, making an environment more similar to that of a real working catalyst is expected to be the most efficient way for breakthrough into advanced catalyst. That is the reason for almost contents in this thesis chosen as the study of "*in situ* STM observation" of molecules and atoms and their surface "dynamic chemical processes on a metal oxide surface" at the atomic level. Furthermore, the study has been done along the purpose of exposing essential relations between catalytic reactions and the acid-base concept on a metal oxide surface.

The contents were divided into three parts. Chapters 3, 4, 5, 6 and 7 are the first part devoted to the studies of adsorption of base molecules: pyridine, its derivatives and ammonia on the $TiO_2(110)$ surface. These molecules are generally used as base probe molecules of surface acid sites to evaluate the acid-base property of metal oxide surfaces, where the feature and strength of the interaction indicated the catalytic performance of metal oxides. Surprisingly, the results in these Chapters revealed above the conventional acid-base concept. For example, whereas it was expected to make tight chemical bonding between coordinatively unsaturated Ti ions and nitrogen atom of pyridine in view of the conventional concept of the acid-base interaction, no chemical interaction between pyridine and the five-fold coordinated Ti sites on $TiO_2(110)$ has been found, as is described in Chapter 3. In contrast, ammonia molecules adsorbed as Lewis base molecules on the five-fold coordinated Ti sites, but that was only observed in the particular cases, as is mentioned in Chapter 6. Throughout these Chapters, it was concluded that the Lewis acidity of the five-fold coordinated Ti sites on the terrace was significantly controlled by two factors: oxygen vacancies of bridging oxygen rows and hydrogen atoms on that in the case of aromatic base molecules and in the case of ammonia. On the other hand, the activity of four-fold coordinated Ti sites at the step was controlled by not only their coordination number but also their surroundings including 2nd nearest neighbor or further. The preliminary understanding to examine chemical reactions of molecules adsorbed on metal oxide surfaces at the atomic level has been accomplished by these studies.

The second part is Chapter 7 where surface reactions of pyridine on $TiO_2(110)$ was performed at 350 K under gaseous reactants. Before the experiments, it was expected that pyridine or ammonia could react on the surface at certain temperature by the results of previous Chapters. That indicated one could find direct evidence on the relation between the active sites of surface reactions and the Lewis acidity on metal oxides. For this purpose, detecting the reaction product even one molecule on a metal oxide surface under reaction conditions was prerequisite during in situ STM observation. Recently, it has been established in the region done in the studies of metal surfaces, which revealed the ultimate resolution of STM to identify one single product molecule helped to detect even a quite small amount of reaction products. It is noted that ex-situ study such as comparative data acquisition of before and after reaction separately, involves possibility of misunderstanding the reaction sites and their role under the reaction conditions, because thermal diffusion of products might be dominant under reaction condition. Therefore, direct capturing the actual spot of surface reaction is indispensable to accurate discussions. Chapter 7 demonstrates surface reactions of pyridine at 350 K under gaseous reactants, whereas the reaction of pyridine at such low temperature was actually above my expectation. In this experiment, sequential recording of STM images have been successfully done for 5 h at the maximum, though the same scan area was kept by hand-operated tracking against a thermal drifting. Individual physisorbed or chemisorbed pyridine, and processes of forming products were visualized directly at the atomic level, although the surface reaction sites could not been specified, unfortunately.

The content of Chapter 8 as the third part is apparently unrelated to the above Chapters. However that is strongly related to the issue of acid-base, in particular for Chapter 6. A typical STM image of an oxide surface contain an ordered array of grayscale maxima and minima, usually interspersed with steps, vacancies, and dislocations other defects. However, the corrugation profiles do not in themselves solve an issue of interpretation of all the STM images and there is therefore scope for controversy. The STM image of $TiO_2(110)$ surface is not an exception. The problem is whether the oxygen vacancies or hydroxyl-like species were imaged, and certain experimental proof of hydroxyl-like species was provided, as is described in Chapter 8.

The remainder of Chapter 1 contains three short reviews describing recent topics about the surface science study of the titanium dioxide. Section 1.2 addresses about structural features of the TiO_2 and other metal oxide surfaces studied by surface science techniques including STM. Section 1.3 summarizes the recent works on *in situ* dynamic studies of STM, where four topics focusing on chemical processes and molecular reactions on Cu(110) and TiO_2(110) are presented. Section 1.4 summarizes the studies of acid-base properties on polycrystalline metal oxides.

1.2 Characterization of metal oxides by surface science techniques

Characterizing the oxide surface is still challenging not only because they often have a complicated atom arrangement, but also because many of the surface science techniques rely on the interaction of ion or electron beams with the surface. Depending on that interaction, the surface can charge negatively or positively. That effect can be serious, particularly for insulating sample. Possible solutions to compensate the charging are proposed as follows, using low energy electron flood gun, using semiconductive sample made by reducing the bulk composition or adding dopants, and using thin film samples on conducting substrates. For more information, a list of surveyed references of STM and AFM studies about single crystal metal oxides is summarized in Section 1.2.3. Several studies on a thin epitaxial oxide layer on metal substrate are also included, where the oxide layer is thin enough to circumvent the problem of conductivity.

1.2.1 Surface science approach to TiO_2 surfaces

In view of the theory of bulk band structure, the roughly octahedral crystal field experienced by the Ti cation splits the Ti 3d conduction band into three-fold degenerate t_{2g} and two-fold degenerate e_g components. A gap of just over 3 eV separates the empty Ti 3d states from the filled valence band of O 2p states. TiO_2 becomes conductive by slight reduction under UHV conditions, and oxygen deficiency introduces occupied Ti 3d donor levels just below the conduction band minimum, i.e. TiO_{2-x} is an n-type semiconductor. Therefore TiO_2 is a tractable material even for surface science techniques that might be disrupted by charging effect. Experimentally, structural information on these surfaces has been obtained using low energy electron diffraction (LEED) [9-12], reflection high energy electron diffraction (RHEED) [13], glancing angle or surface X-ray diffraction (SXRD) [14], electron stimulated desorption (ESD) [10], X-ray photoelectron diffraction (XPD) [15-17] and STM [18-23] [10, 24-27]. For other information on the electronic structure and surface adsorbed species, various techniques have been applied, for example, high energy electron loss spectroscopy (HREELS) [28-30], X-ray photoelectron spectroscopy (XPS) [12, 31-36], ultra-violet photoelectron spectroscopy (UPS) [11, 12, 28, 34-37], secondary ion mass spectroscopy (SIMS) [29, 30, 38], inverse photoemission spectroscopy (IPE) [39], fourier transform reflection-absorption IR spectroscopy (FT-RAIRS) [36], and temperature programmed desorption (TPD) [28-30, 40, 41] [12, 32, 33, 38, 42]. As theoretical approaches such as first-principle calculation [43-48], density functional theoretical (DFT) calculation [38, 49, 50] [51-54], and molecular dynamics (MD) simulations [55, 56] are often adopted to examine the surface electronic structure or the physical properties of stoichiometric or non-stoichiometric surfaces of TiO_2 single crystals.

The several planes of TiO_2 single crystal surfaces have been the subjects of numerous experimental and theoretical investigations over a wide range of temperatures and with a variety of surface treatments. The ideal structures of the (110), (100), and (001) planes formed by simple termination of the bulk rutile lattice are shown in Fig. 1.1. These low-index planes exhibit a wide variety of surface coordination environments; the (110) plane possesses both five-fold and six-fold coordinated Ti cations, five-coordinated Ti cations on the (100) plane, and four-fold coordinated Ti cations on the (001) plane. Each surface reconstructs to generate several types of relaxed or reconstructed surface structure. The remainder of this section summarizes the studies on the structural features of each TiO_2 surface plane.

1.2.1.1 $TiO_2(110)$

The (110) plane is the least coordinatively unsaturated surface of the three, thus the surface exhibits the most thermal stability, which was reproduced by theoretical approaches [43, 56-58]. A (1x1) pattern can be easily obtained by preparing a sample using annealing-oxidation treatment, or Ar^+ bombardment-annealing treatment at 600-900 K [9]. Subsequent annealing at 900-1000 K yields a (1x2) reconstruction [59, 60].

A bulk terminated surface structure of (1x1) model is described in Fig. 1.1(a). The model contains two types of in-plane Ti atoms: five-fold and six-fold coordinated. Protruding oxygen atoms bridge the six-fold coordinated Ti ions, forming O-ridges along the [001] axis. The alternative alignment of the exposed, five-fold coordinated Ti-rows and the bridging O-ridges results in the characteristic anisotropy on this surface. One-dimensional transport was found in the migration of adsorbed formate ions along the Ti row [61-64]. In the previous STM studies of this surface [18-23] [10, 24-27] [61-65] [66-71], it has been well established that the exposed Ti-rows (atoms) are imaged as bright lines (spots) in STM topography determined with positive sample bias voltages [61-64]. For more detail information; see a review of STM studies of $TiO_2(110)$ with and without adsorbates treated in Sections 1.2.2.

Ab nitio calculations [43, 50, 72] predicted that slight relaxation of the surface atom positions of (1x1) terrace to more thermally stable state, although the surface relaxation had not been shown by the structural study of medium energy electron diffraction (MEEM) [73]. However, surface relaxation has been confirmed recently by using the SXRD measurement [14] at the higher resolution limit of surface diffraction techniques. The main relaxation involve the top layer six-fold coordinated Ti atoms moving out of the surface by 0.012 ± 0.005 nm and the top layer five-fold coordinated Ti atoms moving towards the surface by 0.016 ± 0.005 nm, creating a rumpling of the top layer. This rumpling existed in the next layer but was of approximately half the magnitude. Bridging oxygen atoms also relaxed, by about 0.03 nm towards the surface. Rumpling effects were studied by a self-consistent electronic structure calculation with a conjugate gradient technique [74]. The surface relaxation induced only weak charge modifications of surface electronic character. However, the gap on the relaxed surface was wider than on the unrelaxed rutile structure. This effect yielded the surface gap close to the bulk value.

1.2.1.2 TiO_2(100)

The first report [75] on the (100) surface, which was prepared by polishing and annealing, revealed a series of (1x3), (1x5), and (1x7) reconstructions with increasing temperature at 850 K, 1050 K, and 1450 K, respectively. SXRD and LEED I/V analysis of the (1x3) surface proposed a model of surface structure containing (110) microfacets with significant displacements from the ideally terminated bulk atomic position [76]. The proposed model was further confirmed by STM imaging [77, 78], and a ESDIAD study of O^+ ions from the (1 x 3) surface [79]. The (1 x 3) surface was transferred back to the (1 x 1) surface after annealing at 950 K in oxygen, through a stage where the surface consists of (1 x 1) and (1 x 3) domain [79]. Faceting on a large scale on TiO_2(100) was observed by AFM [80].

1.2.1.3 TiO_2(001)

The (001) surface of TiO_2 is highly unstable and a polished surface easily becomes faceted on heating, since the ideal termination of the bulk structure in this direction exposes only four-fold coordinated Ti cations. LEED I-V measurements [81-83] have been performed for the (001) surface, and two possible structural models for TiO_2(001) were proposed: "{011}-faceted" phase produced by heating below ~850 K, and "{114}-faceted" phase produced by heating above 950 K. However, there are several controversies on these idealization; first, the temperatures are in an error due to measurement difficulties and second, the model of {114}-faceted surface did not match the observed LEED patterns exactly [59, 84]. They claimed the temperature should be corrected to be 1000 K and 1300 K, respectively. In general, different facets with crystallographic geometries were observed on the reconstructed (001) surface simultaneously. Although atomic resolved STM images of the surface are still lacking in this temperature region, but both STM observations [85] do show evidence for pronounced faceting of the (001) surface. The {011}-faceted surface produced by annealing at 783 K contained (001) planes on the order of 200 nm wide and {011}, {023}, {045}, {114}, and {011} facet planes on the order of 2000 nm wide. These results were in good agreement with ESDIAD data suggesting that the surface rearrange into {011} facet planes after mild annealing [86]. When $TiO_2(001)$ surfaces were annealed at 1698 K in O_2 for 36 h, {214}-faceted planes were observed by RHEED [13]. Large areas of flat terraces 0.5-1.0 μm wide and big steps 20-30 nm high are the main features observed on the rutile (100) surface. In AFM studies [80] of $TiO_2(001)$ surfaces annealed at 1573 K, the formation of a network of 500-3000 nm-high ridges were observed on the surface. Moreover, in the order of nano scale, network-like structure of $(7\sqrt{2} \times \sqrt{2})R45^\circ$ were observed recently by STM [87]. This structure appeared after annealing under UHV conditions to above 1273 K and subsequent quenching at a rate of ~100 Ks^{-1}.

1.2.2 STM observation of $TiO_2(110)$

At least 11 groups [18-23] [10, 24-27] have established their credentials in this field by obtaining STM images of $TiO_2(110)$ with atomic or unit cell resolution. A general feature in all of these images at positive sample bias is a series of bright rows running along the [001] directions on the (1x1) terraces, as shown in Fig. 1.2. As expected from the electronic structure, imaging of TiO_2 surfaces is most easily achieved at positive sample bias under conditions which probe empty electronic states. Since these states are of dominant Ti 3d atomic character, one interpretation of STM images assumes that the five-fold coordinated Ti^{4+} positions appear as topographic maximum. However, Fischer et al. proposed a "oxygen imaged" model as an inverse interpretation based on molecular orbital calculations and some observed images of defective bright rows on $TiO_2(110)$ [20, 88]. They claimed that strong Ti-O covalency at TiO_2 surfaces gives rise to a substantial contribution of O 2p states to conduction band level. Thus while electronic structure effects partially offset the protrusion of the bridging oxygen atoms, Ti 3d states can not completely dominate topography. In support for this assignment, it was also noted that the bright rows contain a large number of vacant sites corresponding to oxygen defect in the "O-imaged" model, as is hard to account for these vacancies in the "Ti-imaged" model. However, Onishi et al. presented direct evidence of "Ti-imaged" model from adsorption studies of formate ions [61-64], which were expected to adsorb on surface Ti cation sites. A model for adsorbed formate was also proposed by XPD [15-17] and theoretical calculations [17, 46], as a bidentate species; the adsorption involves two oxygen atoms bound to two surface titanium atoms. Onishi et al. obtained atomically resolved bright particles found onto the bright rows of the $TiO_2(110)$ surfaces exposed to formic acid, with a disordered arrangement at low coverages and a (2x1) ordering at higher coverages. The obvious interpretation of this data is to assign the bright particles to individual formate ions which are imaged via the LUMO of the ion. It follows that the bright rows correspond to Ti positions. Moreover, in contrast to STM studies imaging Ti cations, one can expected that outermost atoms of bridge-bound oxygen ridges of the surface were resolved as bright rows by non-contact atomic force microscopy (NC-AFM). Indeed, the atom resolved images of a $TiO_2(110)$-(1 x 1) surface and individual formate ions adsorbed on the surface revealed that formate was observed as bright spots between the bright rows along the [001] direction [89-91]. The compensatory results of NC-AFM studies proved the "Ti-imaged" model in STM studies.

Interpretation of STM images from the (1x2) reconstructed surface, which is yielded from annealing at 900-1000 K, has proved to be equally controversial. At least five models were proposed for (1x2) surface structure, a simple missing oxygen row model [60], an in-plane modified missing row model [19], an out-of-plane modified missing row model [21], an added Ti_3O_5 model [92], and an added Ti_2O_3 row model [23, 65]. Experimentally, Onishi et al. found that formate ions was not adsorbed on the ~0.2 nm higher bright rows above the terraces of $TiO_2(110)$ [61], which is in agreement with the added Ti_2O_3 row model. ESD studies [93] revealed the desorbing flux of oxygen ions produced by electron irradiation maximized in two bands normal to the surface, which further supports the added Ti_2O_3 row model. However, another (1x2) reconstructions with added rows (height ~0.28 nm) of $TiO_2(110)$ were simultaneously observed with the added Ti_2O_3 type by recent elevated temperature STM study [70]. The study concluded that such two distinctly different ordered reconstructions depend upon the level of bulk reduction of the crystal (degree of nonstoichiometry). While the added Ti_2O_3 type formed on the near stoichiometric surface, a cross-linked (1x2) reconstruction formed on heavily reduced crystals. For more information on the (1x2) reconstruction; see a term entitled {Oxygen-induced restructuring of an annealed $TiO_2(110)$surface} in Section 1.3.

1.2.3 A list of surveyed references on STM and AFM studies on surfaces of single crystal oxides and thin films

STM studies

$ZnO(000\bar{1})$ [94], $ZnO(10\bar{1}0)$ [94],

$SnO_2(110)$ [95],

$CeO_2(111)$ [96-98],

$V_2O_5(001)$ [99-101], $V_6O_{13}(001)$ [100],

NiO(001) [102, 103], NiO(100) film / Ni(100) [104], CoO(001) [105],

$Rb_{1/3}WO_3$(0001) [106, 107], WO_3(001) [108-111], WO_2(012) [112],

Fe_3O_4(111) [113], Fe_3O_4(001) [114], Fe_3O_4(110) [115, 116], α-Fe_2O_3(0001) [117-120],

α-Fe_2O_3(0001)film/Pt(111) [119], FeO(111)film/Pt(111) [121-123],

FeO(001) or Fe_3O_4(001) or γ-Fe_2O_3(001) films / MgO(001) [124],

$Rb_{0.3}MoO_3$(010) [125-128], $K_{0.3}MoO_3$(010) [125, 129-131], $Mo_{18}O_{52}$(100) [132, 133], Mo_8O_{23}(010) [132], η-Mo_4O_{11}(100) [132],

Cr_2O_3 (0001) film / Cr(110) [134, 135],

Al_2O_3 film / NiAl(110) [136-139],

SiO_2 film / Mo(110) [140, 141],

UO_2(110) [142], UO_2(111) [143], UO_2(001) [144],

TiO_2(110) [18-23] [10, 24-27], TiO_2(100) [77, 78], TiO_2(001) [85],

TiO_2 films / W(110) [145]

AFM studies

MgO(100) [146-148],

α-MoO_3(010) [132, 149],

V_2O_5(001) [150],

TiO_2(110), (100), (001) [80],

α-Al_2O_3(0001) [151]

1.3 Visualization of dynamic process of surface reactions by STM

Recently, several groups reported the dynamic studies on chemical processes by in situ STM observation: Cu(110) [152-162], Pd, Pt(111) [163], Ru(0001) [164], and $TiO_2(110)$ [61-65] [66-71]. These studies proved that *in situ* STM observation promises to provide detail insight into surface reactions, for example, the ability of STM to image simple molecules in a direct way allows surface coverage to be determined simply by counting the number of molecules in a defined area. Moreover this idea can be extended to study the kinetics of surface reactions [66]. Here, the studies on Cu(110) and $TiO_2(110)$ were briefly reviewed.

1.3.1 Dynamical behavior of admolecules on oxygen precovered Cu(110)

CO oxidation on oxygen pre-covered Cu(110) in the steady state at 400 K [152, 153], and 150 K [154] were observed by sequentially recorded STM at the atomic level. There was a strong preference for CO to react with oxygen along the p(2x1)-oxygen rows at 400 K [152, 153]. The reaction appeared to occur initially at the outer edge of an oxygen island, creating kink defects in the overlayer structure. Once created, these defects were more reactive than non-defects sites and play a dominant role in sustaining the reaction. A model is presented in which adsorbed oxygen, formed by-Cu-O- row scission at these defect sites, was reactive to CO, while p(2x1)-O atoms in the chain were not reactive. When dosed onto an oxygen pre-covered surface at 150 K [154], CO does not react with either p(2x1)-O or added -Cu-O- rows of 2-7 units at low oxygen coverages, presumably because both forms of oxygen are too strongly chemisorbed. However when the surface, partially covered with p(2x1)-O and co-adsorbed CO, was exposed to oxygen, the adsorbed CO reacted to form CO_2. More weakly bound atomic oxygen that was a precursor to chemisorbed oxygen in the form of the p(2x1)-O appears to be more reactive with CO than chemisorbed oxygen.

The synthesis of formaldehyde from methanol on oxygen pre-covered Cu(110) surfaces was studied by STM over temperature ranges within ±30 K of room temperature [155-157]. Sequential STM images showed that the conversion of methanol to methoxy resulted in the removal of oxygen from the [001] edges the p(2x1)-O islands. The adsorbed methoxy resulted in the formation of a (5x2) structure involving added Cu atoms. The decomposition of methoxy to formaldehyde occurred with STM images showing as an initial step the diminishing of the (5x2) methoxy islands. This occurred from island edges.

Methoxy oxidation to formate on oxygen pre-covered Cu(110) was also studied by STM under UHV conditions [158] and under dynamic conditions of co-dosing methanol and oxygen [159]. STM results under UHV conditions with a combination of TPD and molecular beam reaction measurements over temperature ranges within 300-500 K showed that oxygen acted as a promoter for methanol sticking and methoxy formation over a wide range of coverage, but poisons the reactivity on completion on the p(2x1)-O phase [158]. This was due to the lack of available Cu^0 sites to stabilize the methoxy intermediate and results in a large barrier for methanol. Advanced experiments under dynamic conditions of co-dosing methanol and oxygen at 300 K were performed [159]. High O_2:mehanol ratios in the gas phase did not produce formate production due to preferential growth of p(2x1)-O rather than methoxy, either. Inversely, continuous STM recording under certain conditions showed that low concentrations of gas-phase oxygen were seen to have the highest efficiency for formate production, since no p(2x1)-O islands formed which otherwise poison the reaction by site blocking and oxygen-adatom capture. The increased activity for low concentrations of oxygen precluded the possibility of molecular oxygen or "hot " oxygen adatoms being directly involved in the reaction. Therefore the production of formate from methanol during co-dosing stemmed from the reaction between highly reactive oxygen adatoms (which are thermally accommodated to the surface) with adsorbed methoxy.

In addition, the reactivity of added -Cu-O-rows at low coverages and p(2 x 1)-O islands at high coverages for reactions with ammonia was investigated at 300 and 400 K by in-situ imaging with atomic resolved [160-162]. The results at 300K revealed that oxygen in both forms is reactive with ammonia [160]. The reaction initiated from both the end and the side of the -Cu-O-rows. During the exposure of an ammonia and oxygen mixture the reactivity of the oxygen species present in the steady state was estimated to be comparable to that of oxygen pre-adsorbed at low coverages. At 400 K, reactions initiated inside the p(2 x 1)-O islands [161]. The N adatoms produced frequently blocked the ends of -Cu-O-rows inhibiting further reactions and creating stable, two-dimensional (2D) mixed N-O structures on the surface. Step defects on the surface were found to have a strong effect on the reactivity of oxygen adatoms [162]. Reactivity was high at the top and bottom of a $[1\bar{1}0]$ step and at the bottom of a [001] step, whereas it was very low at the top of a [001] step. Reaction at the bottom of [001] steps appeared to lead to deposition of Cu atoms at the step edge.

1.3.2 Anisotropic migration of formate ions adsorbed on $TiO_2(110)$

Formate ions adsorbed on $TiO_2(110)$ surfaces were imaged by STM under positive sample bias voltage. The formates in STM images were adsorbed on the rows of five-fold coordinated Ti^{4+} cations along the [001] axis [61-65], as was mentioned in the Section 1.2.2. These STM studies showed diffusion kinetics of formate ions adsorbed on $TiO_2(110)$. At saturation coverage on the (1x1) surface, the formate ions form an ordered (1x2) layer, and then a 20 x 20 nm^2 area of uncovered substrate was created by scanning the STM tip at +3.7 V sample bias. At room temperature the formate ions have significant mobility, and the residual ions outside diffused into the patches driven by the mutual repulsion in the monolayer. Serial STM images revealed the anisotropic migration; the transport of the formate anion along the one-dimensional row of Ti cations was an order of magnitude faster than that across the Ti row.

1.3.3 Microscopic kinetics of the decomposition reaction of acetate ions on $TiO_2(110)$

The reaction of an acetate-covered $TiO_2(110)$ surface was monitored by STM operated in a temperature-jump mode [66]. Similar to formates, a model for adsorbed acetates were proposed as a bidentate species bonded with the five-fold coordinated Ti^{4+} ions by ESD measurement [67]. Acetate ions were individually resolved at high temperatures where they started decomposing, due to restricted mobility on the metal-oxide surface. The number of ions appearing in a 10 x 10 nm^2 scan was counted in series of frames at an interval of 16.6 s/frame while the surface was heated from 510 to 540 K. The decrease in the number of adsorbed atoms per frame followed the expected first order decay which expected from the macroscopic rate law deduced from a thermal desorption study. From the analysis it was possible to derive a first order rate constant of $(4\pm1)x10^{-3}$ s^{-1}. The study demonstrated the ability of STM for observing reaction of dispersed intermediates on metal oxide surfaces by monitoring the response to temperature increments.

1.3.4 Oxygen-induced restructuring of an annealed $TiO_2(110)$surface

In situ STM observation of a surface/gas phase reaction on $TiO_2(110)$ was reported by several authors [68-71]. Onishi et al. [68, 69] first reported sequentially recorded STM images of oxygen-induced restructuring of $TiO_2(110)$. Hill-like structures comprising double strands were randomly nucleated over (1x1) terraces and then, hill-like structures were transformed into new terraces, while the surface reacted at 800 K in $1x10^{-5}$ Pa O_2. The authors proposed a reoxidation scheme to interpret the dynamics; partially reduced Ti^{n+} ions ($n \leq 3$), which were accumulated at interstitial positions in the vacuum annealed crystal, were oxidized at the surface to form the hills, added rows, and new terraces.

Li et al. [71] also reported similar results; after exposure to 5 x10^{-5} Pa of oxygen at elevated temperatures from 470 to 670 K, the (1x1) surface were covered with small (typically tens of angstroms wide) terraces. In addition, they observed patches on top and in between these terraces, which was an irregular network consisting of interconnected "rosettes" (width ~0.7 nm) with pseudo-hexagonal symmetry. Bennett et al [70], as is briefly discussed in Section 1.2.2, observed cross-linking sites in between (1x2) hill-like structures with double row internal structure. In this case, the height of hill-like structures was ~0.28 nm, which was the same as a step edge. Sequentially recorded STM data at 833 K in 5 x10^{-5} Pa O_2 at 1 min intervals showed growing of bright and dark strings along with an array of bright points and forming a large area of cross-linked (1x2) reconstruction on a (1x1) surface. The authors proposed a new model of the cross-linked (1x2) reconstruction in which the hill-like structure were composed of stoichiometric TiO_2 with the troughs formed by TiO_2 vacancies, which was based on an added Ti_3O_5 model [92]. The cross-linking sites were proposed to form when the troughs started to be filled by oxygen with Ti ions moving out of the strings to bridge the oxygen. They also showed that unreactivity of the (1x2) reconstruction which were not cross-linked. This type of reconstruction was prepared by vacuum annealing, therefore the added Ti_2O_3 type formed on the near-stoichiometric crystal, which did not reveal structural changes in STM images after exposure to ~1200 L of oxygen. Consequently, they concluded that on the near stoichiometric surface reactivity to oxygen was low and attributed to the formation of the stable Ti_2O_3 type termination. For heavily reduced crystals a cross-linked (1x2) reconstruction forms with high activity to oxygen resulting in a well-defined cyclic reaction (TiO_2 growth).

1.4 Acid-base property of metal oxides

The exposed cations and anions on oxide surfaces have long been described as acid-base pairs [165]. In general, the catalytic performance of metal oxides are evaluated in terms of acid-base properties and redox (oxidation-reduction) properties, therefore characterization and controlling the acid-base properties of oxide surfaces are essential issues for the development of industrial catalysts [165-168]. Much effort have been devoted to characterize the acid-base properties of oxides such as γ-Al_2O_3, TiO_2, WO_3, ZrO_2, Nb_2O_5, mixed oxides such as SiO_2-BeO, SiO_2-Al_2O_3, TiO_2-MgO, TiO_2-SiO_2-Al_2O_3 etc. Since near 1960s, a huge amount of literature and reviews [169-174] [175-179] on studying acid-base properties of the surface by using the titration method [180, 181], infrared (IR) spectroscopy [182-187], ultraviolet spectroscopy [188] and the gas-phase adsorption method [189, 190] were reported.

1.4.1 Evaluation method of acid-base property of metal oxides

To determine the surface acid strength and its range, temperature programmed desorption (TPD) and adsorption calorimetry of base molecules are often performed, where pyridine, ammonia, carbon monoxide, and butylamine are used as a standard base molecule in view of their basicity and molecular size. TPD provides an acid strength distribution as functions of temperature through the determination of kinetic parameters of desorption [191]. Adsorption calorimetry, which allows simultaneously the collection of both volumetric and calorimetric data, gives a more direct evaluation of the energy distribution of acid sites and permits the determination of thermodynamic parameters of adsorption [192]. These gas phase adsorption methods can be applied even on colored samples and is independent of the nature of surface acid sites, Brϕnsted and/or Lewis.

The Brϕnsted and Lewis acid sites are distinguished by using infrared (IR) spectroscopy, because the adsorption of base molecules at different acidic sites may result in a change in center, intensity, and profile of the vibrational bands as compared to the corresponding bands in the free, unperturbed molecule. Conventionally, the Brϕnsted acid site is defined as an OH group which is acidic enough to transfer its proton to a base molecule forming an ionized molecule. Associated ionized molecule with an OH site is referred to as hydrogen bonded molecule. This type is often described as a physisorbed type indicating non-specific interaction with chemical bonding [193-195]. The Lewis acid site is defined as a metal ion at defect site with reduced coordination and unsaturated valences. In this case, base molecule can be chemisorbed on the Lewis acid site with their lone-pare forming coordinate bond.

Finally, the titration analysis is discussed briefly. Acidity of solids can be written by Hammett acidity function H_0, which express the degree of protonation of weakly basic indicators in acid solution. The acidity fuction H_0 in the proton transfer equilibrium between an electro-neutral weak base B and the proton can be written as follows:

$$H_0 = pK_{BH^+} - \log\frac{[BH^+]}{[B]} \qquad (1.1)$$

Generally, mixed oxides have higher acidity than single component metal oxides. Several mixed oxides combined with TiO_2 such as SiO_2-TiO_2, Al_2O_3-TiO_2, ZrO_2-TiO_2, and ZnO-TiO_2 exhibited in the range of H_0 from –5.6 to –8.2, while the distribution of the TiO_2 was in the range of H_0 from +6.8 to –3.0 [181, 196-198]. The surface charge imbalance promoted by the mixing of metal components was interpreted as the caused of these differences. However, the charge imbalance was reported even on small sized oxides recently. Finely divided TiO_2 particle of ca. 5 nm exhibited the comparable highest acidity of $H_0 \leq -5.6$ [199]. The acid strength apparently increased with decreasing the particle size, indicating the generation of new and strong acid sites on small sized TiO_2 particles. Notwithstanding the absence of heterogeneous metal-oxygen-metal bonding, strong acid sites were generated even on the single component metal oxides in this case.

1.4.2 Acid-base property and hydroxyls on polycrystalline TiO_2 powder

Titanium dioxide, both in the forms of anatase and rutile, has much variety of applications as catalysts or catalyst supports; in photocatalytic devices [200-203], and as a white pigment [204, 205]. TiO_2 has been the object of surface properties with catalytic performance, i.e. surface acidity since 1960s.

One of the pioneering works of the rutile surface of adsorbed pyridine and ammonia by IR spectroscopy showed that the surface acidity of rutile was only Lewis type [186, 187, 206]. Although the reduction of a rutile surface with hydrogen resulted in the formation of Ti^{3+} and Ti^{2+} sites [207, 208], the population of Ti^{3+} on a reduced surface did not affect significantly the acid-base properties [187]. However, some of the molecularly adsorbed ammonia decomposed to NH_2 on the reduced surface [187]. Several authors [209-213] considered that it was presumably due to contaminants such as surface sulfates or chloride from sample preparation procedure, since similar decomposition of ammonia was observed on anatase, alumina [214], and silica [215], after hydration or chloridation of samples. On the other hand, theoretical calculations of ammonia adsorption on TiO_2 rutile suggested the dissociation process of NH_3 was slightly exothermic, and then concluded that a little amount of NH_3 can be dissociated on perfect terrace of (110) plane of the rutile surface [216].

Acidity of anatase surface was also reported as the Lewis type, while some authors [185, 209-211, 217, 218] reported the existence of Brφnsted acidity and ammonia decomposition [218, 219]. Presence of contaminants was also suspected in most cases as well as on the rutile surface. Indeed, the anatase prepared by hydrolysis of titanium oxide sulfate showed both Lewis and Brφnsted acidity, and the surfaces prepared from titanium *tetra*-isopropoxide showed only Lewis acidity [220].

In summary, most of researchers reported that TiO_2 powder catalysts only showed the Lewis acidity but not Brφnsted acidity with an exception of a sample including impurities:

chloride and sulfur, while the existence of hydroxyls on the both types of TiO_2 surface was well-confirmed by IR spectroscopy [221-226].

References

[1] G. Binnig, H. Rohrer, C. Gerber and E. Weibel, Phys. Rev. Lett. 49 (1982) 57.

[2] G. Binnig, H. Rohrer, C. Gerber and E. Weibel, Phys. Rev. Lett. 50 (1983) 120.

[3] W. Wiesendanger, *Scanning probe microscopy and spectroscopy*, Cambridge University Press., Cambridge, 1994.

[4] C.J. Chen, *Introduction to Scanning Tunneling Microscopy*, Oxford Univ. Press., Oxford, 1993.

[5] R.J. Behm, *Scanning Tunneling Microscopy and Related Methods*, Kluwer Academic Publishers, Dordrecht, 1990.

[6] M.D. Kirk, J. Nogami, A.A. Baski, D.B. Mitzi, A. Kapitulnik, T.H. Geballe and C.F. Quate, Science 242 (1988) 1673.

[7] X.L. Wu, C.M. Leiver, D.S. Ginley and R.J. Baughman, Appl. Phys. Lett. 55 (1989) 2129.

[8] L.E.C. van De Leemput, P.J.M. van Bentum, F.A.J.M. Driessen, J.W. Gerritsen, H. van Kempen, L.W.M. Schreurs and P. Bennema, J. Cryst. Growth 98 (1989) 551.

[9] V.E. Henrich and P.A. Cox, Rep. Prog. Phys. 48 (1985) 1481.

[10] I.D. Cocks, Q. Guo and E.M. Williams, Surf. Sci. 390 (1997) 119.

[11] R.H. Tait and R.V. Kasowski, Phys. Rev. B 20 (1979) 5178.

[12] H. Onishi, T. Aruga and Y. Iwasawa, J. Catal. 146 (1994) 557.

[13] L. Wang, J. Liu and J. M. Cowley, Surf. Sci. 302 (1994) 141.

[14] G. Charlton, P.B. Howes, C.L. Nicklin, P. Steadman, J.S.G. Taylor, C.A. Muryn, S.P. Harte, J. Mercer, R. McGrath, D. Norman, T.S. Turner and G. Thornton, Phys. Rev. Lett. 78 (1997) 495.

[15] S.A. Chambers, M.A. Henderson, Y.J. Kim and S. Thevuthasan, Surf. Rev. Lett. 5 (1998) 381.

[16] S. Thevuthasan, G.S. Herman, Y.J. Kim, S.A. Chambers, C.H.F. Peden, Z. Wang, R.X. Ynzunza, E.D. Tober, J. Morais and C.S. Fadley, Surf. Sci. 401 (1998) 261.

[17] S.A. Chambers, S. Thevuthasan, Y.J. Kim, G.S. Herman, Z. Wang, E. Tober, R. Ynzunza, J. Morais, C.H.F. Peden, K. Ferris and C.S. Fadley, Chem. Phys. Lett. 267 (1997) 51.

[18] D. Novak, E. Garfunkel and T. Gustafsson, Phys. Rev. B 50 (1994) 5000.

[19] M. Sander and T. Engel, Surf. Sci. Lett. 302 (1994) 263.

[20] S. Fischer, A.W. Munz, K.D. Schierbaum and W. Gopel, Surf. Sci. 337 (1995) 17.

[21] P.W. Murray, N.G. Condon and G. Thornton, Phys. Rev. B 51 (1995) 10989.

[22] U. Diebold, J.F. Anderson, K.-O. Ng and D. Vanderbilt, Phys. Rev. Lett. 77 (1996) 1322.

[23] H. Onishi and Y. Iwasawa, Surf. Sci. Lett. 313 (1994) 783.

[24] U. Diebold, J. Lehman, T. Mahmoud, M. Kuhn, G. Leonardelli, W. Hebenstreit, M. Schmid and P. Varga, Surf. Sci. 411 (1998) 137.

[25] M. Wagner, D. A. Bonnell and M. Ruhle, Appl. Phys. A 66 (1998) S1165.

[26] H. Norenberg, R.E. Tanner, K.D. Schierbaum, S. Fischer and G.A.D. Briggs, Surf. Sci. 396 (1998) 52.

[27] H. Norenberg and J.H. Harding, Phys. Rev. B 59 (1999) 9842.

[28] M.A. Henderson, Surf. Sci. 355 (1996) 151.

[29] M.A. Henderson, J. Phys. Chem. B 101 (1997) 221.

[30] M.A. Henderson, Surf. Sci. 400 (1998) 203.

[31] L.Q. Wang, D.R. Baer and M.H. Engelhard, Surf. Sci. 320 (1994) 295.

[32] M.B. Hugenschmidt, L. Gamble and C.T. Campbell, Surf. Sci. 302 (1994) 329.

[33] L. Gamble, L. S. Jung and C. T. Campbell, Surf. Sci. 348 (1996) 1.

[34] L.Q. Wang, A.N. Shultz, D.R. Baer and M.H. Engelhard, J. Vac. Sci. Technol. A 14 (1996) 1532.

[35] R. Wang, N. Sakai, A. Fujishima, T. Watanabe and K. Hashimoto, J. Phys. Chem. B 103 (1999) 2188.

[36] B.E. Hayden, A. King and M.A. Newton, J. Phys. Chem. B 103 (1999) 203.

[37] E.L. Roman, J.L. Desegovia, R.L. Kurtz, R. Stockbauer and T.E. Madey, Surf. Sci. 273 (1992) 40.

[38] L. Gamble, M.A. Henderson and C.T. Campbell, J. Phys. Chem. B 102 (1998) 4536.

[39] A.K. See and R.A. Bartynski, J. Vac. Sci. Technol. A 10 (1992) 2591.

[40] M.A. Henderson, Surf. Sci. 319 (1994) 315.

[41] M.A. Henderson, Langmuir 12 (1996) 5093.

[42] D. Brinkley, M. Dietrich, T. Engel, P. Farrall, G. Gantner, A. Schafer and A. Szuchmacher, Surf. Sci. 395 (1998) 292.

[43] M. Ramamoorthy, D. Vanderbilt and R.D. King-Smith, Phys. Rev. B 49 (1994) 16721.

[44] L.M. Wu, Y.F. Zhang, Y. Li, J.Q. Li and L.X. Zhou, Chinese J. Struc. Chem. 18 (1999) 304.

[45] P. Persson, A. Stashans, R. Bergstrom and S. Lunell, Int. J. Quantum Chem. 70 (1998) 1055.

[46] J. Ahdjoudj and C. Minot, Catal. Lett. 46 (1997) 83.

[47] G. Pacchioni, A.M. Ferrari and P.S. Bagus, Surf. Sci. 350 (1996) 159.

[48] O.V. Krasovska, E.E. Krasovskii, V.V. Nemoshkalenko and V.N. Antonov, J. Electr. Spec. Phenom. 76 (1995) 753.

[49] J. Goniakowski and M. J. Gillan, Surf. Sci. 350 (1996) 145.

[50] D. Vogtenhuber, R. Podloucky, A. Neckel, S.G. Steinemann and A.J. Freeman, Phys. Rev. B 49 (1994) 2099.

[51] J.M. Jehng, G. Deo, B.M. Weckhuysen and I.E. Wachs, J. Mol. Catal. A 110 (1996) 41.

[52] J. Goniakowski, J.M. Holender, L.N. Kantorovich, M.J. Gillan and J.A. White, Phys. Rev. B 53 (1996) 957.

[53] M. Casarin, C. Maccato and A. Vittadini, Appl. Surf. Sci. 142 (1999) 196.

[54] M. Casarin, C. Maccato and A. Vittadini, J. Phys. Chem. B 102 (1998) 10745.

[55] P.J.D. Lindan, N.M. Harrison, J.M. Holender and M.J. Gillan, Chem. Phys. Lett. 261 (1996) 246.

[56] P.M. Oliver, G.W. Watson, E.T. Kelsey and S.C. Parker, J. Mater. Chem. 7 (1997) 563.

[57] M. Matsui and M. Akaogi, Mol. Simul. 6 (1991) 239.

[58] D.W. Kim, N. Enomoto, Z. Nakagawa and K. Kawamura, J. Amer. Ceram. Soc. 79 (1996) 1095.

[59] V.E. Henrich and P.A. Cox, *The Surface Science of Metal Oxides*, Cambridge Univ. Press., Cambridge, 1994.

[60] P.J. Moller and M.C. Wu, Surf. Sci. 224 (1989) 265.

[61] H. Onishi, K. Fukui and Y. Iwasawa, Colloids and Surf. A 109 (1996) 335.

[62] H. Onishi and Y. Iwasawa, Jpn. J. Appl. Phys. 33 (1994) L1338.

[63] H. Onishi and Y. Iwasawa, Langmuir 10 (1994) 4414.

[64] H. Onishi and Y. Iwasawa, Chem. Phys. Lett. 226 (1994) 111.

[65] H. Onishi, K. Fukui and Y. Iwasawa, Bull. Chem. Soc. Jpn. 68 (1995) 2447.

[66] H. Onishi, Y. Yamaguchi, K. Fukui and Y. Iwasawa, J. Phys. Chem. 100 (1996) 9582.

[67] Q. Guo, I. Cocks and E.M. Williams, J. Chem. Phys. 106 (1997) 2924.

[68] H. Onishi and Y. Iwasawa, Surf. Sci. 357/358 (1996) 773.

[69] H. Onishi and Y. Iwasawa, Phys. Rev. Lett. 76 (1996) 791.

[70] R.A. Bennett, P. Stone, N.J. Price and M. Bowker, Phys. Rev. Lett. 82 (1999) 3831.

[71] M. Li, W. Hebenstreit and U. Diebold, Surf. Sci. 414 (1998) L951.

[72] P. Reinhardt and B.A. Hess, Phys. Rev. B 50 (1994) 12015.

[73] B.L. Maschhoff, J.M. Pan and T.E. Madey, Surf. Sci. 259 (1991) 190.

[74] J. Goniakowski and C. Noguera, Surf. Sci. 323 (1995) 129.

[75] Y.W. Chung, W.J. Lo and G.A. Somorjai, Surf. Sci. 64 (1977) 588.

[76] P. Zschack, J.B. Cohen and Y.W. Chung, Surf. Sci. 262 (1992) 395.

[77] P.W. Murray, F.M. Leibsle, H.J. Fisher, C.F.J. Flipse, C.A. Muryn and G. Thornton, Phys. Rev. B 46 (1992) 12877.

[78] P.W. Murray, F.M. Leibsle, C.A. Muryn, H.J. Fisher, C.F.J. Flipse and G. Thornton, Surf. Sci. 321 (1994) 217.

[79] Q. Guo, I. Cocks and E. M. Williams, Surf. Sci. 366 (1996) 99.

[80] M.D. Antonik and R.J. Lad, J. Vac. Sci. Technol. A 10 (1992) 669.

[81] L.E. Firment, Surf. Sci. 116 (1982) 205.

[82] R.H. Tait and R.V. Kasowski, Phys. Rev. B 20 (1979) 5168.

[83] R.V. Kasowski and R.H. Tait, Phys. Rev. B 20 (1979) 5178.

[84] K. Kim and M.A. Barteau, J. Catal. 125 (1990) 353.

[85] G.E. Poirier, B.K. Hance and J.M. White, J. Vac. Sci. Technol. B 10 (1992) 6.

[86] R.L. Kurtz, Surf. Sci. 177 (1986) 526.

[87] H. Norenberg, F. Dinelli and G.A.D. Briggs, Surf. Sci. Lett. 436 (1999) 635.

[88] S. Fischer, A. W. Munz, K.D. Schierbaum and W. Gopel, J. Vac. Sci. Technol. B 14 (1996) 961.

[89] K. Fukui, H. Onishi and Y. Iwasawa, Phys. Rev. Lett. 79 (1997) 4202.

[90] K. Fukui, H. Onishi and Y. Iwasawa, Chem. Phys. Lett. Dec 280 (1997) 296.

[91] K. Fukui, H. Onishi and Y. Iwasawa, Appl. Surf. Sci. 140 (1999) 259.

[92] C.L. Pang, S.A. Haycock, H. Raza, P.W. Murray, G. Thornton, O. Gulseren, R. James and D.W. Bullett, Phys. Rev. B 58 (1998) 1586.

[93] Q. Guo, I. Cocks and E.M. Williams, Phys. Rev. Lett. 77 (1996) 3851.

[94] T.M. Parker, N.G. Condon, R. Lindsay, F.M. Leibsle and G. Thornton, Surf. Sci. Lett. 415 (1998) 1046.

[95] F.H. Jones, R. Dixon, J.S. Foord, R.G. Egdell and J.B. Pethica, Surf. Sci. 376 (1997) 367.

[96] H. Norenberg and G.A.D. Briggs, Surf. Sci. 404 (1998) 734.

[97] H. Norenberg and G.A.D. Briggs, Surf. Sci. Lett. 424 (1999) 352.

[98] H. Norenberg and G.A.D. Briggs, Phys. Rev. Lett. 79 (1997) 4222.

[99] R.L. Smith, W. Lu and G. S. Rohrer, Surf. Sci. 322 (1995) 293.

[100] R.L. Smith, G.S. Rohrer, K.S. Lee, D.K. Seo and M.H. Whangbo, Surf. Sci. 367 (1996) 87.

[101] Y. Sakai and S. Ehara, Jpn. J. Appl. Phys. 38 (1999) 2944.

[102] M.R. Castell, P.L. Wincott, N.G. Condon, C. Muggelberg, G. Thornton, S.L. Dudarev, A.P. Sutton and G.A.D. Briggs, Phys. Rev. B 55 (1997) 7859.

[103] M.R. Castell, S.L. Dudarev, P.L. Wincott, N.G. Condon, C. Muggelberg, G. Thornton, D.N. Manh, A.P. Sutton and G.A.D. Briggs, Surf. Rev. Lett. 4 (1997) 1003.

[104] M. Baeumer, D. Cappus, H. Kuhlenbeck, H.J. Freund, G. Wilhelmi, A. Brodde and H. Neddermeyer, Surf. Sci. 253 (1991) 116.

[105] M.R. Castell, S.L. Dudarev, G.A.D. Briggs and A.P. Sutton, Phys. Rev. B 59 (1999) 7342.

[106] W. Lu, N. Nevins, M.L. Norton and G.S. Rohrer, Surf. Sci 291(1993)395.

[107] M.L. Norton, J.G. Mantovani and R.J. Warmack, J. Vac. Sci. Technol. A 7 (1989) 2898.

[108] F.H. Jones, K. Rawlings, J.S. Foord, P.A. Cox, R.G. Egdell, J.B. Pethica and B.M.R. Wanklyn, Phys. Rev. B 52 (1995) 14392.

[109] F.H. Jones, K. Rawlings, J.S. Foord, P.A. Cox, R.G. Egdell, J.B. Pethica and B.M.R. Wanklyn, Phys. Rev. B 53 (1996) 10412.

[110] F.H. Jones, K. Rawlings, J.S. Foord, R.G. Egdell, J.B. Pethica, B.M.R. Wanklyn, S.C. Parker and P.M. Oliver, Surf. Sci. 359 (1996) 107.

[111] F.H. Jones, R.A. Dixon and A. Brown, Surf. Sci. 369 (1996) 343.

[112] F.H. Jones, R.G. Egdell, A. Brown and F.R. Wondre, Surf. Sci. 374 (1997) 80.

[113] N.G. Condon, F.M. Leibsle, T. Parker, A.R. Lennie, D.J. Vaughan and G. Thornton,

Phys. Rev. B 55 (1997) 15885.

[114] G. Tarrach, D. Burgler, T. Schaub, R. Wiesendanger and H. J. Guntherodt, Surf. Sci. 285 (1993) 1.

[115] R. Jansen, V. A. M. Brabers and H. van Kempen, Surf. Sci. 328 (1995) 237.

[116] R. Jansen, B. J. Nelissen, D. L. Abraham, H. Vankempen and V. A. M. Brabers, IEEE Trans. Magn. 30 (1994) 4506.

[117] N.G. Condon, P.W. Murray, F.M. Leibsle, G. Thornton, A.R. Lennie and D.J. Vaughan, Surf. Sci. Lett. 310 (1994) 609.

[118] N.G. Condon, F.M. Leibsle, A.R. Lennie, P.W. Murray, T.M. Parker, D.J. Vaughan and G. Thornton, Surf. Sci. 397 (1998) 278.

[119] S.K. Shaikhutdinov and W. Weiss, Surf. Sci. Lett. 432 (1999) 627.

[120] C.M. Eggleston, Amer. Mineral. 84 (1999) 1061.

[121] Y.J. Kim, C. Westphal, R.X. Ynzunza, Z. Wang, H.C. Galloway, M. Salmeron, M.A. VanHove and C.S. Fadley, Surf. Sci. 416 (1998) 68.

[122] W. Weiss and M. Ritter, Phys. Rev. B 59 (1999) 5201.

[123] M. Ritter, W. Ranke and W. Weiss, Phys. Rev. B 57 (1998) 7240.

[124] Y. Gao, Y.J. Kim and S.A. Chambers, J. Mater. Res. 13 (1998) 2003.

[125] U. Walter, R.E. Thomson, B. Burk, M.F. Crommie, A. Zettl and J. Clarke, Phys. Rev. B 45 (1992) 11474.

[126] G. Rudd, D. Novak, D. Saulys, R.A. Bartynski, S. Garofalini, K.V. Ramanujachary, M. Greenblatt and E. Garfunkel, J. Vac. Sci. Technol. B 9 (1991) 909.

[127] S. Tanaka, E. Ueda and M. Sato, Solid State Commun. 87 (1993) 877.

[128] E. Garfunkel, S.H. Garofalini, M. Greenblatt, G. Ebert, D. Novak, G. Rudd, T. Gustafsson and S. Wang, Science 246 (1989) 99.

[129] D. Anselmetti, R. Wiesendanger, H.J. Guntherodt and G. Gruner, Europhys. Lett. 12 (1990) 241.

[130] K. Nomura and K. Ichimura, Solid State Commun. 71 (1989) 149.

[131] A. Zettl, M.F. Hundley, J. Clarke, L.C. Bourne, R.E. Thompson, U. Walter and M.F. Crommie, Syn. Metals 29 (1989) F445.

[132] R.L. Smith and G.S. Rohrer, J. Solid State Chem. 124 (1996) 104.

[133] G.S. Rohrer, W. Lu, R.L. Smith and A. Hutchinson, Surf. Sci. 292 (1993) 261.

[134] N.M.D. Brown and H.X. You, Surf. Sci. 233 (1990) 317.

[135] M. Muller and H. Oechsner, Surf. Sci. 387 (1997) 269.

[136] T. Bertrams, A. Brodde, H. Hannemann, C.A. Ventrice, G. Wilhelmi and H. Neddermeyer, Appl. Surf. Sci. 75 (1994) 125.

[137] R.P. Blum, D. Ahlbehrendt and H. Niehus, Surf. Sci. 396 (1998) 176.

[138] R.P. Blum and H. Niehus, Appl. Phys. A 66 (1998) S529.

[139] J. Libuda, F. Winkelmann, M. Baeumer, H. J. Freund, T. Bertrams, H. Neddermeyer and K. Mueller, Surf. Sci. 318 (1994) 61.

[140] K.H. Schulz and D.F. Cox, J. Phys. Chem. 96 (1992) 7394.

[141] K.H. Schulz and D.F. Cox, J. Phys. Chem. 97 (1993) 3555.

[142] C. Muggelberg, M.R. Castell, G.A.D. Briggs and D.T. Goddard, Surf. Sci. 404 (1998) 673.

[143] C. Muggelberg, M.R. Castell, G.A.D. Briggs and D.T. Goddard, Surf. Rev. Lett. 5 (1998) 315.

[144] C. Muggelberg, M.R. Castell, G.A.D. Briggs and D.T. Goddard, Appl. Surf. Sci. 142 (1999) 124.

[145] G.S. Herman, M.C. Gallagher, S.A. Joyce and C.H.F. Peden, J. Vac. Sci. Technol. B 14 (1996) 1126.

[146] K. Sangwal, F. Sanz, J. Servat and P. Gorostiza, Surf. Sci. 383 (1997) 78.

[147] D. Abriou, F. Creuzet and J. Jupille, Surf. Sci. 352(1996) 499.

[148] S.S. Perry and P.B. Merrill, Surf. Sci. 383 (1997) 268.

[149] R.L. Smith and G.S. Rohrer, J. Catal. 163 (1996) 12.

[150] A. DaCosta, C. Mathieu, Y. Barbaux, H. Poelman, G.D. Vennik and L. Fiermans, Surf. Sci. 370 (1997) 339.

[151] J.R. Heffelfinger, M.W. Bench and C.B. Carter, Surf. Sci. Lett. 370 (1997) 168.

[152] W.W. Crew and R.J. Madix, Surf. Sci. Lett. 319 (1994) 34.

[153] W.W. Crew and R.J. Madix, Surf. Sci. 349 (1996) 275.

[154] W.W. Crew and R.J. Madix, Surf. Sci. 356 (1996) 1.

[155] F.M. Leibsle, S.M. Francis, S. Haq and M. Bowker, Surf. Sci. 318 (1994) 46.

[156] F.M. Leibsle, S.M. Francis, R. Davis, N. Xiang, S. Haq and M. Bowker, Phys. Rev. Lett. 72 (1994) 2569.

[157] M. Bowker and F. Leibsle, Catal. Lett. 38 (1996) 123.

[158] S.M. Francis, F.M. Leibsle, S. Haq, N. Xiang and M. Bowker, Surf. Sci. 315 (1994) 284.

[159] A.H. Jones, S. Poulston, R.A. Bennett and M. Bowker, Surf. Sci. 380 (1997) 31.

[160] X.C. Guo and R.J. Madix, Surf. Sci. 387 (1997) 1.

[161] X.C. Guo and R.J. Madix, Faraday Discuss. 105 (1996) 139.

[162] X.C. Guo and R.J. Madix, Surf. Sci. 367 (1996) L95.

[163] J.Wintterlin, S. Volkening, T.V.W. Janssenes, T. Zambelli and G. Ertl, Science 278 (1997) 1931.

[164] J. Wintterlin, J. Trost, S. Renisch, R. Schuster, T. Zambelli and G. Ertl, Surf. Sci. 394 (1997) 159.

[165] K. Tanabe, Solid Acids and Bases, (Academic Press., New York, 1970).

[166] H.A. Benei and B.H.C. Winquist, Adv. Catal. 27 (1978) 97.

[167] Y. Iwasawa, in: Stud. Surf. Sci. Catal., Vol. 101 (*Proc.11th Int. Congr. Catalysis*), eds. J. W. Hightower, W. N. Delgass, E. Iglesia and A.T. Bell (Elsevier, Amsterdam, 1996) p. 21.

[168] Y. Iwasawa, Catal. Surveys. Jpn. 1 (1997) 3.

[169] K. Tanabe, M. Misono, Y. Ono and H. Hattori, in: Stud. Surf. Sci. Catal. Series, 51 (Elsevier, Amsterdam, 1989).

[170] C.N. Satterfield, *Heterogeneous Catalysis in Practice*, McGraw-Hill, New York, 1980.

[171] G. Busca, Catal. Today 41 (1998) 191.

[172] G.A. Somorjai and M.X. Yang, J. Mol. Catal. A 115 (1997) 389.

[173] G.A. Somorjai, Chem. Rev. 96 (1996) 1223.

[174] B.E. Bent, Chem. Rev. 96 (1996) 1361.

[175] M.K. Weldon and C.M. Friend, Chem. Rev. 96 (1996) 1391.

[176] M.A. Barteau, Chem. Rev. 96 (1996) 1413.

[177] M. Kiskinova, Chem. Rev. 96 (1996) 1431.

[178] C.T. Campbell, J. Chem. Soc. Faraday Trans. 92 (1996) 1435.

[179] F.M. Leibsle, P.W. Murray, N.G. Condon and G. Thornton, J. Phys. D 30 (1997) 741.

[180] K. Shibata, T. Kiyoura, J. Kitagawa, T. Sumiyoshi and K. Tanabe, Bull. Chem. Soc. Jpn. 46 (1973) 2985.

[181] K.R.P. Sabu, K.V.C. Rao and C.G.R. Nair, Bull Chem Soc Jpn 64 (1991) 1920.

[182] D.J.C. Yates, J. Phys. Chem. 65 (1961) 746.

[183] E.P. Parry, J. Catal. 2 (1963)

[184] R.B. Michael, R.K. Theodore and H.R. Kee, J. Phys. Chem. 68 (1964) 3197.

[185] C. Morterra, G. Ghiotti and E. Garrone, J. Chem. Soc. Faraday I 76 (1980) 2102.

[186] G.D. Parfitt, J. Ramasbotham and C. H. Rochester, J. Chem. Soc. Faraday Trans. 72 (1971) 1500.

[187] G.D. Parfitt, J. Ramasbotham and C. H. Rochester, J. Chem. Soc. Faraday Trans. 67 (1971) 841.

[188] Y. Kageyama, T. Yotsuyanagi and K. Aomura, J. Catal. 36 (1975) 1.

[189] M. Takahashi, Y. Iwasawa and S. Ogasawara, J. Catal. 45 (1976) 15.

[190] R.L. Richardson and S.W. Benson, J. Phys. Chem. 61 (1957) 405.

[191] J.L. Lemaitre, in: "Characterization of heterogeneous catalysts", F. Delannay (Dekker, New York, 1984).

[192] N. Cardona-Martinez and J.A. Dumesi, Adv. Catal. 38 (1992) 149.

[193] M.R. Basila, T.R. Kantner and K.H. Rhee, J. Phys. Chem. 68 (1964) 3197.

[194] L.M. Parker, D.M. Bibby and G.R. Burns, J. Chem. Soc. Faraday Trans. 87 (1991) 3319.

[195] M. Niwa, N. Katada and Y. Murakami, J. Catal. 134 (1992) 340.

[196] K. Tanabe, C. Ishiya, I. matsuzaki, I. Ichikawa and H. Hattori, Bull. Chem. Soc. Jpn. 45 (1972) 47.

[197] H. Nakabayashi, Bull. Chem. Soc. Jpn. 65 (1992) 914.

[198] K. Shibata, T. Kiyoura, J. Kitagawa, T. Sumuyoshi and K. Tanabe, Bull. Chem. Soc. Jpn. 46 (1973) 2985.

[199] K. Nishiwaki, A. Ueno, N. Kakuta and H. Nakabayashi, J. Catal. 118 (1989) 498.

[200] H. Kominami, S. Murakami, Y. Kera and B. Ohtani, Catal. Lett. 56 (1998) 125.

[201] J. Schwitzgebel, J. G. Ekerdt, F. Sunada, S. E. Lindquist and A. Heller, J. Phys. Chem. B. 101 (1997) 2621.

[202] N. Negishi, K. Takeuchi, T. Ibusuki and A. K. Datye, J. Mater. Sci. Lett. 18 (1999) 515.

[203] A. Fujishima and K. Honda, Nature 238 (1972) 37.

[204] R. Kobayashi, M. Yajima and K. Kameyama, Nippon Kagaku Kaishi. 6 (1996) 589.

[205] U. Gesenhues, Solid State Ionics. 2 (1997) 1171.

[206] M. Primet, P. Pichat and M.-V. Mathieu, J. Phys. Chem. 75 (1971) 1216.

[207] H.P.R. Frederikse, J. Appl. Phys. 32 (1961) 2271.

[208] G.B. Raupp and J.A. Dumesic, J. Phys. Chem. 89 (1985) 5240.

[209] G. Busca, H. Saussey, O. Saur, J.C. Lavalley and V. Lorenzelli, Appl. Catal. 14 (1985) 245.

[210] A. Hess and E. Kemnitz, Appl. Catal. A149 (1997) 373.

[211] C. Martin, I. Martin and V. Rives, J. Mater. Sci. 30 (1995) 3847.

[212] F. Lange, K. Hadjiivanov, H. Schmelz and H. Knozinger, Catal. Lett. 16 (1992) 97.

[213] M. Ziolek, J. Kujawa, O. Saur, A. Aboulayt and J.C. Lavalley, J. Mol. Catal. A 112 (1996) 125.

[214] J.B. Peri, J. Phys. Chem. 69 (1965) 231.

[215] J.B. Peri, J. Phys. Chem. 70 (1965) 2937.

[216] A. Markovits, J. Ahdjoudj and C. Minot, Surf. Sci. 365 (1996) 649.

[217] A. Severino, J. Vital and L. S. Lobo, Stud. Surf. Sci. Catal. 78 (1993) 685.

[218] K. Hadjiivanov, V. Bushev, M. Kantcheva and D. Klissurski, Langmuir 10 (1994) 464.

[219] R.M. Pittman and A.T. Bell, Catal. Lett. 24 (1994) 1.

[220] T. Kantoh and S. Okazaki, Bull. Chem. Soc. Jpn. 54 (1981) 3259.

[221] M. Primet, P. Pichat and M.-V. Mathieu, J. Phys. Chem.75 (1971) 1221.

[222] S.W. Ho, J. Chinese Chem. Soc. 43 (1996) 155.

[223] P. Jones and J. A. Hockey, J. Chem. Soc. Faraday Trans. (1971)2669.

[224] P. Jackson and G. D. Parfitt, J. Chem. Soc. Faraday Trans. (1971) 896.

[225] D.M. Griffiths and C.H. Rochester, J. Chem. Soc. Faraday Trans. (1976) 1510.

[226] K. Tanaka and J.M. White, J. Phys. Chem. 86 (1982) 4708.

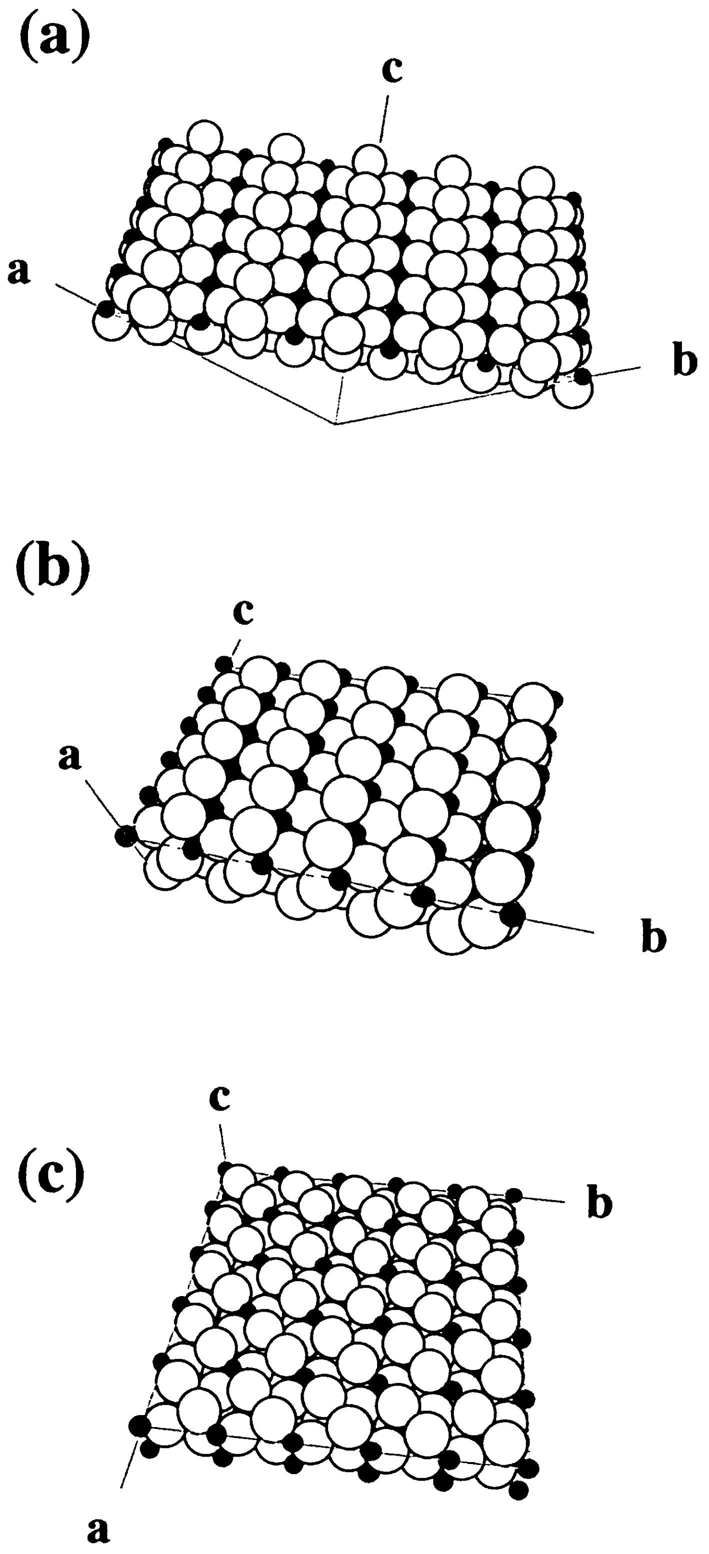

Figure 1.1 Ideal termination of (a) the $TiO_2(110)$, (b) the $TiO_2(100)$, and (c) the $TiO_2(001)$ surfaces. Filled and open symbols represent titanium and oxygen atoms, respectively. Letters; a, b, and c represent [100], [010], and [001] directions, respectively

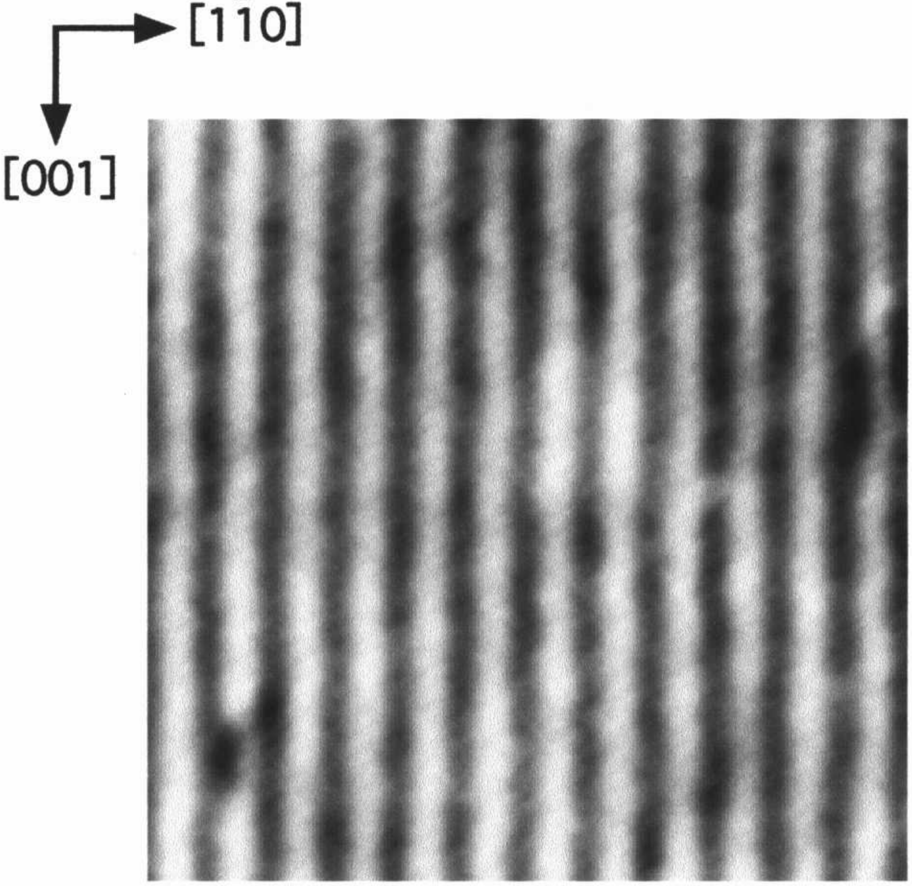

Figure 1.2 A constant current STM images of TiO_2(110)-(1x1) surface.
8x8 nm^2, sample bias voltage: +2.5 V, tunneling current: 0.10 nA

Chapter 2

Experimental

2.1 Scanning Tunneling microscopy (STM)

2.1.1 Outline

STM relies on quantum mechanical tunneling. An atomically sharp tip is brought within a few Angstroms of a surface using an arrangement of piezoelectric transducers and a voltage is applied between the tip and the sample (Fig. 2.1). At small separations the wave functions for electron states at the surfaces overlap with the wave functions associated with the tip and electrons may tunnel into or out of the surface, depending on the bias. The tunneling current shows an exponential variation with tip-surface separation because of the exponential decay of the wave functions into the vacuum. The tip is moved parallel to the surface in the xy plane while the z position in controlled. There are two principal modes of image acquisition. In the constant height mode the tunnel current is simple measured as a function of xy coordinates. In the alternative constant current mode a negative feedback is applied to the z piezo to keep the tunnel current constant and the z displacement is monitored as a function of xy coordinates. The constant current mode allows for more rapid scanning across the surface but there is a significantly larger risk of "tip crash" on surfaces containing irregular protrusions or large numbers of steps. The image is built up from a series of corrugation profiles, i.e. plots of z displacement as a function of x displacement. There are finally transformed into grayscale images that represent maximum outward z displacement as white and maximum inward displacement as black. In addition the feedback loop may be disengaged at each pixel point in the image and a current-voltage (I-V) curve measured at that point. It may be shown that the normalized differential conductance (dI/dV)/(I/V) is directly proportional to the electron density of filled or empty states.

2.1.2 Theoretical treatment of STM

2.1.2.1 Properties of the tunneling current

The tunneling current between a tip and sample separated by a spacing z is determined by the tunneling probability *T*. The tunneling probability *T* was evaluated from a one-dimensional potential barrier (Fig. 2.2) on a time-dependent treatment (Bardeen's transfer Hamintonian approach) [1]. Within the treatment, the *T* of potential barrier V_0 is expressed by

$$T \propto \exp(-2kz) \tag{2.1}$$

with the decay rate

$$k = \left[2m(V_0 - E)\right]^{\frac{1}{2}} / \hbar \tag{2.2}$$

where *E* is the impinging electron energy of *E*, and m is electron mass. The strong exponential dependence of *T* on the barrier width z and the square root of an effective barrier height $(V_0\text{-}E)^{1/2}$ is typical for tunneling, independent of the exact shape of the barrier. Assuming a barrier width of 0.5 nm and an effective barrier height of 4 eV, we get a value of about 10^{-5} for the exponential factor. Changing the barrier width by 0.1 nm then typically leads to a change of the *T* by one order of magnitude. The extreme sensitivity of the tunneling probability to the barrier width led Binnig et al. [2] to the idea that a microscope based on tunneling should provide extremely high spatial resolution.

2.1.2.2 Models of STM

For the three-dimensional case to be considered for STM, Bardeen's transfer Hamiltonian approach, based on a perturbative treatment of tunneling, is still applicable and provides an appropriate insight into the physics of the tunneling process as well as a connection to specific tip and sample surface properties.

Within Bardeen's formalism, the tunneling current I can be evaluated in first-order time-dependent perturbation theory according to

$$I = \frac{2\pi e}{\hbar}\sum_{\mu,\nu}\left\{f(E_\mu)\left[1 - f(E_\nu - eU)\right] - f(E_\nu + eU)\left[1 - f(E_\mu)\right]\right\}\bullet\left|M_{\mu\nu}\right|^2\delta(E_\nu - E_\mu) \qquad (2.3)$$

where $f(E)$ is the Fermi function, U is the applied sample bias voltage, $M_{\mu\nu}$ is the tunneling matrix element between the unperturbed electronic states ψ_μ of the tip and ψ_ν of the sample surface, and $E_\mu(E_\nu)$ is the energy of the state $\psi_\mu(\psi_\nu)$ in the absence of tunneling. The delta function describes the conservation of energy for

the case of the tunneling matrix element which is given by

$$M_{\mu\nu} = \frac{-\hbar^2}{2m}\int dz\bullet\left(\psi_\mu^*\nabla\psi_\nu - \psi_\nu\nabla\psi_\mu^*\right) \qquad (2.4)$$

where the integral has to be evaluated over any surface lying entirely within the vacuum barrier region separating the two electrodes. The quantity in parentheses can be identified as a current density. To derive the matrix $M_{\mu\nu}$ element from Eq. (2.2), explicit expressions for the wave functions ψ_μ and ψ_ν of the tip and sample surface are required. Unfortunately, the atomic structure of the tip is generally not known, therefore, a model tip wave function has to be assumed for calculation of the tunneling current.

Most qualitative interpretations of STM images are based implicitly on the Tersoff-Hamann model [3]. Here the tip electronic wave functions are assumed to be described by spherically symmetrical s-waves. For small sample bias, it may be shown that the tunneling current I is given by

$$I \propto \sum_{s} \left|\psi_s(r_o)\right|^2 \delta(E_s - E_t) \tag{2.5}$$

where the summation is taken over amplitude of sample wave function s at the center of the tip whose coordinates are specified by r_0, and the subscripts refer to the energy of electronic states in the sample (s) relative to the Fermi energy of the tip (t). By the definition the summation corresponds to the local density of sample electronic states at the center of tip curvature and therefore, the constant current images correspond to contours of constant density of sample electronic states.

There are already many approximations at this stage. STM experiments almost invariably use W or Pt/Ir tips, and if they terminate with a single transition metal atom, the tip wave functions will certainly not be a s-wave. For example, model calculations on a cluster providing a realistic model of a W tip revealed a strong 5_{dz2} resonance near the Fermi level [4].

A recent development in interpretation of STM images of adsorbate system is direct calculation of tunneling currents using the electron scattering quantum chemistry (ESQC) approach [5]. The system for the calculation is infinite in z with a single tunnel gap, each atom being represented by a set of basis functions: a semi-infinite substrate is built by repetition of a cell slab from $-\infty$ to the surface. Then the adsorbate and the tip apex are positioned, and this tip apex is connected to a second semi-infinite solid up to $+\infty$, which represents the tip bulk. Therefore, the infinite nature of the electron reservoirs on each side of the tunnel gap is correctly described here. The system is finite in the lateral x, y directions with cyclic boundary conditions. This model was used with notable success to treat adsorbed C_6H_6/Rh(111) system [6] and C_6H_6/Pt(111) system [7, 8]. In the latter system, the contrast simulations reproduced the shape of the molecule pattern in the STM image, which was strongly dependent on the chemisorption site on the (111) terrace, in agreement with the experimentally observed data [9].

2.2 Apparatus

The STM measurements were carried out in a JEOL JSTM-4500 VT (Fig. 2.3), variable temperature UHV system containing three chambers. The first is a turbomolecular pumped chamber, which offers facilities for sample exchange without breaking UHV atmosphere of the latter two chambers individually pumped by an ion pump. The second is a sample pre-treatment chamber equipped with an Ar^+ sputtering gun, rear-view low energy electron diffraction (LEED)/Auger electron Spectroscopy (AES) four-grid optics (OMICRON). In this work, LEED measurements were performed only for qualitative interpretation of the spot patterns, and the AES measurements were used to monitor surface cleanliness. The third chamber is equipped with a variable temperature STM stage, which can be operated within a temperature range of 4-1000 K. The base pressure of the pre-treatment chamber and the STM-chamber are 1×10^{-8} Pa, and each chamber is equipped with a capillary gas doser. The temperature of the sample surface is monitored with an IR radiation thermometer (Chino).

Samples are mounted onto standard specimen holders which are moved to any experimental location within the UHV system by use of a linear transport system. Further, three specimen holders and three tips are simultaneously kept at the parking stage in the pre-treatment chamber.

STM images were recorded with an electrochemically etched W tip. Electrochemical preparation of W was performed with 2 N NaOH solution, which is most often used as an etching electrolyte. Bias voltages were applied to the $TiO_2(110)$ sample with the tip at virtual ground. These ranged from +1.0 to +5.0 V; negative voltages invariably caused tip crashes. Optimum imaging of the surface was obtained with a bias voltage of +1.0 to +2.5 V. Comparing with observing silicon surfaces, the image quality degrades relatively fast, especially during or after exposure to gaseous adsorbate or reactants, probably due to the presence of adsorbates on the tip. In many cases, applying a high bias voltage (up to +10 V) during scanning is successful for restoring a tip state that renders atomic resolution.

2.3 Sample preparation

A one-side polished $TiO_2(110)$ wafer of 6.5 x 1 x 0.25 mm^3 was obtained from Earth Jewelry Co. (Japan). For removal of carbon contaminants and raising quality of the crystal, the sample was annealed in air at 1000 K for 2 h. Then, nickel film was deposited on the opposite side of the polished for resistive heating in the UHV system. A small electrical input power (ca. 2V, 1A) was sufficient to heat the wafer at 1200 K.

Sample cleaning was achieved by bombardment with 3 keV Ar+ ions with typical sample currents of order 0.3 μA and subsequent annealing in UHV at 900 K. After the several cleaning cycles, no features other than those originating from the presence of Ti and O were observed in AES, and a sharp 1x1 LEED pattern was routinely obtained.

2.4 Original recipes for getting atomic resolution images of STM

Scanning tunneling microscopy has been well recognized as an ultimate technique, but there is still a large room to improve the operation of scanning tunneling microscope. Most of the difficulty for data acquisition of atomic resolution can overcome preparation of fresh atomically sharp tip. However, controlling and keeping the tip condition well are the most difficult issue for almost STM users. As is many researchers say, the STM image is changed its resolution accidentally. Therefore there may not been the way of controlling the tip conditions in the strict meaning. Nevertheless, I hope to describe some recipes for future prospectors.

First, it may be the most basic procedure for STM users; when a fresh tip is used at first time, tip annealing with silicon wafer heated above 1300 K within 30 s is an effective way for improving resolution in a short time. Before the tip annealing, tip is closely approached to the silicon surface, and then the tip is withdrawn until a slight distant point from the surface in the micro order. Annealing the tip may involve deposition process of evaporated silicon atoms to the tip surface. However, annealed tip often provide atomic resolved image directory without any procedures. The evaporated silicon atoms might play a role of micro tip on the tip apex.

Second, it is useful way to change the condition of tip drastically, but it is necessary to care the tip damage; when an STM image seems to be dull or overlapping the same topography, touching or weak collision of tip to the surface is applicable. Dull image may be caused of lost of micro tip on the tip apex. Overlapping the same topography is caused of co-existence of double or triplet tips within an effective region for tunneling current on the tip apex. When the surface adsorbates are observed, the tip apex is particularly disturbed by those adsorbates in such a way. For grazing tip apex, scanning parameters, mainly bias voltage or reference tunneling current, are carefully alternated lower and higher values until an STM image is disturbed by tip contact to the surface, and then the parameters is quickly recovered. If there is nothing to change in the image by that, a try to apply high bias voltage between the tip and the surface is a possible solution. High sample bias voltage between −10 and +10 V are often applied in my experiments.

Finally, it is not for a wide use and not to be a proper content for the recipe, however I recommended using sound for delicate adjustment of the tip conditions, especially in a pre-final step to obtain the atomic resolved images. Indeed, the JEOL JSTM-4500 VT was not much properly designed for avoiding an influence of noise or sound from the outside. Even human voice nearly whispering often influenced in the image acquisition. However, that indicates sound is available to change tip condition, and a single weak beat with the hand is the most effective sound for improving the tip condition into the atomic resolution. Such simple way was thought to be the best way in my experience.

References

[1] J. Bardeen, Phys. Rev. Lett. 6 (1961) 57.

[2] G. Binnig, H. Rohrer, C. Gerber and E. Weibel, Phys. Rev. Lett. 49 (1982) 57.

[3] J. Tersoff and D.R. Hamann, Phys. Rev. Lett. 50 (1983) 1998.

[4] G. Doyen, E. Kotter, J.P. Vigneron and M. Scheffler, Appl. Phys. A 51 (1990) 281.

[5] P. Sautet and C. Joachim, Phys. Rev. B 38 (1988) 12238.

[6] P. Sautet and C. Joachim, Chem. Phys. Lett. 185 (1991) 23.

[7] P. Sautet and M.L. Bocquet, Phys. Rev. B 53 (1996) 4910.

[8] P. Sautet, Chem. Rev. 7 (1997) 1097.

[9] P.S. Weiss and D.M. Eigler, Phys. Rev. Lett. 71 (1993) 3139.

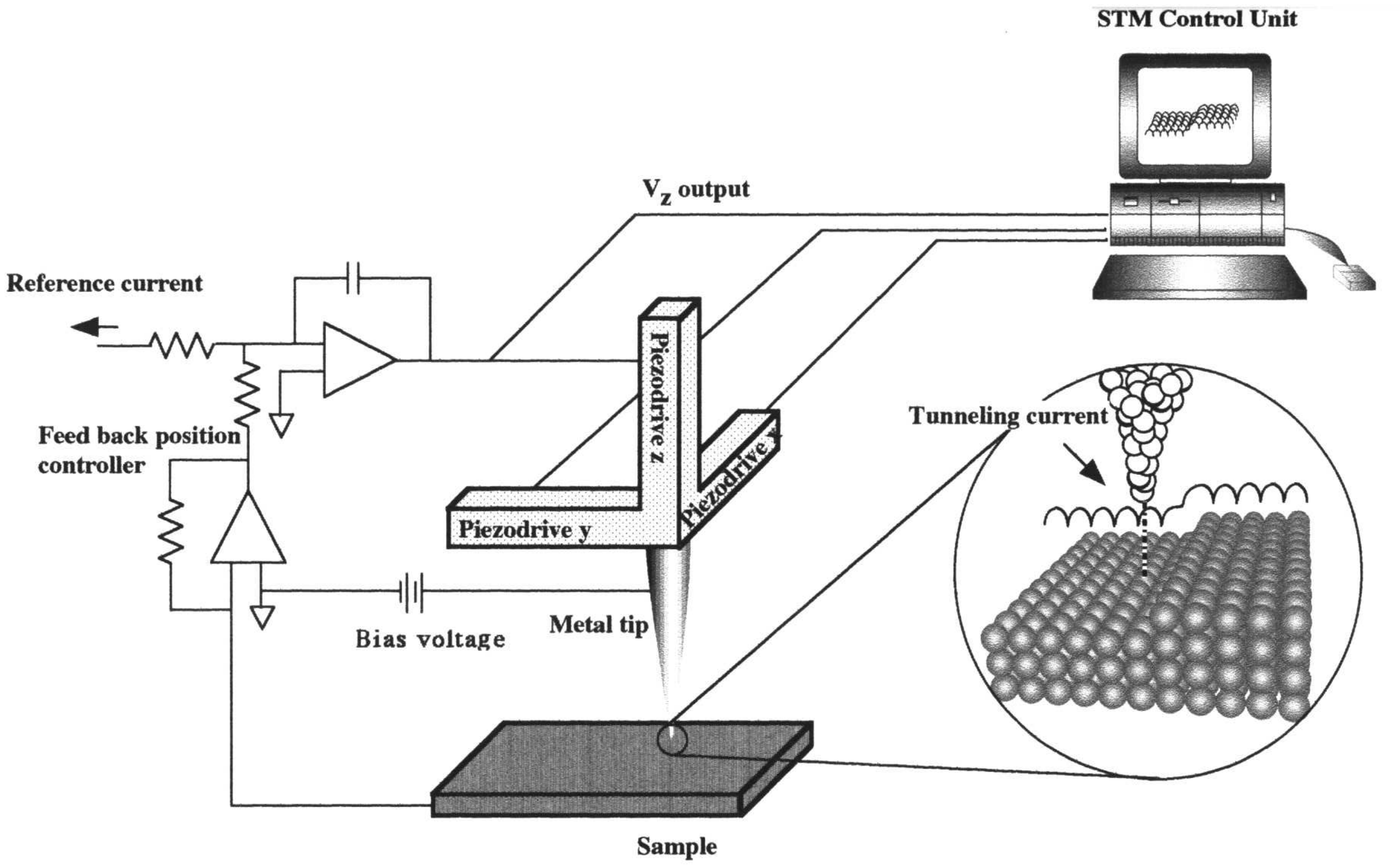

Figure 2.1 Schematic view of the scanning tunneling microscope.

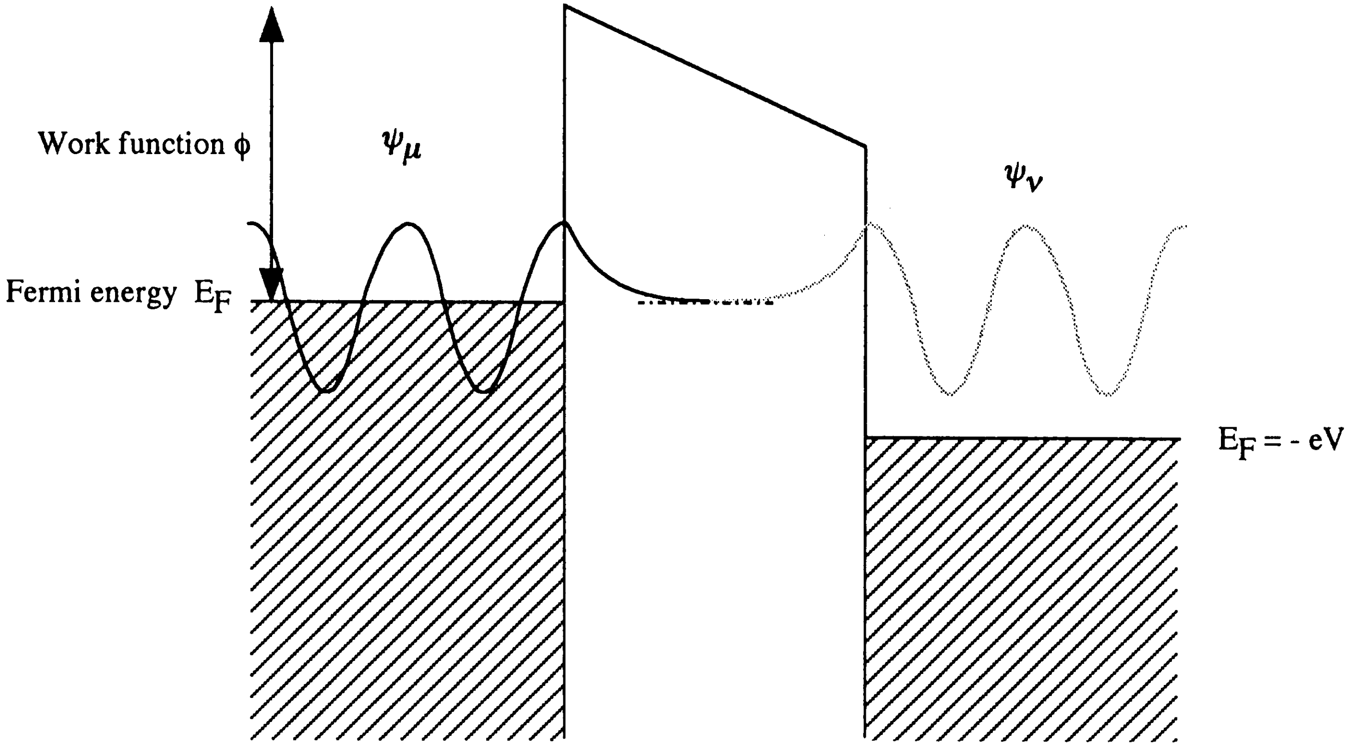

Figure 2.2 Energy diagram illustraing tunneling between two elecrodes.

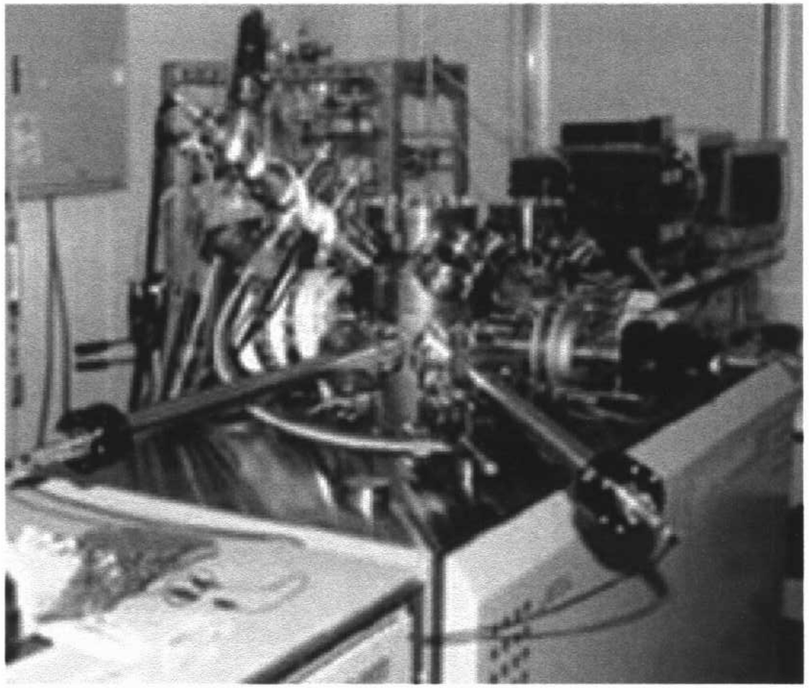

Figure 2.3 Photograph of the scanning tunneling microscope, JEOL JSTM-4500 VT

Chapter 3

Study of Pyridine and Its Derivatives Adsorbed on a TiO_2(110)-(1x1) Surface by Means of STM, TDS, XPS and MD Calculation in Relation to Surface Acid-Base Interaction

Abstract

Pyridine, benzene, 2, 6-dimethylpyridine (2, 6-DMP), and m-xylene molecules adsorbed on a TiO_2(110)-(1x1) surface were characterized by scanning tunneling microscopy, thermal desorption spectroscopy, x-ray photoelectron spectroscopy, and molecular dynamics calculation to explore structural feature of acid-base interaction which is relevant to acid-base catalysis of metal oxides. Individual pyridine and 2, 6-DMP admolecules were successfully visualized by STM at room temperature. Those probe molecules were only weakly adsorbed on the surface and desorbed near room temperature. The absence of the chemical bond between the nitrogen atoms of adsorbed pyridine and 2, 6-DMP and the Ti^{4+} atoms exposed to the surface was suggested, despite of the presence of geometric space enough for the bonding on the Ti^{4+} atoms at the surface.

3.1 Introduction

In this study, pyridine and its derivatives adsorbed on a $TiO_2(110)$-(1x1) surface have been characterized by traditional macroscopic techniques, such as thermal desorption spectroscopy (TDS) and x-ray photoelectron spectroscopy (XPS), combined with STM and molecular dynamics (MD) calculation.

Pyridine is a typical Lewis-base molecule, which is frequently employed as a probe molecule to evaluate the acid properties of oxide catalyst surfaces. The feature and strength of the interaction between probe molecule and surface acidic site reflect the character and reactivity of acid sites at oxide surfaces which are relevant to performance of oxide catalysts. There is, however, few information on atomic or molecular structures and behaviors of surface acid sites and adsorbed probe molecules. Figure 3.1 illustrates the model proposed for the stoichiometric $TiO_2(110)$-(1 x 1) truncation [2]. The model contains two types of in-plane Ti atoms: five-fold and six-fold coordinated. Protruding oxygen atoms bridge the six-fold coordinated Ti ions, forming O-ridges along the [001] axis. The alternative alignment of the exposed, five-fold coordinated Ti-rows and the bridging O-ridges results in the characteristic anisotropy on this surface.

In the acid-base points of view, the highly ionized Ti atoms exposed to the (110)-(1x1) surface are assumed to be Lewis acid sites favorable for pyridine chemisorption. The single coordination vacancy of the five-fold coordinated Ti^{4+} ion reserves space accessible by a nucleophilic reactant (Lewis base) molecule. Indeed, carboxylate anions, which are conjugate bases of the corresponding carboxylic acids, are tightly chemisorbed on the Ti atoms [2,14]. In the present study, however, it was found that pyridine was only weakly adsorbed on the surface against the acid-base assumption. Further, individual pyridine admolecules were successfully visualized by STM, though they were very mobile on the surface even at room temperature.

3.2 Experimental

Thermal desorption and XPS measurements were carried out in a ESCALAB chamber (VG) with a base pressure of 2×10^{-8} Pa. A home-built holder allowed to cool and heat a sample crystal linearly over the whole range of 100-900 K [8]. Two $TiO_2(110)$ wafers ($13\times13\times1$ mm^3, Earth Chemicals Co.) were bound to each other sandwiching a piece of tungsten mesh. The mesh was welded on a couple of electric feedthrus and resistively heated. The feedthrus were attached to a liq.N_2 reservoir to be cooled. A chromel-alumel thermocouple was fixed at an edge of the wafer with ceramic glue. The wafer was sputtered with Ar^+ ions of 5 keV and vacuum annealed at 800 K. A sharp (1x1) pattern was observed in low energy electron diffraction (LEED). Thermal desorption spectrum was observed on the wafers heated at a rate of 2 K s^{-1} on a quadrupole mass filter (UTI-200). The binding energy in Mg-Kα XPS was referred to an internal standard level, the O(1s) emission of the surface as 530.3 eV [9].

Molecular dynamics calculation was performed with commercial software (Cerius^2 version 1.6, Molecular Simulations Inc.). Dreiding II force field [10], which took account of electrostatic and van der Waals forces as molecule-surface interactions, was used with a spline switching method. A stoichiometric cluster of 8 x 8 x 4 unit cells ($Ti_{512}O_{1024}$) was used to represent the TiO_2 (110)-(1x1) surface. Net charges of Ti and O ions were assigned to +2.196e and -1.098e, respectively, according to phonon dispersion measurement [11]. Since the surface cluster atoms were fixed at initial positions during the dynamical calculations, the surface phonon excitation and hence energy exchange between admolecules and the surface were left out of consideration. To disperse the excess energy that the admolecule initially has, an isothermal condition at 4 K was employed to determine the stable adsorption structure. Charge distributions (Mulliken charge) in pyridine and benzene were separately determined as shown in Fig. 3.2 by a density functional program DMol

96.0 / 4.0.0 (Molecular Simulations Inc.). Numerical basis sets of double ζ quality plus polarization functions and the gradient-corrected exchange [12] and correlation [13] functional were used. The net charges assigned to the individual atoms were fixed during the MD calculation.

STM observation was carried out in an UHV microscope (JSTM-4500VT, JEOL) equipped with an Ar^+ gun and LEED-AES optics. A polished $TiO_2(110)$ wafer of 6.5 x 1 x 0.25 mm^3 (Earth Chemicals) was annealed in air at 1100 K for 1 h. Nickel film was then deposited on the backside of the wafer for resistive heating on the microscope stage. The temperature of the surface was monitored with an IR radiation thermometer. After cycles of Ar^+ sputtering (3 keV, 0.3 μA) and vacuum annealing at 900 K, a sharp (1x1) LEED pattern was yielded on the surface. The (1x1) surface was cooled at room temperature and then exposed to pyridine or 2, 6-dimethylpyridine (research grade, Wako Pure Chemicals) vapor in the microscope. STM images were recorded with an electrochemically etched W tip. A Positive sample bias voltage (V_s) of +2.5 V and a tunneling current (I_t) of 0.30 nA were employed unless otherwise stated.

3.3 Results and discussion

3.3.1 Thermal desorption and X-ray photoelectron spectroscopy

Thermal desorption spectra of pyridine adsorbed on a $TiO_2(110)$-(1x1) surface were observed in Fig. 3.3, where the TiO_2 surface was exposed to pyridine vapor at 150 K. The parent molecule (m/e = 79) was only desorption species. Possible products of decomposition reaction (H_2, H_2O, CO and CO_2) were watched, but not detected. Figure 3.3 shows a series of spectra with increasing exposure. Two desorption peaks of pyridine were observed at 270 and 220 K. An additional peak appeared at 160 K with larger exposure in spectra d and e. The activation energies of the desorption events (E_d) at 270, 220, and 160 K were estimated to be 70, 60 and 40 kJ/mol, respectively, by assuming the first-order desorption kinetics and a preexponential factor of 10 s^{-1} [6]. The additional peak at 160 K was attributed to multilayer condensation of pyridine ice, because that peak was developed without saturation at further exposures. On the other hand, the two peaks at the higher temperatures were assignable to desorption of pyridine molecules in direct contact with the surface.

The amount of the pyridine molecules in contact was quantified with XPS measurements. The coverage of carbon and nitrogen atoms (θ_X and θ_N) was determined on the basis of the intensity of C(1s) and N(1s) signals relative to that of O(1s) emission of the substrate. The (2x1)-ordered formate (HCOO) monolayer was also employed as a standard of 2.6 carbon atoms per nm^2. The estimated atom coverages of the saturated pyridine monolayer prepared at 170 K are listed in Table 1. Based on the atom coverage, molecule coverage of pyridine was estimated to be 2 molecules nm^{-2}. This indicates that pyridine molecules were adsorbed on (110) terraces of the surface, not only specific sites such as steps, vacancies, etc., because the population of singularities resident on the single crystal surface is much more minor.

The binding energies of C(1s) and N(1s) are also shown in Table 1. Pyridine molecules in multilayered ice at 130 K gave C(1s) and N(1s) emissions at 400.3 and 285.9 eV. They are identical to those of monolayer species within experimental uncertainty of 0.2 eV. This suggests weak interaction between the pyridine monolayer and the TiO_2 surface. The negligible shift in N(1s) binding energy, in particular, suggests the absence of N-Ti chemical bond, which is contrasted to the traditional assumption on acid-base type adsorption [14].

The weak interaction between the nitrogen atom in pyridine and the Ti^{4+} ion exposed to the surface is supported by thermal desorption results of benzene. Figure 3.4 shows a series of benzene desorption (m/e=78) following exposure of benzene on the (1x1) surface at 150 K. The desorption spectra of benzene were quite similar to those of pyridine. Two peaks were developed at 220 and 260 K without multilayer condensation in the case of benzene. The identical desorption features demonstrate that pyridine-surface interaction is very similar to benzene-surface interaction, and hence the absence of N-Ti chemical bond.

To examine the contribution of the N-Ti bonding interaction to the adsorption process, further, 2, 6-dimethylpyridine (2, 6-DMP) was employed as a probe molecule. Two methyl groups at the ortho positions hinder the nitrogen atom from effective approach to the Ti^{4+} Lewis acid sites. If the direct N-Ti bonding played a major role in adsorption, 2, 6-DMP would be less strongly adsorbed on the TiO_2 surface as compared with pyridine. However, this was not the case. Desorption of 2, 6-DMP was observed at 260 and 340 K, as shown in Fig. 3.5. Sharp peak at 170 K was ascribed to the desorption of multilayered pyridine. The desorption temperatures of 2, 6-DMP directly adsorbed on the surface shifted to higher temperatures by 40-80 K, compared with the spectra of pyridine in Fig. 3.3. The estimated atom coverages of 2, 6-DMP monolayer prepared at 190 K are listed in Table 1. The values were a little smaller than those for pyridine, while similar to those for *m*-xylene.

The TDS results of pyridine, benzene, and 2, 6-DMP demonstrate that N-Ti direct interaction plays only minor role in the adsorption of these compounds. Thermal desorption results of *m*-xylene (Fig. 3.6), the nitrogen-free equivalent of 2, 6-DMP, support the picture. The presence of the nitrogen atom gave no effect in desorption temperatures of 2, 6-DMP and m-xylene. Instead of N-Ti bond formation, electrostatic and van der Waals forces should play a major role in the adsorption of the compounds. Hence, the adsorption states of these four compounds can be classified as physisorbed states, though their heat of adsorption was estimated at 60 kJ/mol or more, somewhat larger than the limit of physisorption (~10 kcal/mol) in the traditional definition.

It is a quite interesting and important issue why the Ti^{4+} ions on TiO_2(110)-(1x1) do not show Lewis acidity. There are one-dimensional grooves composed of five-fold coordinated Ti^{4+} ions between the protruding oxygen ridges, as shown in Fig. 3.1. The O-ridges are separated by 0.649 nm. Assuming hard spheres of the van der Waals radius (0.152 nm) [17] for bridge-oxygen atoms, space of 0.345 nm in width is still reserved on the five-fold coordinated Ti atoms in the groove. Therefore it would have been expected that the electron-rich nitrogen atom of a pyridine molecule could approach and chemically interact with the Ti^{4+} ions, since the van der Waals radius of nitrogen atom is 0.155 nm [17]. That indicates inactivity was not related to steric hindrance of the O-ridges, but perhaps repulsive force come from the O-ridges, or electronic states localized over the Ti sites.

3.3.2 Molecular dynamics calculation

The TDS and XPS results presented in the previous section indicate no formation of specific N-Ti chemical bond in the adsorption of pyridine on TiO_2(110). Thus, the adsorption of pyridine and benzene was simulated with molecular dynamics (MD) calculation taking account of electrostatic and van der Waals forces as molecule-surface interactions.

The energy minimized calculation of a single pyridine molecule adsorbed on a $Ti_{512}O_{1024}$cluster was performed. The atoms in the surface cluster were fixed at the positions determined by surface x-ray diffraction [3], where the exposed Ti atoms are pulled down into the surface by 0.016 nm relative to the ideal (110) truncation. The adsorption energy of pyridine was determined as the energy difference between the adsorbed state calculated at 4 K and the non-adsorbed state where the molecule is put away from the surface cluster. Table 2 shows the total adsorption energy (E), electrostatic force component of E (E_e), and van der Waals force component of E (E_{vw}). The calculated total adsorption energy, 84 kJ/mol, is in agreement with the value estimated in TDS, 70 kJ/mol. This agreement supports that the adsorption phenomenon is properly reproduced in the calculation. The adsorption energy of benzene was calculated in a similar manner. The small difference of 9 kJ/mol in E is consistent with the identical peak temperatures observed in TDS (Fig. 3.3 and Fig. 3.4).

Adsorption structures of pyridine and benzene were also determined in the calculation. Pyridine and benzene molecules were most stable when they were placed on an exposed Ti-row with their aromatic ring parallel to the surface, as illustrated in Fig. 3.7. The electrostatic component mainly comes from the attraction between the highly ionized Ti atoms and the negative charge localized on the aromatic ring of pyridine or benzene. The negative charge on the nitrogen atom in pyridine enhanced the electrostatic attraction by 12 kJ/mol, and total adsorption energy increased by 9 kJ/mol, as a result. The ring plane of the pyridine admolecule was slightly inclined by 1.6 degree from the parallel. Electrostatic interaction weakly operates between the N atom and the Ti atom at a rather long distance of 0.344 nm. On the other hand, a much shorter N-Mo distance of 0.201 nm for pyridine π-bonded on a MoS_2 surface has been concluded by a CNDO calculation [15].

To evaluate the effect of relaxation in the substrate surface, the adsorption on the surface cluster of unrelaxed, ideal (110) truncation was also examined by the MD calculation. The calculated adsorption energy terms are shown in Table 2 in parentheses. The electrostatic terms were nearly twice as large as those on the relaxed surface, while van der Waals components remained unchanged. The five-fold coordinated Ti atoms are pulled down and shielded by in-plane oxygen atoms in the relaxed structure [3]. The present study demonstrates that surface relaxation has to be considered in simulating the adsorption on metal oxide surfaces.

3.3.3 Scanning Tunneling Microscopy

Figure 3.8 shows typical constant current STM images of a pyridine-exposed TiO_2(110) surface. Figure 3.8a was observed on a surface exposed to 3 L pyridine vapor at room temperature. Adsorbed pyridine molecules were traced as many bright spots. Fragmented shapes of the molecular image suggest vital migration of adsorbed pyridine molecule. When an adsorbed molecule migrates quickly, its whole shape cannot be imaged with scanning microscopy. The number of pyridine images (bright spots) reduced with time when the surface was maintained at room temperature on the microscope stage. The observed depopulation is ascribed to the desorption, since the desorption of pyridine occurs at room temperature as shown in the TPD spectra. On the other hand, the number of pyridine images increased with scan time, when a same area was continuously scanned.

Some streaks parallel to the scan direction were observed in Fig. 3.8a and suggest a tip-molecule interaction. The scan direction was parallel to the steaks. However, the tip-molecule interaction is seemed to play only a secondary role in the migration of pyridine on the surfaces with lower pyridine coverages as shown in Fig. 3.8b and 3.8c, where the streaks along the scan direction were observed much less frequently.

Figures 3.8b and 3.8c were sequentially recorded on the same surface area at a 23 s interval at 5 h after Fig. 3.8a was measured. The pyridine density decreased due to the desorption and individual admolecules were well resolved. The average height of the pyridine image was 0.26 nm with cross-section analysis. In addition to the pyridine images, regular rows were also imaged with slight contrast. The rows parallel to the [001] direction are the rows of Ti atoms exposed to the surface [4, 5]. The bright spots were always located on the Ti rows, while they were migrating frame by frame. This suggests that the admolecules mainly stayed on the Ti atoms, though they were mobile at this temperature.

Constant current images including Fig. 3.8 were determined with a positive sample bias voltage of +2.5 V. The observed topographies are regarded to represent the shape of unoccupied states localized on adsorbed pyridine molecules. The lowest unoccupied molecular orbitals (LUMOs) of a free pyridine molecule are nearly degenerated π^* states of the aromatic ring, $3b_1$ and $2a_2$ at 3.0 eV above the vacuum level [16]. The observed topography on the Ti rows is reproduced by assuming the electron tunneling into the LUMOs and the structure predicted with the MD calculation (Fig. 3.7). Molecular imaging by tunneling to LUMO has been claimed in formate- [7] and acetate- [1] adlayers on this surface.

Sequential constant current images of 2, 6-DMP molecules adsorbed on the $TiO_2(110)$ surface are shown in Fig. 3.9, where the TiO_2 surface was exposed to 0.03 L of 2, 6-DMP at room temperature. Adsorbed molecules were again observed at on-top positions of the Ti rows. In contrast to pyridine, 2, 6-DMP molecules were much less mobile on the $TiO_2(110)$ surface. Most of them were observed at the same positions in the sequential frames taken at an 88 s interval as shown in Figs. 3.9a and 3.9b. The minority of the bright spots migrated at a short distance in the [001] direction between Fig. 3.9a and Fig. 3.9b. In the case of the STM images of 2, 6-DMP, however, fragmented topography due to migration of admolecules was not almost observed. Hence, the distorted topography may reflect the intramolecular structure. The less mobility of 2, 6-DMP is in accordance with the larger adsorption energy observed with TDS. Individual Ti atoms were resolved at the surface with 2, 6-DMP admolecules in a small area scan as shown in Fig. 3.9c. The relative position of admolecules is deduced from the image. The center of the 2, 6-DMP molecule is located on the Ti-row along the [001] axis but between adjacent Ti atoms in the row.

These results demonstrate that weakly adsorbed molecules like pyridine on $TiO_2(110)$ can be imaged by STM. On this surface, the imaged pyridine molecules are ready to desorb from the surface at room temperature. This suggests that metal oxide surface is very promising substrate to image weakly adsorbed and hence mobile admolecules and reaction intermediates. The adsorption energy of pyridine obtained by the MD calculation was 84 kJ/mol as already mentioned. This is contrasted to the fact that admolecules more strongly bound to metal surfaces are often invisible by STM due to the large mobility parallel to the surface. The ionic property of the metal oxide surface yields a relatively high barrier against surface migration.

3.4 Conclusions

(1) Adsorption of pyridine, benzene, 2, 6-DMP, and *m*-xylene on the $TiO_2(110)$-(1x1) surface which has the alternative alignment of the exposed, five-fold coordinated Ti^{4+} (Lewis acid site) rows and the protruding bridging oxygen ridges, was investigated to give an insight into structural aspect and bonding feature in acid-base interaction on a metal oxide surface by STM, TDS, XPS, and MD calculation.

(2) Physisorbed pyridine and 2, 6-DMP have been successfully visualized by STM. Fragmented shapes of the molecular image suggest vital migration of adsorbed pyridine molecules at room temperature. It is to be noted that STM can resolve and trace the individual pyridine molecules which are mobile on the oxide surface. The migration of 2, 6-DMP was much slower than that of pyridine.

(3) The MD calculation of a single pyridine molecule adsorbed on a $Ti_{512}O_{1024}$cluster shows similar adsorption energy to that for benzene. The calculation also revealed that both molecules were most stable when the face of the molecules is parallel to the surface. The nitrogen atom in pyridine is located at the distance of 0.344 nm far from the nearest Ti atoms.

These results on STM and MD calculation coincide with the TDS and XPS data.

(4) The TDS peaks for pyridine and 2, 6-DMP are similar to those for the corresponding aromatics, benzene and *m*-xylene.

(5) The XPS binding energies of N 1s for adsorbed pyridine and 2, 6-DMP are almost the same as those for multilayered ice of the corresponding compounds.

(6) The comprehensive data give a picture for weakly adsorbed structures of pyridine and 2, 6-DMP without chemical bonding between the N atom and the Lewis acidic Ti^{4+} atom in the groove of $TiO_2(110)$ surface, in spite of the accessible space on the five-fold coordinated Ti^{4+} atom to the N atom of the basic compounds.

(7) Thus, the origin of strong acid-base interaction at oxide catalyst surfaces may involve more complicated structural factors in addition to a simple Coulombic interaction between highly ionized metal atom and nucleophilic reactant.

References

[1] H. Onishi, Y. Yamaguchi, K. Fukui and Y. Iwasawa, J. Phys. Chem. 100 (1996) 9582.

[2] V.E. Henrich and P.A. Cox, The Surface Science of Metal Oxides, Cambridge University Press., Cambridge, 1994.

[3] G. Charlton, P.B. Howes, C.L. Nicklin, P. Steadman, J.S.G. Taylor, C.A. Muryn, S.P. Harte, J. Mercer, R. McGrath, D. Norman, T.S. Turner and G. Thornton, Phys. Rev. Lett. 78 (1997) 495.

[4] H. Onishi, K. Fukui and Y. Iwasawa, Bull.Chem. Soc. Jpn. 68 (1995) 2447.

[5] H. Onishi and Y. Iwasawa, Surf. Sci. Lett. 313 (1994) L783.

[6] F.M. Leibsle, P.W. Murray, N.G. Condon and G. Thornton, J. Phys. D Appl. Phys. 30 (1997) 741.

[7] H. Onishi and Y. Iwasawa, Chem. Phys. Lett. 226 (1994) 111.

[8] H. Onishi, T. Aruga and Y. Iwasawa, J. Catal. 146(1994) 557.

[9] H. Onishi, T. Aruga, C. Egawa and Y. Iwasawa, Surf. Sci. 193 (1988) 33.

[10] S.L. Mayo, B.D. Olafoson and W.A.G. III, J. Phys. Chem. 94 (1990 8897.

[11] J.G. Traylor, H.G. Smith, R.M. Nicklow and M.K. Wilkinson, Phys. Rev. B 3 (1971) 3457.

[12] A.D. Becke, Phys. Rev. A 38 (1988) 3098.

[13] J.P. Perdew and Y. Wang, Phys. Rev. B 45 (1992) 13244.

[14] K. Tanabe, H. Hattori, T. Yamaguchi and T. Tanaka, Acid-Base Catalysis, Kodansha Ltd., Tokyo, 1988.

[15] E.N. Roudríguez-Arias, A.E. Gainza, A.J. Hernández, P.S. Lobos and F. Ruette, J. Mol. Catal. A 102 (1995) 163.

[16] W.L. Jorgensen and L. Salem, in The Organic Chemist's Book of Orbitals, Academic Press,

1973, p. 263.

[17] A. Bondi, J. Phys. Chem. 68(1964) 441.

Table 1. XPS binding energies and estimated coverages of pyridine and derivatives adsorbed at saturation on a $TiO_2(110)-(1x1)$ surface. The TiO_2 surface was exposed to the compounds at temperatures shown in parentheses.

Adsorbate	C(1s) B.E. /eV	θ_C / atom · nm^{-2}	N(1s) B.E. /eV	θ_N / atom · nm^{-2}
Pyridine (170 K)	286.1	11	400.5	1.7
Benzene (170 K)	284.3	5		
2,6-DMP (190 K)	285.5	10	399.5	1.3
m-xylene (200 K)	284.3	9		

Table 2. Energy terms predicted in the MD calculation; E: total adsorption energy, Ee: electrostatic component of E, and Evw: van der Waals component of E. The values in parentheses are energy terms calculated for the adsorption on an unrelaxed surface.

Adsorbate	E / kJ mol-1	E_e / kJ mol-1	E_{vw} / kJ mol-1
Pyridine	84(122)	53(104)	31(18)
Benzene	75(105)	41(79)	34(26)

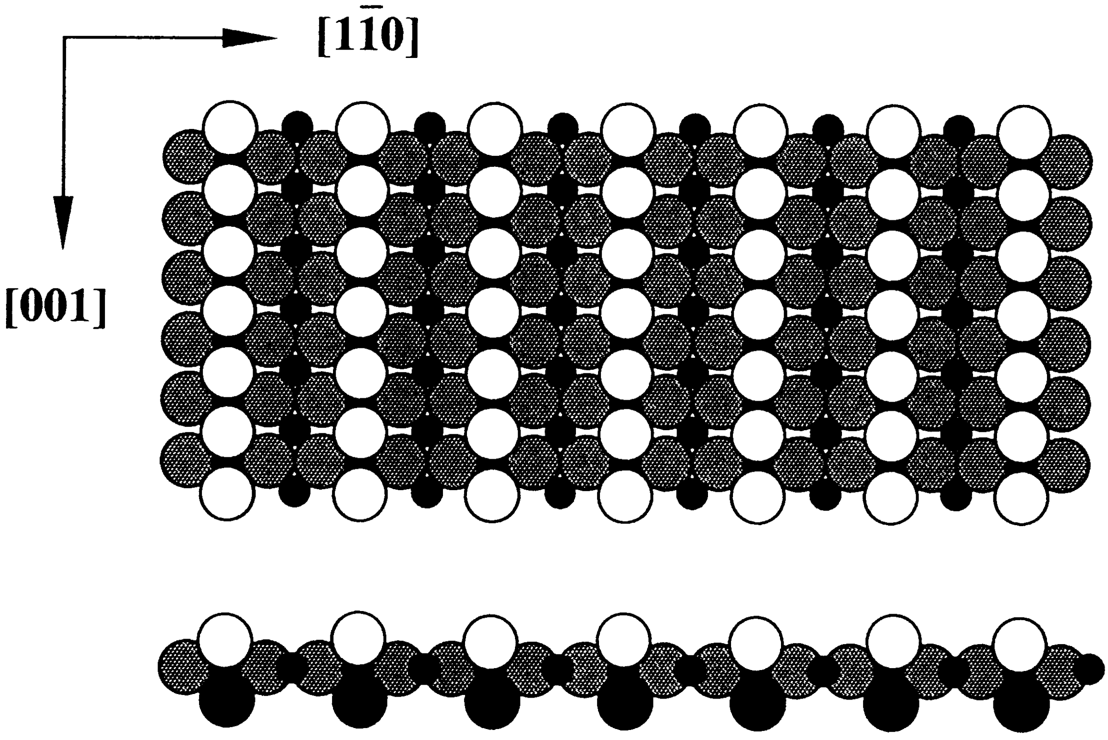

Figure 3.1 The model of TiO_2(110)-(1x1) surface (top and side views). Filled and open symbols represent titanium and oxygen atoms, respectively.

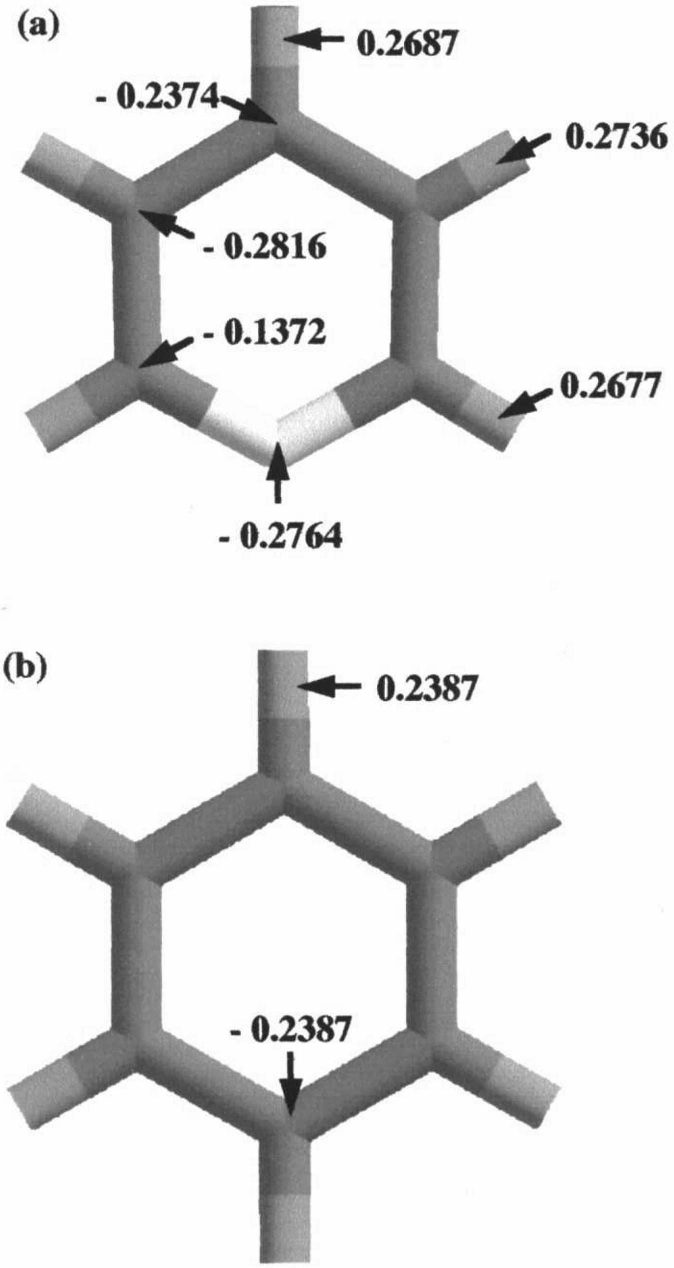

Figure 3.2 Charge distributions of a free pyridine (a), and a free benzene (b) determined by the energy minimized calculation with DMol software.

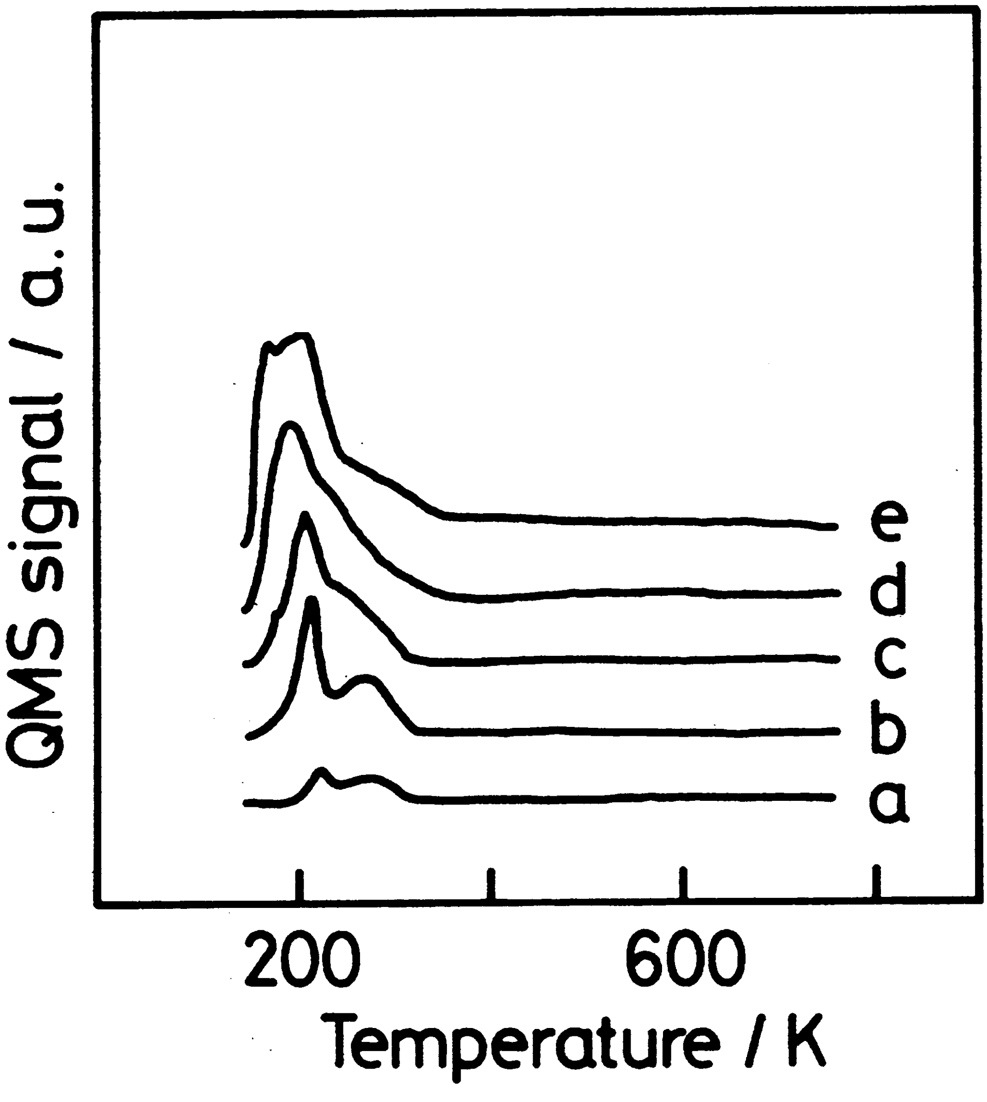

Figure 3.3 Thermal desorption spectra (m/e =79) following adsorption of pyridine at 150 K with increasing exposure time; a: 0.1 L, b: 0.2 L, c: 0.7 L, d: 1.4 L, and e: 3.8 L.

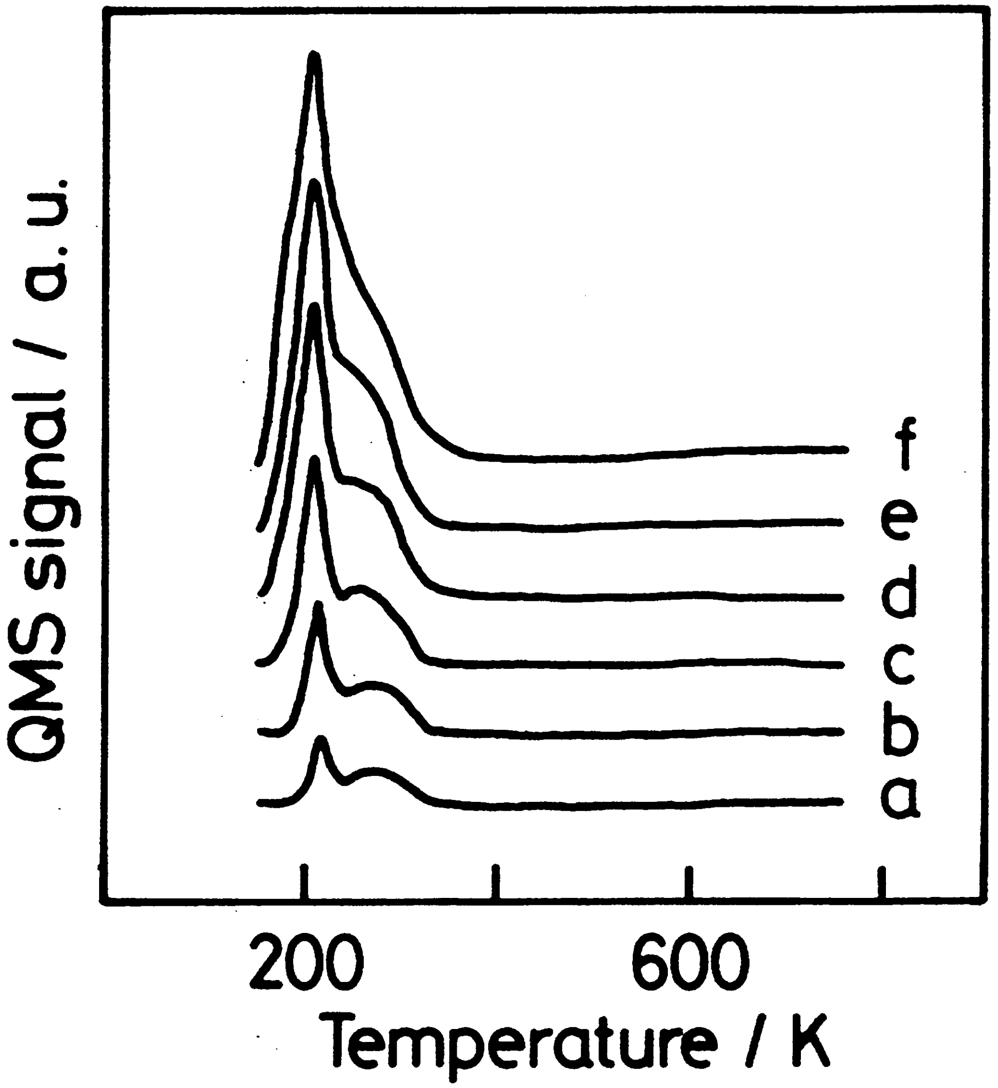

Figure 3.4 Thermal desorption spectra (m/e =78) following adsorption of benzene at 150K. Estimated exposure; a: 0.1 L, b: 0.2 L, c: 0.3 L, d: 0.5 L, e: 0.6 L, and f: 0.7 L.

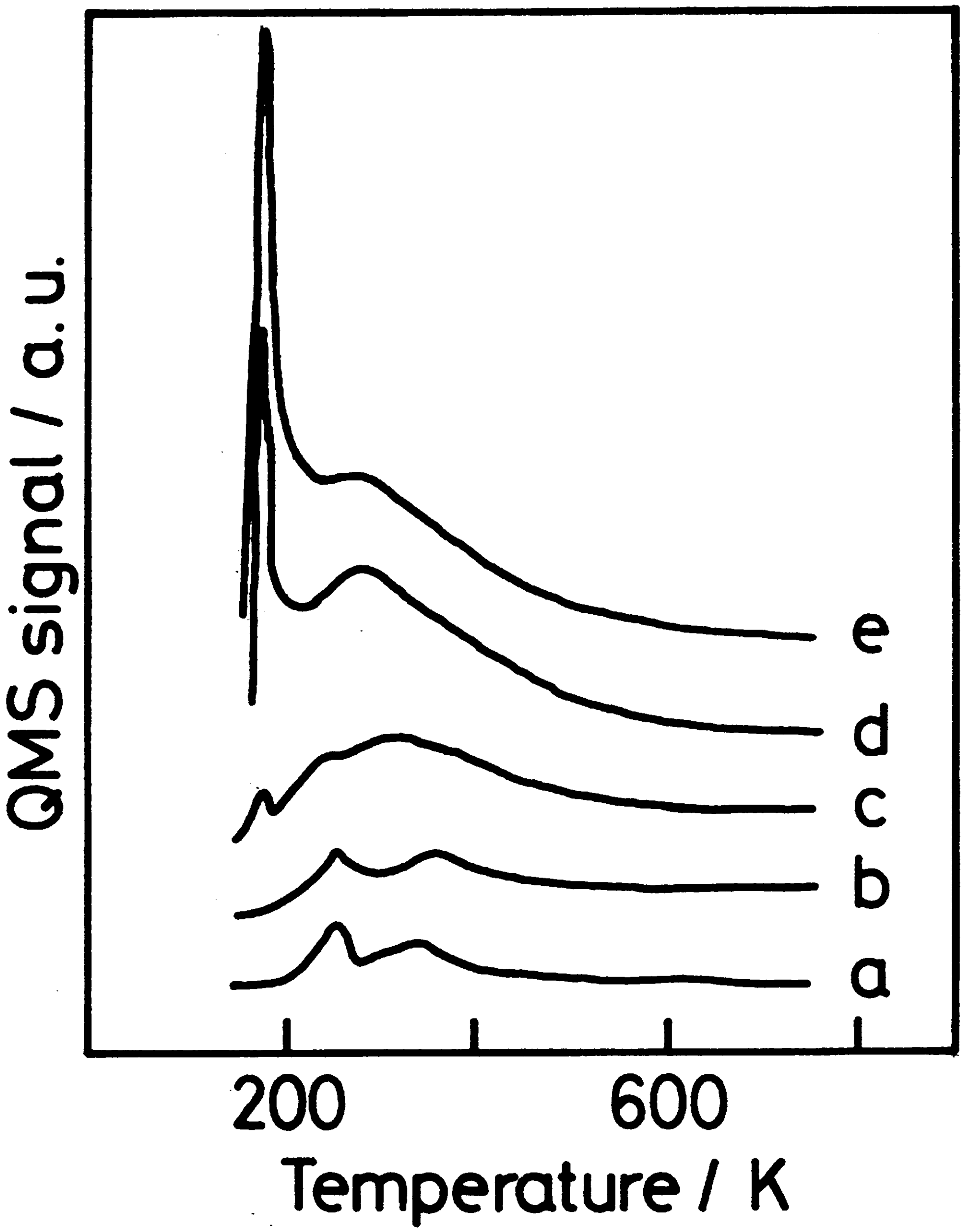

Figure 3.5 Thermal desorption spectra (m/e =107) following adsorption of 2, 6-dimethylpyridine at 150 K. Estimated exposure; a: 0.1 L, b: 0.2 L, c: 0.3 L, d: 0.5 L, and e: 1.0 L.

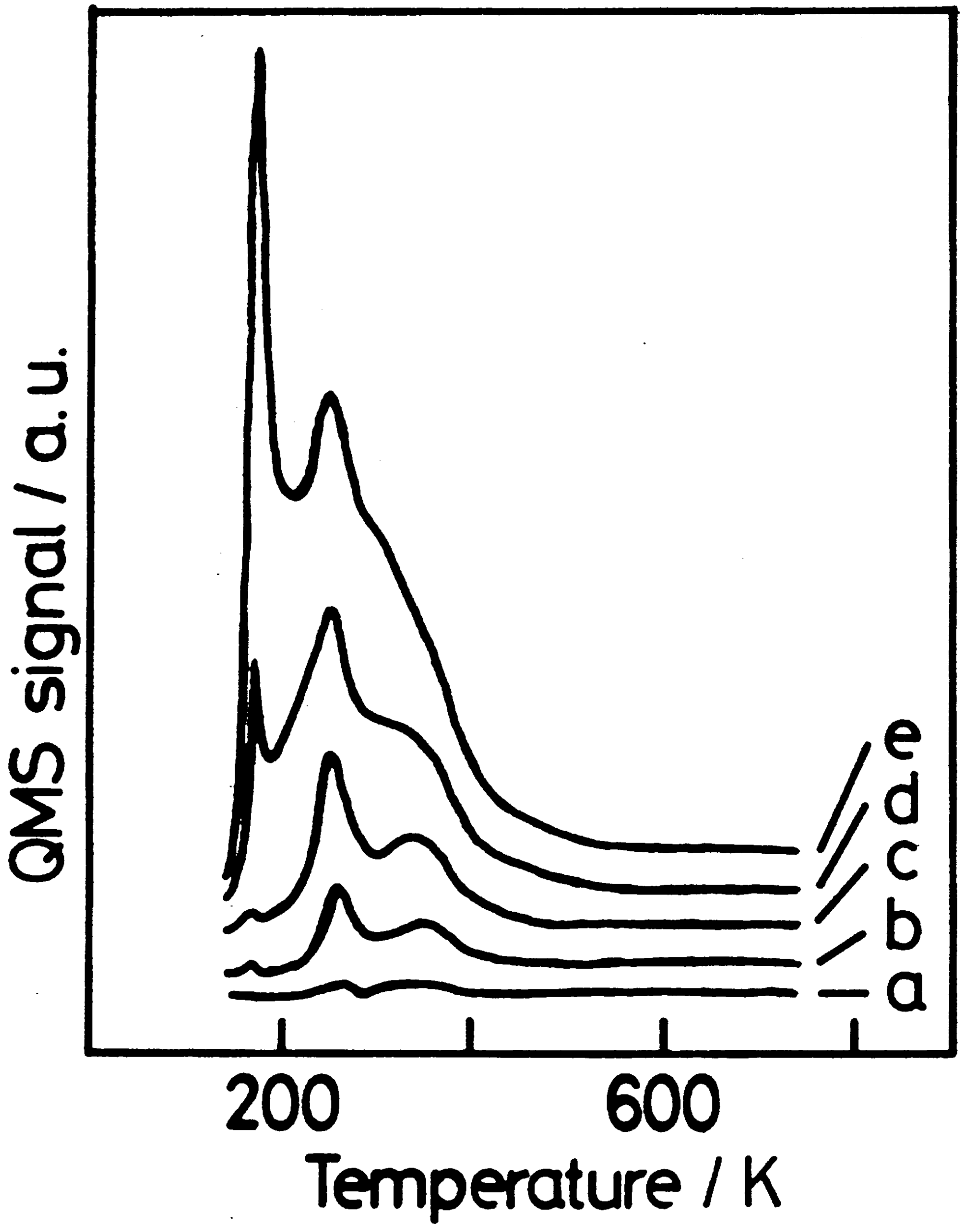

Figure 3.6 Thermal desorption spectra (m/e =106) following adsorption of m-xylene at 140 K. Estimated exposure; a: 0.1 L, b: 0.2 L, c: 0.3 L, d: 0.5 L, and e: 1.0 L.

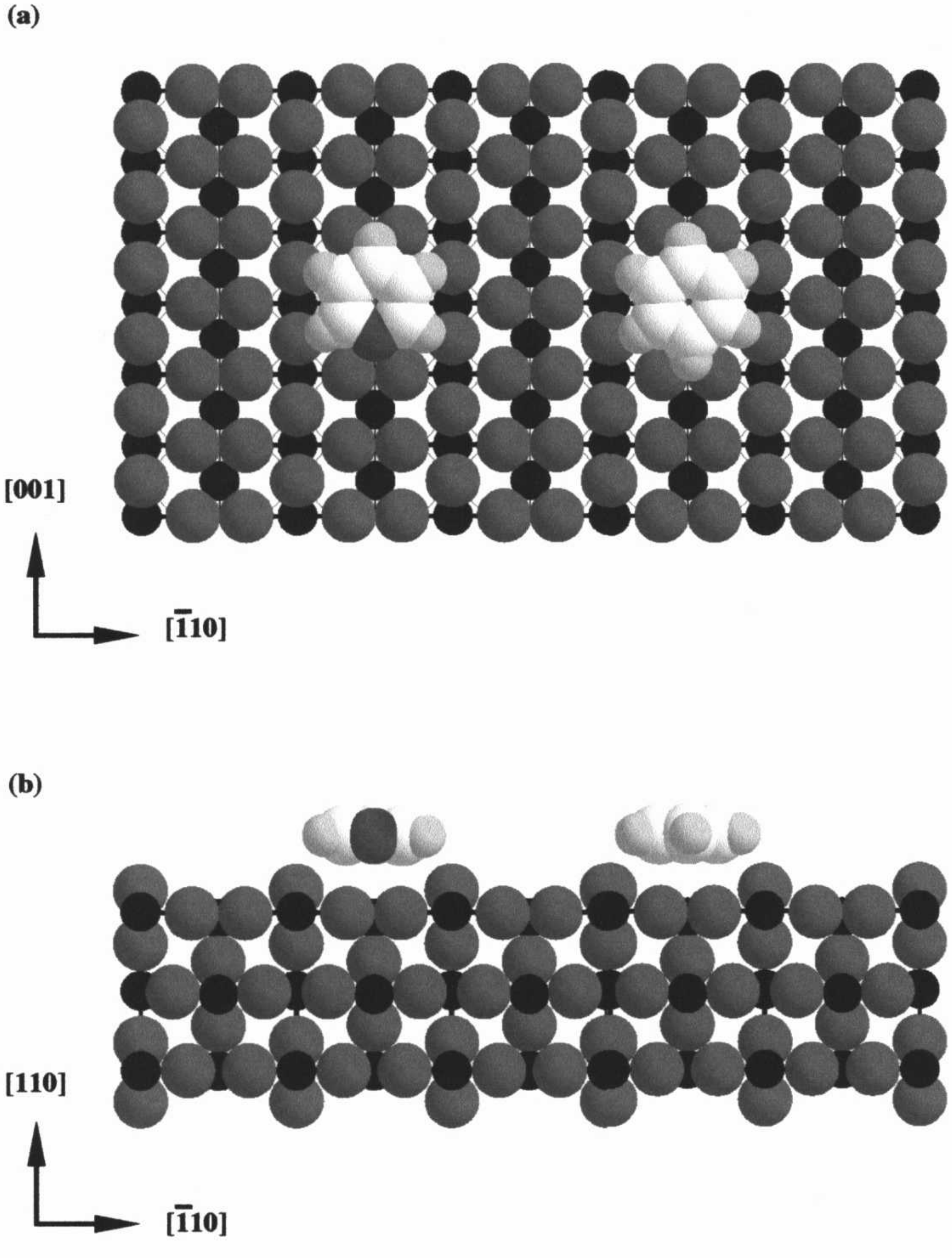

Figure 3.7 The structures of a pyridine molecule (left) and a benzene molecule (right) adsorbed on the $TiO_2(110)$-(1x1) surface predicted by molecular dynamics calculation. (a) top and (b) side views of a part of the $Ti_{512}O_{1024}$ surface cluster are shown with the admolecules. Titanium and oxygen atoms of the surface cluster are presented with filled and shaded symbols.

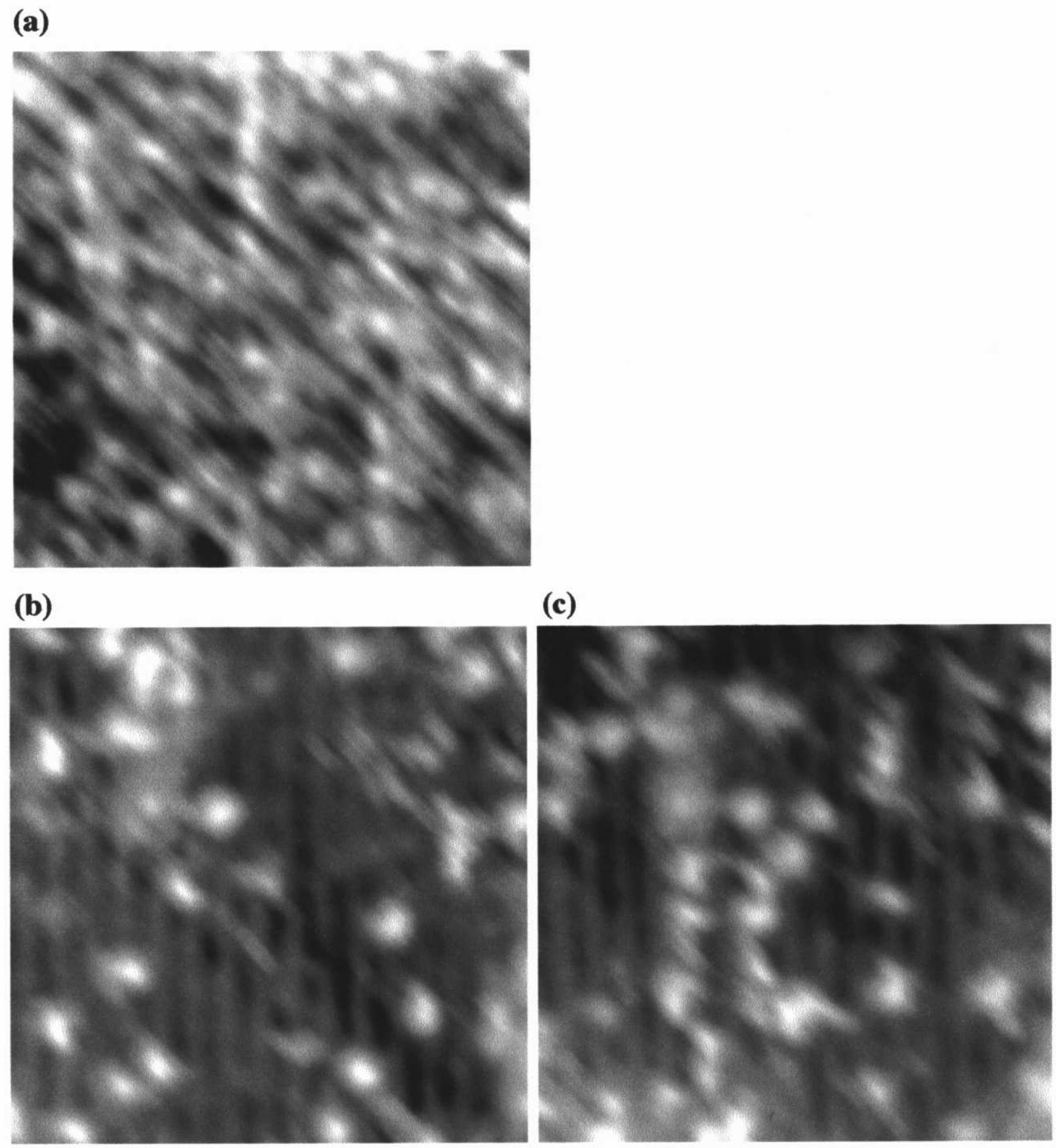

Figure 3.8 Constant current STM images of a pyridine-exposed TiO_2(110)-(1x1) surface. Image (a) was recorded at room temperature on the surface exposed to 3 L pyridine vapor. Images (b) and (c) were sequentially recorded at an interval of 23 s on the same surface at 5 h after the image (a)was measured. sample bias voltage: +2.5 V, tunneling current: 0.30 nA, 10x10 nm^2.

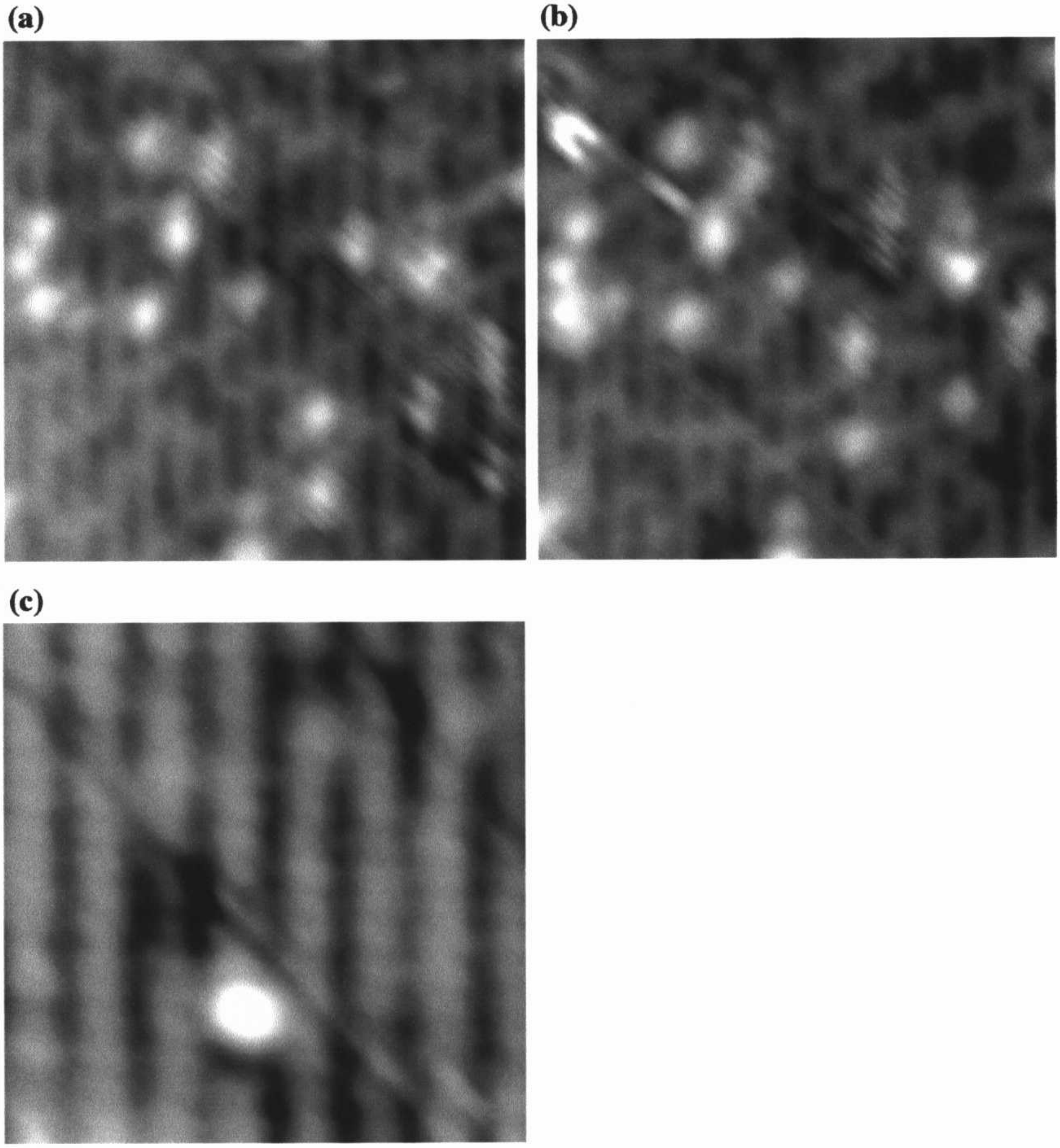

Figure 3.9 Constant current STM images of a 2, 6-dimethylpyridine-exposed $TiO_2(110)$-(1x1) surface. The surface was exposed to 0.03 L 2, 6-dimethylpyridine vapor at room temperature. Images (a) and (b) were sequentially determined at an interval of 88 s. sample bias voltage: +2.0 V, tunneling current: 0.30 nA, 10x10 nm^2. Imges (c) is a zoomed-in image (5x5 nm^2) of the surface.

Chapter 4

STM Visualization of Site-Specific Adsorption of Pyridine on $TiO_2(110)$

Abstract

Pyridine molecules adsorbed on a $TiO_2(110)$-(1x1) surface were visualized by scanning tunneling microscopy (STM). Direct evidence of coordination-controlled adsorption on a metal oxide surface is reported for the first time. A pyridine molecule was more strongly adsorbed on a four-fold coordinated Ti atom exposed at single-atom-height step edges than on the five-fold coordinated Ti site over the perfect (110) terrace. Furthermore, the activity of the four-fold coordinated Ti sites at step edges was strongly dependent on the orientation of the step in azimuth. Sequential imaging of the pyridine-exposed surface revealed that terrace-adsorbed molecules were transformed to step-bonded species and vice versa even at room temperature.

4.1 Introduction

The adsorption of pyridine specific to single-atom height steps resident on a metal oxide surface has been visualized in the present study. Pyridine is a typical Lewis-base compound and employed as a probe for the acid properties of oxide catalysts. The quality and quantity of acid sites have been often analyzed with thermal desorption and infrared absorption spectroscopy. Despite a number of studies with the macroscopic techniques, the atomic-scale structure of acid sites is still unclear. As is demonstrated in Chapter 3, pyridine was only weakly adsorbed, perhaps physisorbed on the (110)-(1x1) surface of rutile TiO_2 without definite N-Ti bonding, although the highly ionized Ti atoms exposed on that surface could be assumed as Lewis acid sites favorable for pyridine chemisorption. Visualization of individual probe molecules adsorbed on different parts of a metal oxide surface, which is performed in the present study for the first time, is indispensable for rational design of acid sites with controlled reactivity.

4.2 Experimental

The experiments were performed with an UHV compatible scanning tunneling microscope (JSTM-4500VT, JEOL) equipped with an Ar^+ gun and LEED-AES optics. A polished $TiO_2(110)$ wafer of 6.5 x 1 x 0.25 mm^3 (Earth Chemicals) was annealed in air at 1100 K for 1 h. Nickel film was then deposited on the back side of the wafer for resistive heating on the microscope stage. The temperature of the surface was monitored with an IR radiation thermometer. After cycles of Ar+ sputtering (3 keV, 0.3 μA) and vacuum annealing at 900 K, a sharp (1x1) LEED pattern was observed on the surface. The (1x1) surface was cooled to room temperature and then exposed to pyridine (research grade, Wako Pure Chemicals) vapor. Constant current topography of the pyridine-exposed surface was continuously determined at room temperature with an electrochemically etched W tip. A positive sample bias voltage (V_s) of +2.5 V, and a tunneling current (I_t) of 0.05 nA were employed in imaging.

4.3 Results and Discussion

The annealed (1x1) surface was exposed to pyridine vapor of 0.01 L at room temperature in the treatment chamber and then transferred to the microscope stage. Figure 4.1a shows a typical STM topography of the pyridine-exposed TiO_2(110)-(1x1) surface, where two terraces separated with single-atom height steps were imaged. Fig. 4.1b illustrates the position and azimuthal orientation of the step edges. Fifteen protrusions of complete circular shape were observed on the edges. These protrusions were assigned to individual pyridine admolecules. The step-bonded molecules were imaged completely, whereas many images of fragmented shapes were observed over the upper terrace. The fragmented shapes of molecular image suggests vital migration of pyridine molecules adsorbed on the terrace, because a quickly migrating molecule cannot stay at a position long enough to be properly imaged with scanning microscopy. Indeed, terrace-adsorbed pyridine molecules frozen at about 100 K could be resolved as isolated protrusions of the complete shape [3]. Our previous work showed that the five-fold coordinated Ti^{4+} sites exposed on the (110)-(1x1) terrace are incapable of making stable Ti-N bonds with pyridine admolecules [2]. The step-bonded species of the complete shape were less mobile at room temperature and thus more strongly bound to the surface, than the terrace-adsorbed species were. The residence time at the step edges was the order of 100 s, as shown later.

The rows of the five-fold coordinated Ti^{4+} atoms (Ti-rows) were resolved as lines of slight contrast on the upper terrace in Fig. 4.1a. It has been well established that the exposed Ti atoms are imaged as small protrusions in STM topography determined with positive sample bias voltages [1]. The step-bonded pyridine molecules were always observed at positions where the steps truncated Ti-rows. Four-fold coordinated Ti atoms should be exposed at those intersections. The Ti atom originally five-fold coordinated loses one oxygen ligand at a step edge. A step parallel to the $[11\bar{2}]$ direction is illustrated in Fig. 4.2 as an example. The coordination number around Ti atoms was maximized in the model with the least number of four-fold coordinated Ti atoms and no three-fold coordinated Ti atoms. A bulk truncation without any reconstruction or relaxation was assumed. It is thus concluded that a pyridine molecule is adsorbed more strongly on a coordinatively unsaturated (four-fold coordinated) Ti atom exposed on the step edge, than on a five-fold coordinated Ti atom over the (110)-(1x1) terrace.

A possible interpretation of the adsorption state specific to the step edges is that the unsaturated (four-fold) coordination promotes the Lewis-acid strength of the Ti site. A molecular dynamics (MD) calculation considering electrostatic and van der Waals forces between the step site and a single pyridine molecule failed to reproduce the observed state [3], while a weakly bonded state on a perfect (110) terrace was well presented in the calculation [2]. Hence, chemical bonding interaction, i.e. acid-base type interaction in this case, may play a role in the adsorption at the step edges.

On the other hand, the step-bonded state exhibited topography very similar to that of the terrace-adsorbed species, when the surface migration of the latter was frozen out at 100 K [3]. The image height of both the states at 100 K was determined to be 0.25±0.01 nm. The MD calculation of a single pyridine molecule adsorbed on a perfect (110) terrace revealed that the adsorbed pyridine was most stable when the aromatic ring is parallel to the surface [2]. If the step-bonded pyridine molecule is adsorbed with a N-Ti chemical bond, the aromatic ring should stand up relative to the terrace plane. Pyridine adsorbed in this manner was found on a ZnO$(10\bar{1}0)$ surface in an X-ray absorption study [4]. The topographical similarity of the step-bonded and terrace-adsorbed species does not suggest the upright geometry of the step-bonded state. The adsorption geometry stable at the step site and the contribution of N-Ti chemical bond are now being examined with a density functional method [3].

It has been pointed out that the multiplicity of coordination vacancy is a key factor controlling the reactivity of the metal centers of metal oxides [5]. The present study yields direct evidence of coordination-controlled adsorption on a metal oxide surface for the first time. Furthermore, the affinity of the four-fold coordinated Ti atoms was dependent on the azimuthal orientation of the step edges. The steps in Fig. 4.1 on which pyridine molecules were adsorbed run parallel to the $[1\bar{1}2]$ direction. Similar activity was observed on the steps parallel to $[1\bar{1}3]$, $[1\bar{1}4]$, and $[1\bar{1}5]$ directions. Figure 4.3a shows an STM image of three pyridine molecules adsorbed on a $[1\bar{1}5]$ step, as an example. Ti-rows were well resolved on the terrace and the step-bonded molecules were again adsorbed on the intersections of the step edge and Ti-rows. In contrast, steps parallel to $[1\bar{1}1]$, $[1\bar{1}0]$, and [001] orientations were not active for the adsorption. Figure 4.3b shows a wide-area (40 x 30 nm^2) image of the pyridine-exposed surface. Step-bonded species were not observed on the steps terminating the upper terrace, which were parallel to $[1\bar{1}1]$, $[1\bar{1}0]$, and [001] directions, while short segments of $[1\bar{1}2]$ and $[1\bar{1}3]$ steps on the lower terrace were covered with eight pyridine molecules of the complete shape.

Steps capable and incapable of pyridine adsorption are modeled in Fig. 4.4, where we assume the non-reconstructed, ideal structures truncated along desired orientation. The lack of the strongly adsorbed species is not surprising on steps along the [001] and $[1\bar{1}0]$ directions. Those steps only contain five-fold and six-fold coordinated Ti atoms. In contrast, the absence of the adsorption activity on the $[1\bar{1}1]$ step is quite interesting, because four-fold coordinated Ti atoms are still exposed as shown in Fig. 4.4c. The nearest-neighbor coordination of the Ti atoms active at the $[1\bar{1}2]$ step and inactive at the $[1\bar{1}1]$ step is equivalent, four-fold. How does a pyridine molecule distinguish the step of one orientation from the other and hate the $[1\bar{1}1]$ step? Site-specific state of adsorbed benzene was found on single-atom-height steps on Cu(111) at 77 K [6]. However, preference of step-orientation was not observed in that case. The activity of the four-fold coordinated Ti center must be affected by the arrangement of atoms at 2nd nearest positions or further. A four-fold coordinated Ti atom at the inactive $[1\bar{1}1]$ step has two Ti neighbors on both sides along the step, and each of which neighbors is five-fold coordinated with oxygen atoms (Fig. 4.4c). At the active $[1\bar{1}2]$ step in Fig. 4.2, one of the neighbors is missing. The pair of the extra O atoms being coordinated to the Ti neighbor may sterically obstruct close approach of a pyridine molecule to the four-fold coordinated Ti center at the $[1\bar{1}1]$ step. The missing Ti neighbors may also perturb the electronic states of the adsorption site through the bridging O atoms. Anyway, this orientation dependent affinity is beyond the simple coordination vacancy argument.

Sequential imaging of the pyridine-exposed surface revealed that terrace-adsorbed molecules were transformed to step-bonded species and vice versa. Figure 4.5 shows sequential six frames recorded on the surface of Fig. 4.1 at an interval of 18.3 s/frame. The number and position of step-bonded pyridine molecules fluctuated through frames (a) to (f). The frame-by-frame fluctuations suggest that the residence time on a step site is comparable with the image acquisition time (order of 100 s).

The observed exchange allows us to draw a picture that the terrace-adsorbed state is a precursor to produce the step-bonded species; First, pyridine molecules in the gas phase are adsorbed on the five-fold coordinated Ti sites on terraces first. The terrace-adsorbed species migrate over the surface to be trapped at the step sites. A gas-phase pyridine molecule can also strike and adsorb directly on the step site. However, the direct adsorption should be an infrequent event due to the minor population of step sites. Thereby, surface diffusion of the terrace-adsorbed state plays an essential role to form the step-bonded species.

It has been contended that metal oxides are the place to find strong analogies with organometallic chemistry and homogeneous metal-complex catalysis [5]. The metal cations in oxides are compared to the metal centers in mononuclear metal complexes in solution in that scheme, because the cations are isolated from each other by bridging oxygen anions. However, the exchange visualized in Fig. 4.5 demonstrates that two-dimensional transport of adsorbates promotes the interactions among physically isolated metal sites. Remind that the step-direction dependent affinity is also out of the simple coordination vacancy argument of an isolated metal center. These findings lead to the chemistry characteristic of heterogeneous catalysis beyond analogies with organometallic chemistry and homogeneous catalysis. Scanning probe microscopy including STM is a powerful technique to visualize such chemical phenomena on solid surfaces of heterogeneous compositions and structures.

References

[1] H. Onishi, K. Fukui and Y. Iwasawa, Bull. Chem. Soc. Jpn. 68 (1995) 2447.

[2] S. Suzuki, Y. Yamaguchi, H. Onishi, T. Sasaki, K. Fukui and Y. Iwasawa, J. Chem. Soc. Faraday Trans. 94 (1998) 161.

[3] T. Sasaki, S. Suzuki, H. Onishi and Y. Iwasawa, to be submitted.

[4] G. Thornton, in: *Adsorption on Ordered Surfaces of Ionic Solids and Thin Films*, Springer Series in Surface Science, Vol. 33, eds. H.J. Freund and E. Umbach (Springer-Verlag, Berlin, 1993) p. 115.

[5] M. A. Barteau, Chem. Rev. 96 (1996) 1413.

[6] S.J. Stranick, M.M. Kamna, P.S. Weiss, Science 266 (1994) 99.

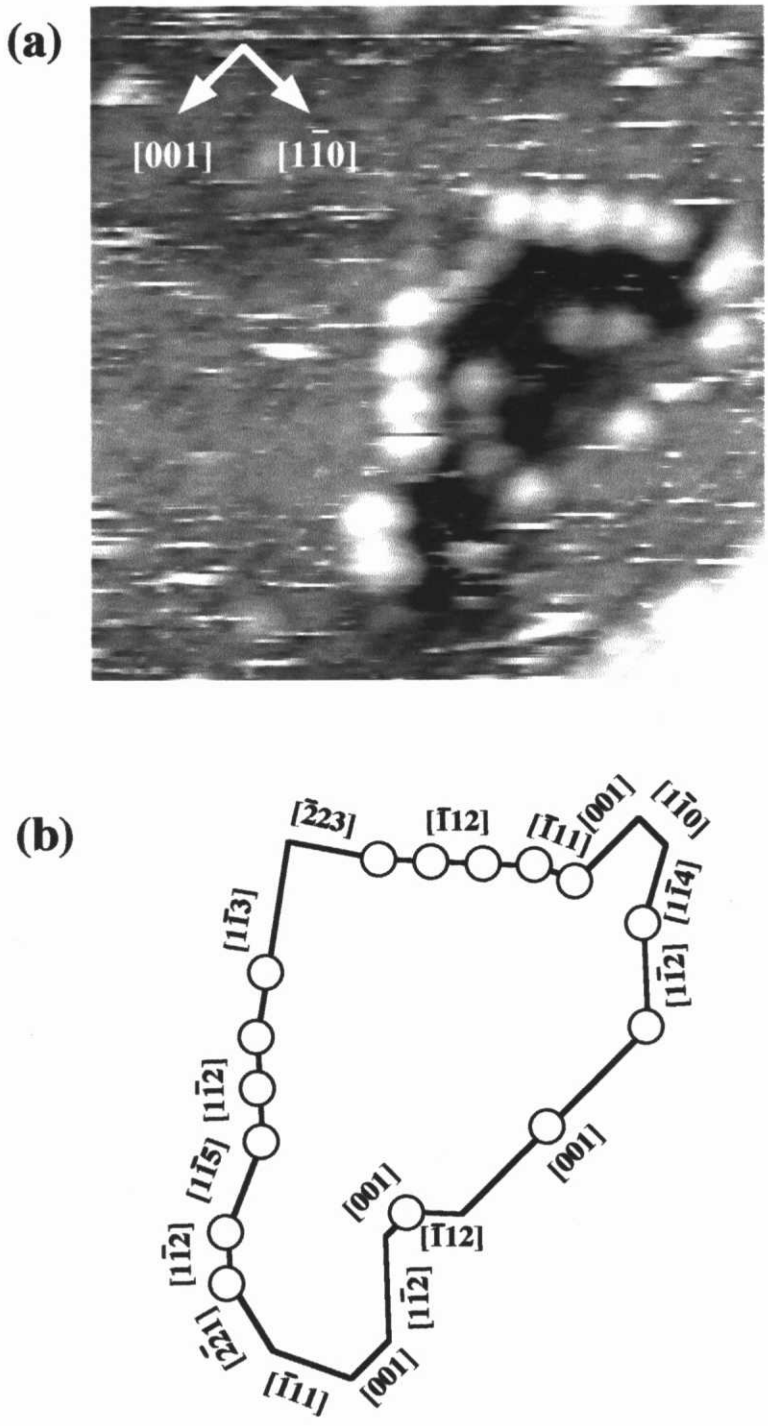

Figure 4.1. (a) An STM image of the pyridine-exposed TiO_2(110)-(1x1) surface. 15x15 nm^2, sample bias voltage: +2.5 V, tunneling current: 0.05 nA. (b) A schematic drawing of the single-atom height steps in (a). The positions of pyridine molecules adsorbed on the steps are shown by dots.

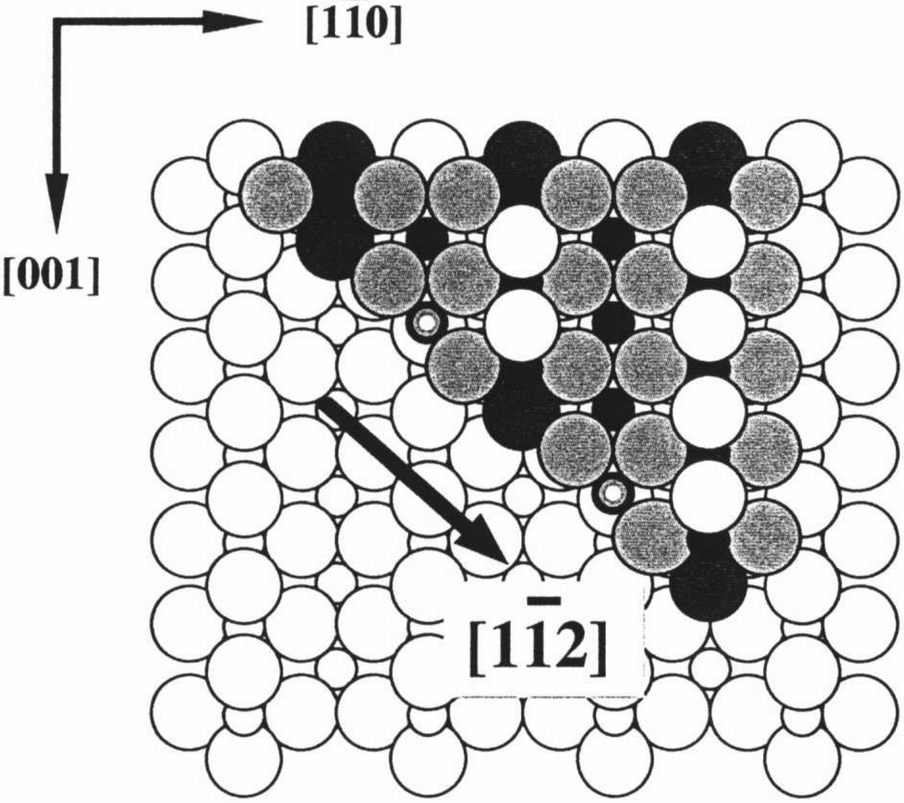

Figure 4.2. A ball model of a step along the [1$\bar{1}$2] direction. Small and large symbols represent Ti and O atoms.

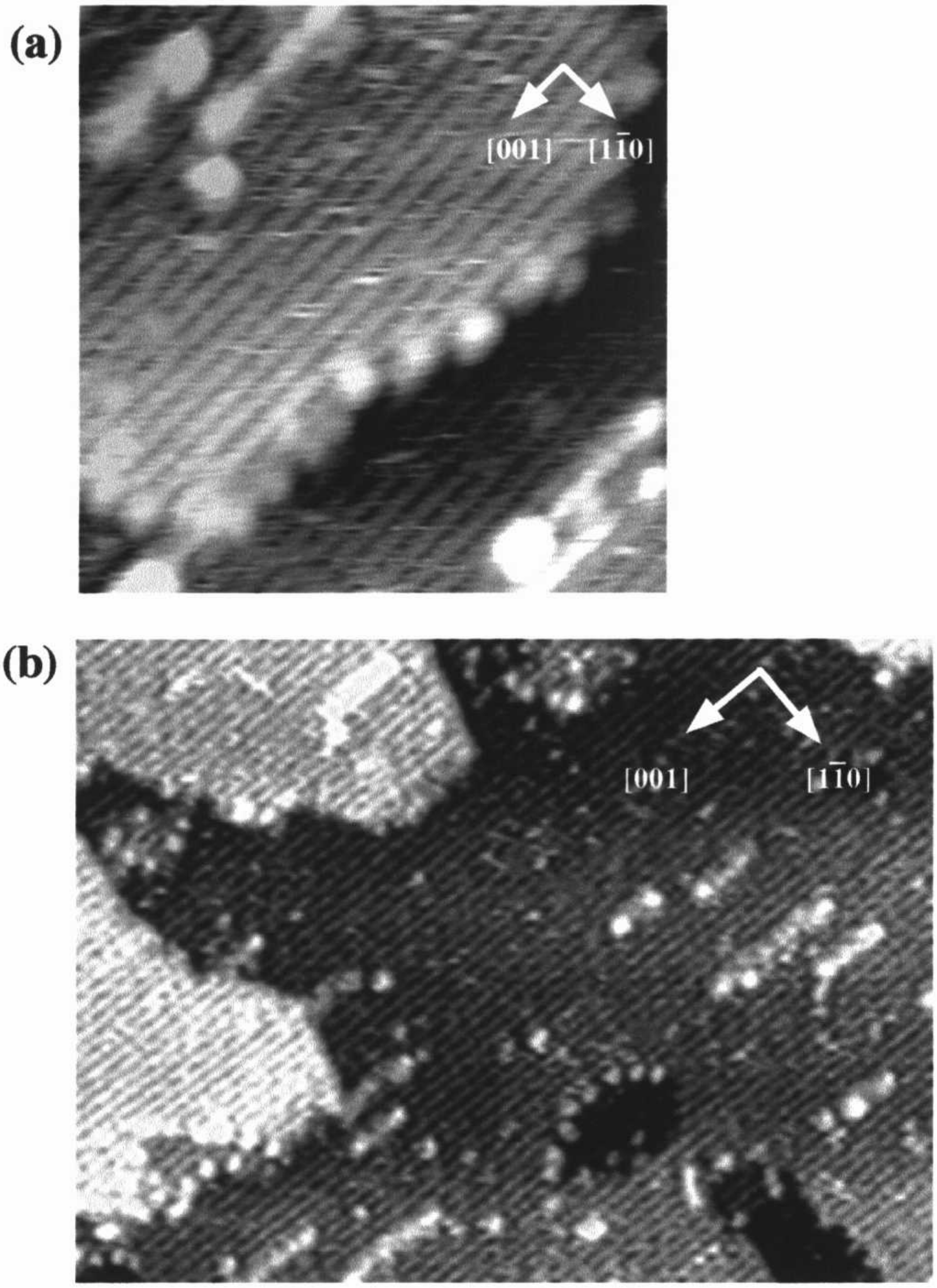

Figure 4.3 (a) An STM image of a pyridine-adsorbed step along the [1$\bar{1}$5]direction. 17x17 nm^2, sample bias voltage: +2.5 V, tunneling current: 0.05 nA. (b) A wide area image of the surface in Fig. 1. 40x30 nm^2, sample bias voltage: +2.5 V, tunneling current: 0.05 nA.

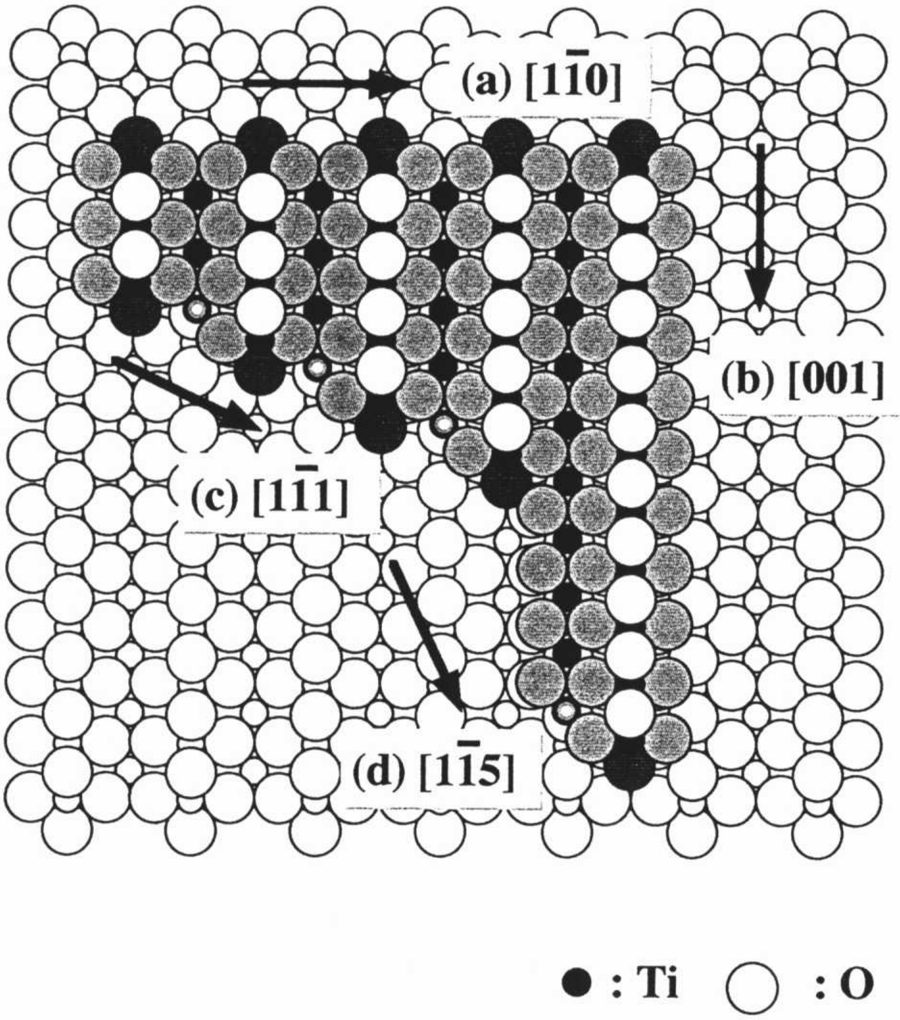

Figure 4.4. Bulk truncated models of steps along (a) [1$\bar{1}$0], (b) [001], (c) [1$\bar{1}$1], and (d) [1$\bar{1}$5] directions.

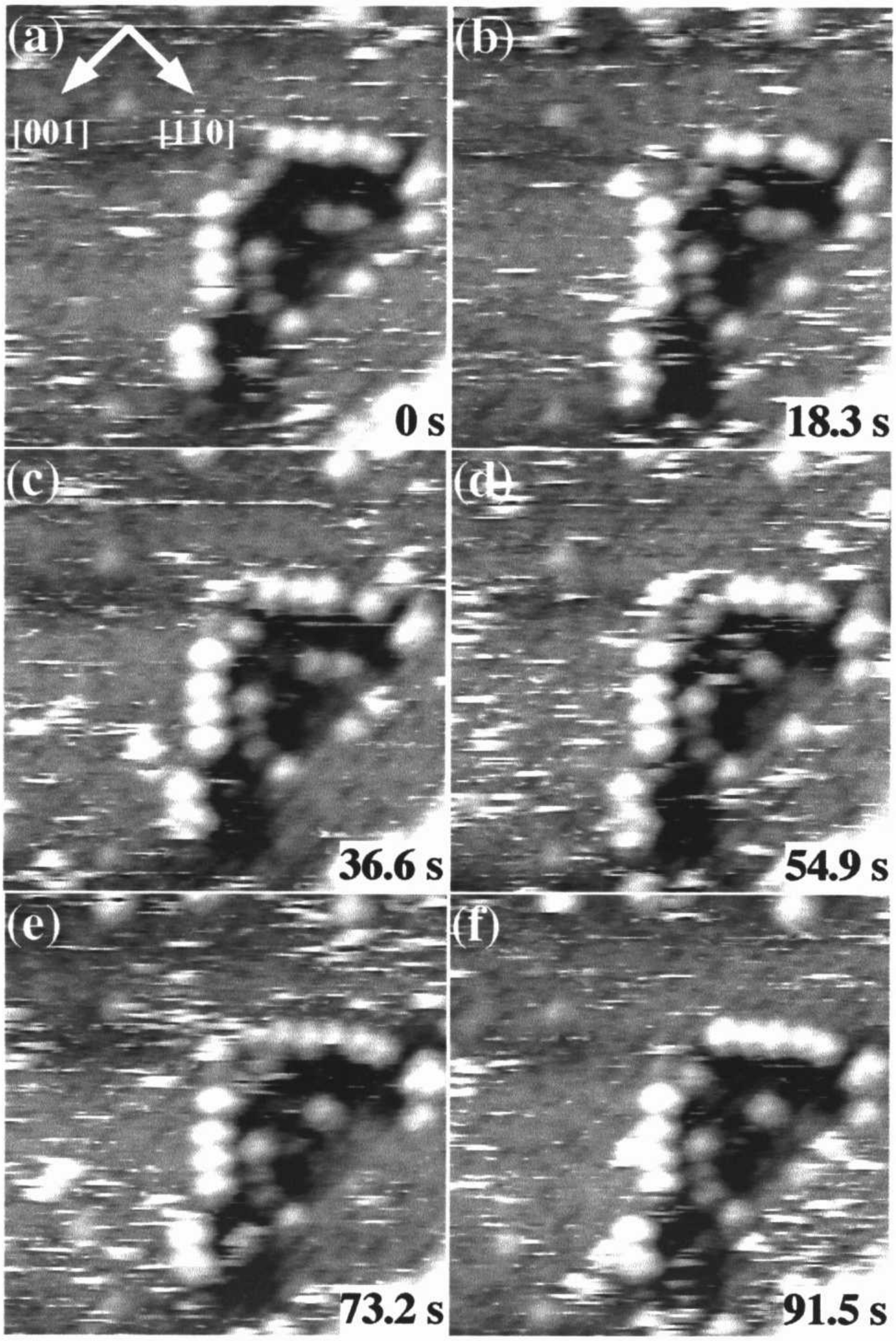

Figure 4.5. Sequential STM images of the surface shown in Fig. 4.1. The frames (a)-(f) were determined at a rate of 18.3 s/frame. 15x15 nm^2, sample bias voltage: +2.5 V, tunneling current: 0.05 nA.

Chapter 5

Identification of Individual 4-Methylpyridine Molecules Physisorbed and Chemisorbed on TiO_2(110)-(1x1) Surface by STM

Abstract

Adsorption geometries of 4-methylpyridine (4-MP) molecules adsorbed on TiO_2(110)-(1x1) have been successfully identified by sequential STM imaging. Characteristics in mobility, topographic height, and location allowed us to distinguish three adsorption states at room temperature; a chemisorbed state with the upright geometry (A_1), a flat-lying state localized at specific sites (A_2), and a flat-lying physisorbed state mobile over the surface (B). The concentration of A_1 and A_2 species was restricted at an order of 0.01 ML. A_2 state was related to the adsorption at oxygen vacancies resident on the vacuum annealed surface. The present study demonstrates the promising ability of STM to identify the adsorption geometry of small probe molecule, 4-methylpyridine in the present case, and to provide atom-level information on the origin of acidic property of oxide surfaces.

5.1 Introduction

By analyzing the adsorbed probe molecules with spectroscopic techniques such as TPD, and IR [1-4], we can evaluate the strength, quantity, and character (Lewis type or Brønsted type) of acid sites on catalysts. However, it is still difficult to identify which molecules interact with specific surface sites and to classify the way of interaction such as chemical interaction from these measurements.

STM has a great potential to overcome the problems, since individual events at each surface site should be discriminated by this method, as shown in Chapters 3 and 4. Sequential imaging of the pyridine-exposed $TiO_2(110)$-(1x1) surface (Fig. 5.1) revealed that terrace-adsorbed molecules were diffusing quickly, and transformed to step-bonded species and vice versa even at room temperature. However, the adsorption geometry of pyridine (Fig. 5.2) could not be identified by the STM observations, probably because the topographic height difference between upright and flat-lying geometries is small for this compound. In the present study, we employed 4-methylpyridine (4-MP) instead of pyridine as probe. One methyl group substituted at the *para*-position of the six-membered ring should enhance the topographic difference between the two states. This study presents that three states of 4-MP adsorbed on the (110) terrace with oxygen vacancies were identified by combining the mobility analysis and height analysis of sequential STM images.

5.2 Experimental

The experiments were performed with an UHV compatible scanning tunneling microscope (JSTM-4500VT, JEOL) equipped with an Ar^+ gun and LEED-AES optics. A polished rutile $TiO_2(110)$ wafer of 6.5 x 1 x 0.25 mm^3 (Earth Chemicals) was annealed in air at

1100 K for 1 h. Nickel film was deposited in a separate chamber on the back side of the wafer for resistive heating on the microscope stage. The temperature of the surface was monitored with an IR radiation thermometer. After cycles of Ar+ sputtering (3 keV, 0.3 μA) and vacuum annealing at 900 K, the surface showed a sharp (1x1) LEED pattern. The (1x1) surface cooled to room temperature was exposed to 4-methylpyridine (research grade, Wako Pure Chemicals) vapor in the treatment chamber and then transferred on the microscope stage without breaking vacuum. Constant current topography of the 4-MP-exposed surface was continuously observed at room temperature in UHV (~2 x 10^{-8} Pa) with an electro-chemically etched W tip and recorded in video. A positive sample bias voltage (V_s) of +2.0 V and a tunneling current (I_t) of 0.05 nA were employed in imaging.

5.3 Results and Discussion

The annealed TiO_2(110)-(1x1) surface was exposed to 0.03 L of 4-methylpyridine (4-MP) vapor at room temperature and then transferred on the microscope stage. Figures 5.3a, b, and c show STM images sequentially recorded on the 4-MP-exposed surface. Adparticles of completely circular shape and incomplete, fragmented shapes were observed on the terrace. Those features were assigned to 4-MP molecules adsorbed, since they were not observed before the exposure. Three classes of molecules could be identified based on their mobility, topographic height, and location.

By animating a number of sequential images, the mobility of admolecules could be easily differentiated. Molecules labeled A_1 in Fig. 5.3(a), the least mobile state, stayed over 15 minutes at their original positions during the course of imaging, a part of which is presented in Fig. 5.3. Those immobile 4-MP molecules exhibited the complete circular topography, since they were fixed in the time scale of tip scanning. A less stable state A_2 also seemed immobile at first sight. In image (a) there are four A_2 molecules. Three of these (except for the bottom left one) were half imaged in at least one of the sequential images recorded within 40 s, showing their diffusion on the surface. However, admolecules were again imaged at the same positions in the subsequent images. This indicates that A_2-state 4-MP molecules were trapped and liberated repeatedly at specific sites. The last class, B state, contained molecules of nearly circular topographies labeled and of unlabeled fragmented images, as shown in Fig. 5.3. They were quite mobile and easily differentiated from A_1 and A_2 species by animating sequential images. If we assume that a fragmented image corresponds to one 4-MP molecule, the concentration of B species was much larger than the population of two other states.

The difference in topographic height supported the identification of A_1, A_2, and B states. Figure 5.4 summarizes the results of cross section curves of molecules in the three states. Topography of pyridine adsorbed on this surface is also presented. A_1 state gave rise to the largest protrusion of 0.34 ± 0.02 nm (averaged on 10 molecules), while the height of A_2 state was 0.26 ± 0.02 nm (averaged on 11 molecules). A_1- and A_2-state molecules could be safely distinguished on the topographic heights. Corrugation of species B, 0.25 ± 0.02 nm (averaged on 29 molecules), was compatible with the corrugation of A_2 state. The in-plain width of A_2 species was larger than those of A_1 and B states.

The adsorbed position relative to the Ti-row was also different for A_1 and A_2. A_1-state molecules were always adsorbed just on the Ti-rows, whereas the image center of species A_2 was shifted away from the Ti-row, as illustrated in Fig. 5.3(b) where the position of the Ti-rows was marked with white lines for clarity. The location of B species was sometimes difficult to be determined precisely, because they gave often only fragmented image due to quick migration. When a B-state molecule stayed long enough for proper imaging, its topography was centered on a Ti-row.

Three different adsorption states of 4-MP were thereby distinguished with the characteristics in mobility, topographic height, and location. Here we consider the identity of those states. The most mobile state B is assigned to a physisorbed state. Molecular topography of similar mobility and height was observed on the pyridine-exposed $TiO_2(110)$ surface and assigned to pyridine molecules physisorbed in flat-lying geometry, on the basis of thermal desorption, XPS and molecular dynamics calculation results, as is described in Chapter 3.

The less mobile A_1 and A_2 species should be bound to the surface more strongly with higher barrier against migration. If we assume that image height determined in Fig. 5.4 reproduces the physical topography of the imaged molecule, the height difference of 0.08 nm can be attributed to the difference in adsorption geometry, upright or flat-lying. The height of A_2 species compatible with the corrugation of B state suggests a flat-lying geometry of A_2-state molecules. A_1 state of largest corrugation is assigned to the 4-MP molecule adsorbed with the aromatic ring vertical to the surface. Figure 5.5 illustrates the proposed geometries. One would expect that the height difference between molecules with the aromatic ring parallel and vertical to the surface would be greater than 0.08 nm. For instance, the van der Waals height of toluene is estimated to be 0.8 nm, while its thickness is 0.4 nm. Our simple assumption is supported by a systematic observation of the image height of formate, acetate, and pivarate (trimethylacetate) ions adsorbed on the $TiO_2(110)$ surface. The image height of the carboxylate ions were 0.15 nm, 0.25 nm, and 0.45 nm, respectively [5]. Because those carboxylates should be adsorbed in bridge form, the increase in image height is related with the size of the alkyl group. By substituting a hydrogen atom with a methyl group, image height increased by 0.10 nm from formate to acetate, and by 0.20 nm from acetate to pivalate. One methyl group, the van der Waals radius of which is 0.2 nm, induced much smaller increase in image height. This is well known as an artifact of 'tunnel vision' resulting from the dominant contribution of electronic effects in tunneling.

The upright geometry A_1 naturally leads to a chemisorbed state with a definite N-Ti bond. The concentration of this state was not more than 0.01 ML. The restricted population is reasoned if we assume that the formation of this chemisorbed state is an activated process with a small sticking coefficient at room temperature.

A flat-lying geometry of A_2 state was suggested by the height analysis. On the other hand, A_2 species were much less mobile than the B-state physisorbed molecules. As mentioned above, detailed inspection of the sequential STM images revealed that the A_2-state molecules trapped and liberated repeatedly at specific sites. These experimental results can be interpreted by assuming that A_2 species are adsorbed at oxygen vacancies in a flat-lying geometry. Actually, an empirical molecular dynamics calculation predicted a flat-lying state of pyridine is more strongly bound at a point vacancy of bridge oxygen than on the perfect terrace by 8 kJ/mol. Oxygen vacancies are easily created on vacuum annealed $TiO_2(110)$ surfaces [6], and recently visualized by atomic force microscopy operated in a frequency modulated non-contact mode (NC-AFM) [7]. The number density of the vacancies observed with NC-AFM was 0.02 ML, which is comparable to the coverage of A_1-state molecules obtained in the present study.

The mobile physisorbed state was majority species of 4-MP and pyridine on the $TiO_2(110)$-(1x1) surface. This verifies that the five-fold coordinated Ti^{4+} ion exposed to the surface is incapable of forming stable N-Ti bonds with the basic nitrogen atoms of those compounds. The reason for the weak Lewis-acid property of the Ti centers was not cleared from this study. For more detail discussions, it probably required comparative study of other base molecules. In summary, three different states of 4-methylpyridine adsorbed on the $TiO_2(110)$-(1x1) surface were distinguished with the characteristics in mobility, topographic height, and location, which were determined by analysis of sequential STM topographies; a chemisorbed state with the upright geometry (A_1), a flat-lying state localized at specific sites (A_2), and a flat-lying physisorbed state mobile over the surface (B). The concentration of A_1 and A_2 species was restricted at an order of 0.01 ML. A_2 state was related to the adsorption at oxygen vacancies resident on the vacuum annealed surface. The present study demonstrates the promising ability of STM to identify the adsorption geometry of small probe molecules, 4-

methylpyridine in the present case, and to provide atom-level information on the origin of acidic property of oxide surfaces.

References

[1] C. Morterra, G. Ghiotti and E. Garrone, J. Chem. Soc. Faraday I 76 (1980) 2102.

[2] M. Waqif, J. Bachelier, O. Saur and J. C. Lavalley, J. Mol. Catal. 72 (1992) 127.

[3] M. Delarco, S. R. G. Carrazan, C. Martin and V. Rives, J. Mater. Sci. 31 (1996) 1561.

[4] T. Kataoka and J. A. Dumesic, J. Catal. 112 (1988) 66.

[5] H. Onishi, K. Fukui and Y. Iwasawa, to be submitted.

[6] V. E. Henrich and P. A. Cox, *The Surface Science of Metal Oxides*, (Cambridge University Press., Cambridge, 1994).

[7] K. Fukui, H. Onishi and Y. Iwasawa, Phys. Rev. Lett. 79 (1997) 4202.

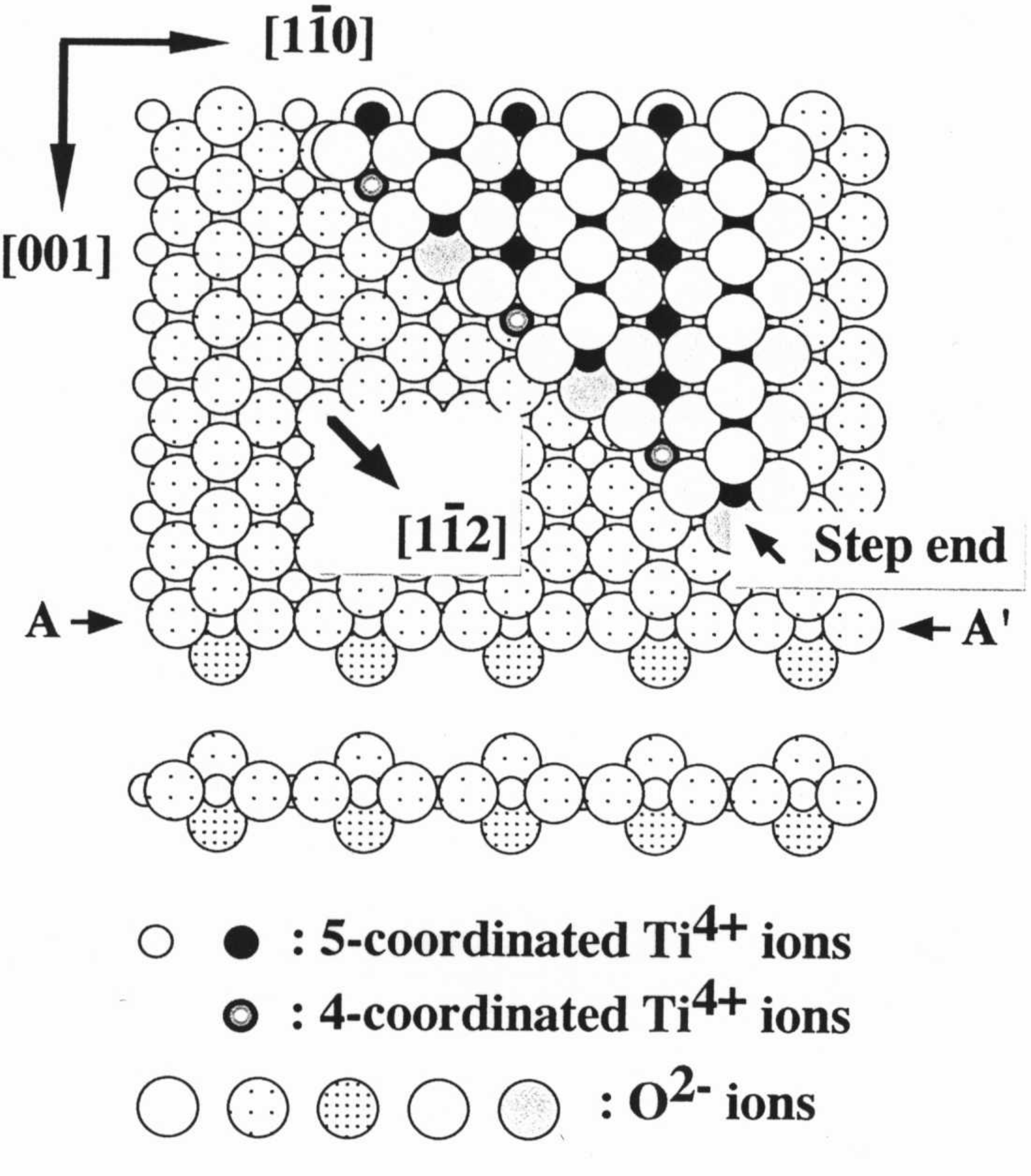

Figure 5.1. A model of TiO_2(110)-(1x1) surface with a single height step along the direction. A top view and A-A' cross section are shown

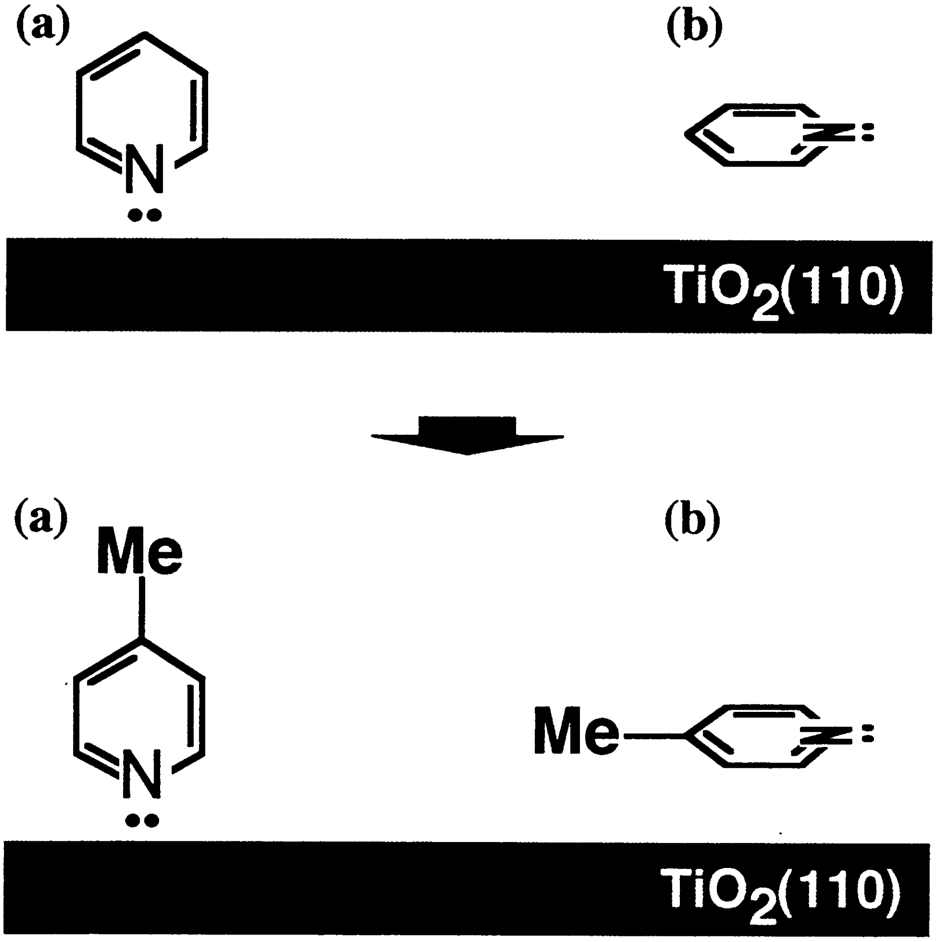

Figure 5.2. Schematic drawings of pyridine and 4-methylpyridine probe molecules in (a) a flat-lying physisorbed state, and (b) an upright chemisorbed state.

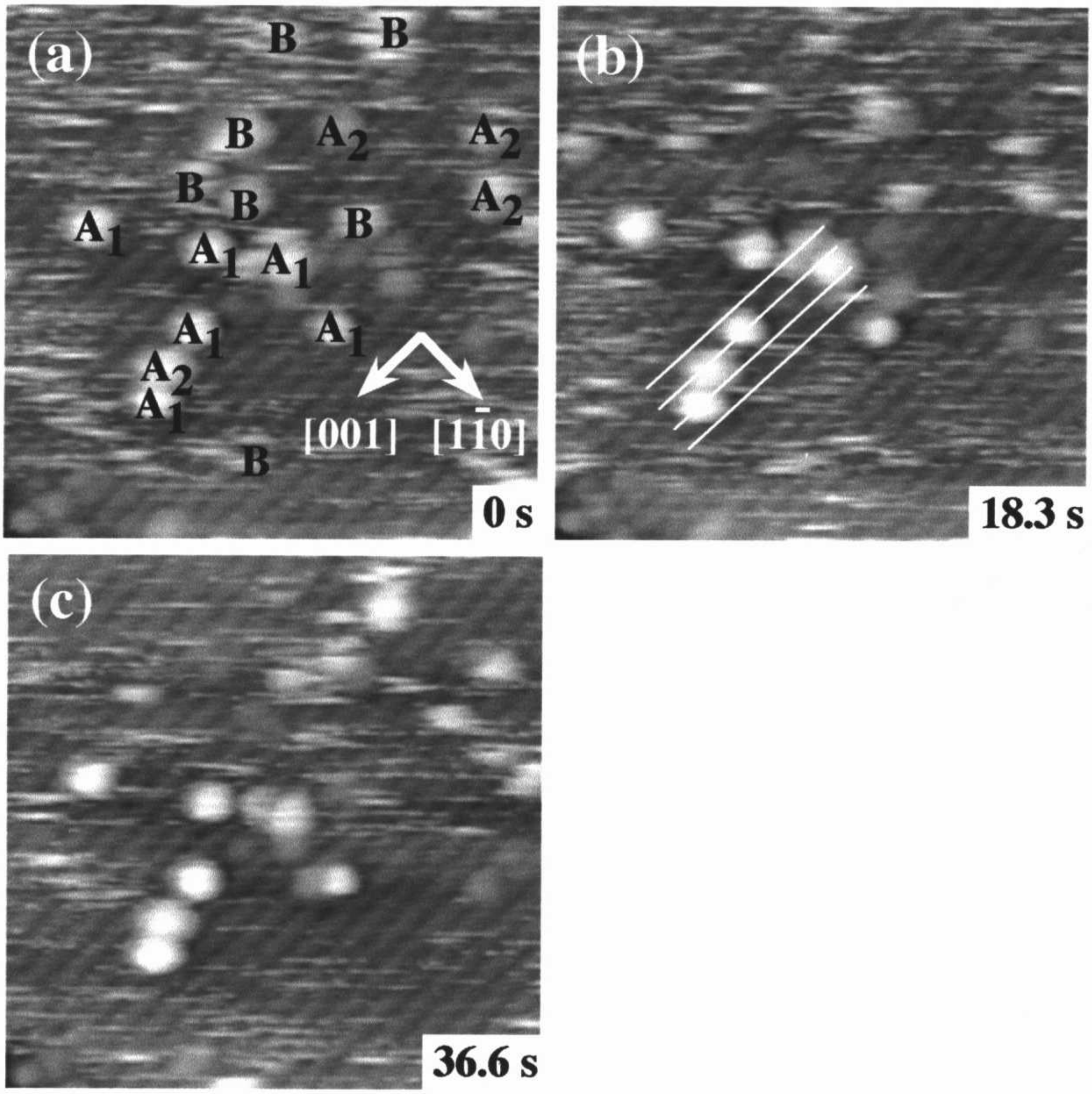

Figure 5.3. Sequential STM images of the 4-methylpyridine-exposed TiO_2(110)-(1x1) surface. 15x15 nm^2, sample bias voltage: +2.0 V, tunneling current: 0.05 nA.

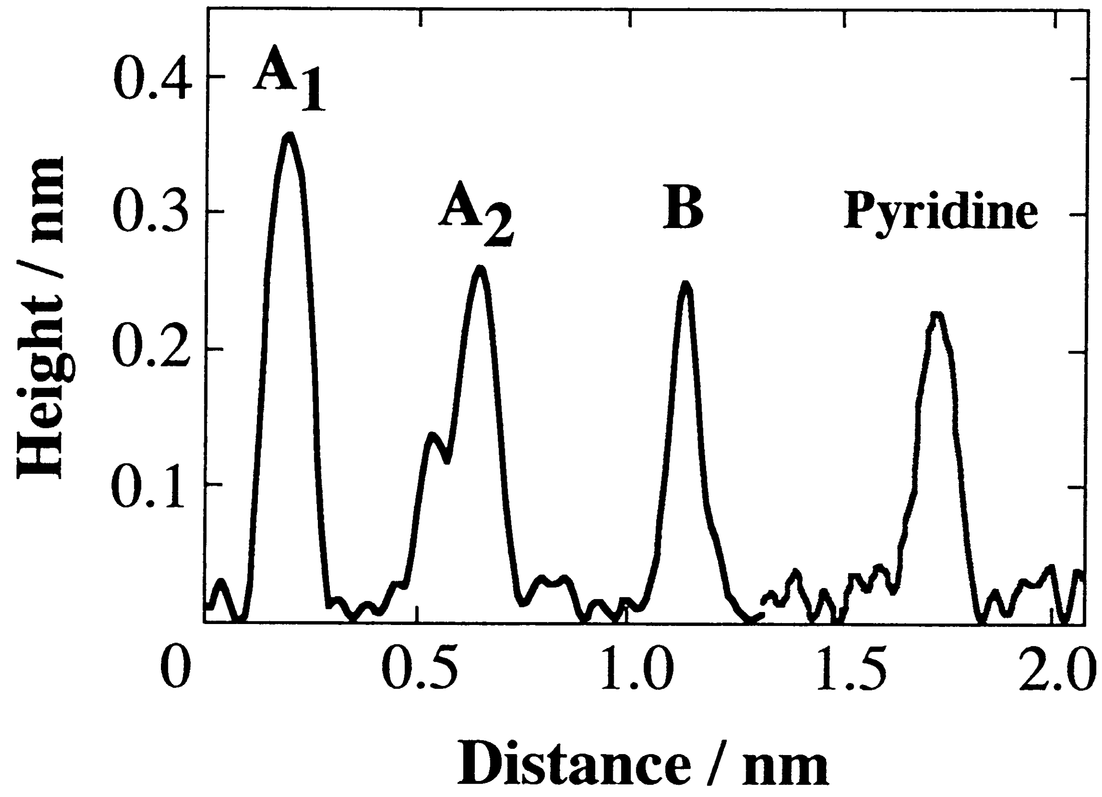

Figure 5.4. Cross sections of STM topography of different states of 4-methylpyridine molecule, and the flat-lying physisorbed state of pyridine molecule on the $TiO_2(110)$-(1x1) surface.

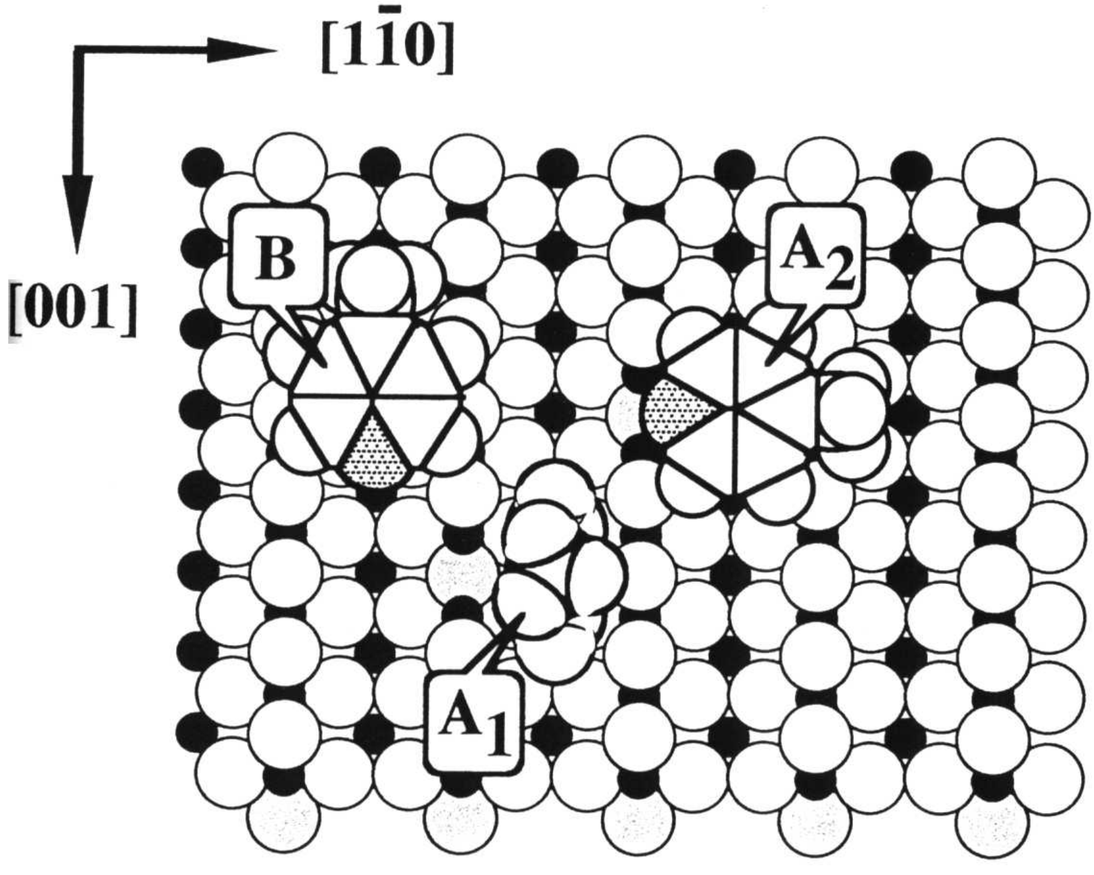

Figure 5.5. A pictorial model of A_1, A_2, and B states of 4-methylpyridine molecules adsorbed on the $TiO_2(110)$-(1x1) surface.

Chapter 6

Direct viewing of surface acidity of $TiO_2(110)$ by in situ STM Observation of Adsorbed Ammonia

Abstract

The $TiO_2(110)$-(1x1) surface after exposure to ammonia was observed by STM at room temperature. A few amounts of adparticles and many grains covered with surface was observed, and sequential STM images revealed that time-resolved behavior of the adparticles on the five-fold coordinated Ti sites. From the STM measurements, it was concluded that $TiO_2(110)$ surface was basically inactive for adsorption of ammonia. While, the adparticles was only observed in a particular area in the absence of grains that were assigned to hydrogen atoms on the bridging oxygen rows, as is mentioned in Chapter 8. Further, the adparticles on the terraces were assigned to chemisorbed or dissociative species of ammonia, but not physisorbed ammonia. Therefore, the results revealed that the five-fold coordinated Ti sites were originally active for chemisorption of ammonia and accessible way toward the Ti sites were interrupted by hydrogen atoms on the bridging oxygen rows. The nature of hydrogen atoms on bridging oxygen rows was considered as a different species from a hydroxyl having activity for adsorption through hydrogen bonding. These hydrogen atoms were inevitably to appear on the surfaces, because single crystals were grown by Bernoulli method using H_2-O_2 flame. On the other hand, the immobile step-bounded species were also observed, and activity dependence of adsorption of ammonia on the four-fold coordinated Ti sites was similarly found in the pyridine case. The adparticles on the steps was also assigned to chemisorbed or dissociative species of ammonia.

6.1 Introduction

In Chapters 3, 4, and 5, adsorption of aromatic base molecules on $TiO_2(110)$ was treated sequentially. In view of the conventional acid-base interaction, the highly ionized Ti atoms exposed to the (110) surface were expected to be Lewis acid sites favorable for pyridine chemisorption, but the facts on these molecules were against the expectation. They were physisorbed on the terrace except the case of presence of oxygen vacancies of the bridging oxygen rows surrounding the five-fold coordinated Ti sites. Figure 6.1 shows bulk terminated structural model of $TiO_2(110)$. As is mentioned in Chapter 3, why the Ti^{4+} ions on $TiO_2(110)$-(1x1) did not show Lewis acidity in spite of the presence of accessible space for chemisorption of pyridine was a quite interesting and important issue for catalytic chemistry. It was found that carboxylate anions, which are conjugate bases of the corresponding carboxylic acids, were tightly chemisorbed on the Ti atoms [1, 2].

Here, the adsorption of ammonia on $TiO_2(110)$ was observed by STM under UHV condition at room temperature. Molecular size of ammonia is smaller than the size of aromatic ring of pyridine, therefore it was expected to examine whether the Ti sites was originally inactive or active for chemisorption of base molecules. As a matter of fact, observed image of ammonia was smaller than that of pyridine. The present study showed that ammonia was able to truly interact with the Ti sites and proved the latter expectation. Furthermore, peculiar site dependence of adsorption of ammonia was also observed by in situ dynamic study of STM.

6.2 Experimental

The experiments were performed in a UHV chamber equipped with scanning tunneling microscope (JSTM-4500VT, JEOL), Ar^+ sputtering gun, and LEED-AES optics. A polished rutile $TiO_2(110)$ wafer of 6.5 x 1 x 0.25 mm^3 (Earth Chemicals) was annealed in air at 1100 K for 2 h. Nickel film was deposited on the backside of the wafer for resistive heating on the microscope stage. The temperature of the surface was monitored with an IR radiation thermometer. After cycles of Ar^+ sputtering (3 keV, 0.3 μA) and vacuum annealing at 900 K, the surface showed a sharp (1x1) LEED pattern. Ammonia (research grade, Wako Pure Chemicals) was purified by pump-through cycles. Ammonia vapor was introduced through a gas doser attached on a pretreatment chamber. After exposure of NH_3 vapor, the sample was transferred to the microscope stage loaded another chamber without breaking vacuum. Constant current topography of the NH_3-exposed surface was observed at room temperature in UHV (~2 x 10^{-8} Pa) with an electro-chemical etched W tip. A positive sample bias voltage (V_s) of +1.0 V and a tunneling current (I_t) of 0.05 nA were employed in imaging.

6.3 Results and Discussion

6.3.1 Adsorption of ammonia on the $TiO_2(110)$ surface

The $TiO_2(110)$-(1x1) surface was exposed to 3 L of NH_3 vapor at room temperature and then transferred on the microscope stage. STM observation was carried out at room temperature after 2 h later. Figure 6.2(a) to (c) indicate sequential STM images with time interval of 36.6 s. Small amount of adparticles were observed on the Ti-rows after exposure of ammonia, and most of them often diffused at random direction or moved along the Ti rows. For example, an arrow pointed the adparticle in Fig. 6.2(a). An average topography of the adparticle was 0.09±0.02 nm in height measured from the Ti-rows of $TiO_2(110)$. Nevertheless the exposure of 3 L was expected to be enough to create a surface covered with a certain amount of adsorbate, the surface coverage was in the range from ca. 0.03 to 0.08 ML. In fact, while pyridine was physisorbed on the surface, the 3L exposure was enough to be reached to the coverage of 0.3 ML in the case of pyridine, as is described in the Chapter 3. Therefore, it was concluded that the TiO_2(110)-(1x1) surface were basically inactive for adsorption of ammonia.

In addition to the adparticles, many grains were simultaneously observed between the Ti rows, i.e. on the oxygen rows. The grains were also observed the sputtered-annealed surface. In this study, appearance of the grains was inevitable when the TiO_2(110) surface were observed by STM. Once, the grains had been ascribed to intrinsic oxygen vacancies of the bridging oxygen rows. However, the grains, which are represented as "bright spots" in Chapter 8, have been assigned to hydrogen atoms on the bridging oxygen rows, in other words, hydroxyl-like species in the chemical formula by certain experimental proofs. The source of hydrogen was ascribed to the dissolved hydrogen atoms that were possibly stored during the crystallization of TiO_2 single crystal by Bernoulli method where TiO_2 melted and crystallized in H_2-O_2 flame.

The corrugation profiles of STM do not in themselves solve an issue of interpretation of all the STM images, and the amount of adparticles were too small to analyze by macroscopic techniques such as XPS, UPS, and thermal desorption. However, they may be assigned as the chemisorbed ammonia, or dissociative ammonia on the five-fold coordinated Ti sites. Physisorbed ammonia was not a candidate, because molecular dynamics simulation on the physisorption of ammonia over a perfect (110) terrace did not reproduce the stable adsorption state at room temperature as was observed by STM. Comparing with the study of pyridine in Chapter 3, calculated adsorption energies of ammonia and pyridine were 55 kJ/mol and 84 kJ/mol, respectively. That indicated desorption kinetic constant of ammonia was at least the order of 10^5 times larger than that of pyridine at room temperature. In the above case, this idea did not contradict the above assignation. Therefore ammonia could contact with the five-fold coordinated Ti site in a groove between bridging oxygen rows. That is the different point of adsorption of aromatic base molecules in Chapters 3, 4, and 5, which described that the oxygen vacancies were prerequisite for chemisorption of these base molecules.

What make the five-fold coordinated Ti sites inactive for acid-base interaction was considered as follows. It was expected that ammonia molecules would stay for a long time at favorable sites, while they were not stayed or observed at non-favorable sites. Therefore, sequential STM images provided detail information about the diffusion of the adparticles, and the behavior of adparticles reflected their affinity to adsorption sites.

Figures 6.3(a) to (f) and Figures 6.4(a) to (h) show two series of sequential STM images recorded with time intervals of 18.3 s. The two series were originated from the same series of STM images. There was no grains existed in a circular area represented in Fig. 6.3(a) with radius of 2.3 nm from the center of the adparticle, and the adparticle crossed over the bridging oxygen row and diffused along the Ti row. In contrast, at least 5 grains included in the same area surrounding the adparticle in Fig. 6.4, and the adparticle hardly relocated its position from (a) to (h). It seemed that condensed three or four grains prevented the diffusion of the adparticle along the Ti row in Fig. 6.4. Hence, the difference in the behavior of those adparticles was due to their surroundings, i.e. the grains had an effect on the diffusion of adparticles.

For more examples, adparticles was hardly observed in the stable form at the five-fold coordinated Ti site adjacent to an isolated grain, as show in Figs. 6.5(a) to (h). Twenty and eleven frames were omitted between Figs. 6.5(a) to (b) and Figs. 6.5(g) to (h) with time interval of 366.0 s and 201.3 s, respectively. Figs. 6.5(b) to (g) show sequential STM images with time interval of 18.3 s. These STM images revealed step-bounded adparticles on the upper-side and left side in the images, but note that an adparticle pointed by an arrow in Fig. 6.5(a) bounded on a side of the small terrace. The adparticle did not migrate during recording images from Figs. 6.5(a) to (b). However, the adparticle suddenly jumped into the inside of the terrace crossing over the three or four bridging oxygen rows until next frame was recorded, i.e. Figs. 6.5(c) to (f). Again, the adparticle was instantly moved to the other side of the terrace edge and stayed there to the end of observation. There was the dense area of the grains inside of the terrace, while little grains were observed in the region near the steps where the adparticles stayed in the stable manner. Thus the results showed that there was hardly-adsorbed area for the adparticles. Another example was shown in Figs. 6.6(a) to (f). Figure 6.6(a) shows an initial position of adparticles pointed by an arrow. While the adparticle diffused along the [001] direction from Figs. 6.6(a) to (c), the circular shape of the adparticle suddenly changed into fragmented one over the dense region of the grains in Fig. 6.6(d). Four fragmented shapes in the image indicated footprints of the adparticle during scanning tip in that region. In Figure 6.6(e), the adparticle were again properly imaged, and adsorbed near the step site pointed by an arrow in Fig. 6.6(f). In similar to the pyridine case, the fragmented shape was interpreted that the adsorbed state of the adparticle diffused too rapid to observed as the properly image, and that indicated the weakly adsorption state of the adparticle. Thus the grains on the bridging oxygen rows restricted adsorbed area for the adparticles.

The dimensions of hardly-adsorbed area were estimated. The observed shortest length between the adparticle and the grains along the [001] and $[1\bar{1}0]$ directions was estimated ca. 0.65±0.04 nm, ca. 1.02±0.04 nm, respectively. These two lengths correspond to nearly 2 times (0.592 nm) and nearly 1.5 times (0.974 nm) periodicity of surface unit cell, as is drawn in Fig. 6.7, where two adparticles and two grains were adsorbed on a bulk terminated surface model. In this model, two adparticles were located at the nearest position to each grain, and the shortest distance between them was 0.675 nm. Hence, the hardly-adsorbed area were estimated as an internal area of a circle centered at the grain with a radius of 0.675 nm including six five-fold coordinated Ti sites surrounding the single hydrogen atom, as show in Fig, 6.7.

The above interpretation supposed that only 0.17 ML of the isolated hydrogen atoms made all the five-fold coordinated Ti sites inactive for adsorption of ammonia on the surface at room temperature; the hydrogen atoms on the bridging oxygen rows controlled the surface Lewis acidity of $TiO_2(110)$. In this experiment, the coverage of the hydrogen atoms was locally uneven on the terrace, but was estimated to 0.14 to 0.18 ML with an exception of the region near the steps. Further, an averaged coverage of the hydrogen atoms on the whole surface was also estimated to 0.15 ML. The coverage of 0.15 ML indicated that the 0.10 ML of the Ti sites remained on the surface as the active Lewis acid sites for the adsorption of ammonia. In spite of roughly estimation, this value was in almost agreement with the coverage of adparticles observed by STM.

In general, creation of a certain amount of oxygen vacancies (ca. 1-10%) on a metal oxide surface is inevitable under UHV condition. Therefore, it might be considered that the difference behavior of adparticle was due to the strength of interaction with oxygen vacancies on the bridging oxygen rows, as was similar to the case of pyridine. However, this idea can not explain why the adparticle was diffused along the Ti rows. Basically, it was hard to consider that the surface structure was retained the original structural stability when a series of oxygen vacancies were created on the bridging oxygen row. Further, it does not explain the main purpose of this issue why the $TiO_2(110)$-(1x1) surface were basically inactive for adsorption of ammonia, where surface exposed Ti sites were arranged along the [001] direction with an accessible free space between the protruding bridging oxygen rows.

By the way, the nature of hydroxyls including Brϕnsted acid sites was commonly accepted to promote the adsorption of electron rich compounds on the surface through making hydrogen bonding at first. The hydrogen atoms on the bridging oxygen rows, however, did not adsorb preferentially ammonia molecules, in addition to having a loss effect of activity control of the five-fold coordinated Ti sites. Therefore, the nature of hydrogen atoms on the adsorption of ammonia was seemed to be different from the same category of conventional hydroxyls in spite of similar chemical formula. Nevertheless, the existence of such inactive hydroxyls was also reported about adsorption of methanol, ethanol, and water on Cr_2O_3 powder [3, 4]. The authors presented that the coexisting three types of hydroxyls including active for physisorption/chemisorption and completely inactive one could be divided by FT-IR spectroscopy. Division of hydroxyls was also traditionally reported in 1965 [5-7], revealed that the character of hydroxyl on alumina surface was classified into five types by the number of nearest neighbors of lattice oxygen a hydroxyl. The most relatively negative hydroxyl had four oxygen ion nearest neighbors; the most positive one was immediately situated adjacent to vacant sites, although the actual net charge of these hydroxyls was unknown. Therefore, the absence of affinity of the hydroxyl-like species to the adsorption of ammonia could be explained due to higher local charge density than expected; the defect free environment of the hydroxyl-like species on the $TiO_2(110)$ surface corresponded to dense, close packed environment of the relatively negative charged or relatively neutral hydroxyls on alumina surface. Therefore, assuming the hydroxyl-like species being not positively charged to have the affinity, both of the issues: the loss effect of activity of the five-fold coordinated Ti sites and less affinity to adsorption of ammonia was satisfactory explained by that. Driving force of these effects was interpreted as the repulsive force between the base molecules and the hydrogen atoms on the bridging oxygen rows.

As far as the loss effect of hydrogen atoms on the activity of the five-fold coordinated Ti sites is concerned, it may requires more supports of experimental data. A study of temperature desorption of ammonia on $TiO_2(110)$ with various concentration of hydrogen atoms, which can be controlled by low-energy electron exposure and exposure of hydrogen atoms to the surface as described in Chapter 8, can provide a more direct experimental proof of the effect and more precise discussions. In this occasion, there were the experimental results reported by some researchers that might be regarded as a proof of the loss effect of the hydroxyl-like species on the active sites. In a study of IR spectroscopy of TiO_2 powder, the characteristic adsorption peaks of pyridine adsorbed on Lewis acid sites decreased after exposure to water vapor [8]. Although the authors proposed that some of the adsorbed pyridine be displaced with water, the effect of water was seemed to be similar to the loss effect on the Lewis acidity in this study, because it was expected that creation of such hydroxyl-like species on TiO_2 by water dissociation examined by some researchers [9-11].

6.3.2 STM observation of steps after exposure to ammonia

STM observation simultaneously revealed surface another species bounded at the step-sites. In Figs. 6.5, 6.6, and 6.8, every image showed tightly bounded particles at the steps. In the study of pyridine, the step-bounded pyridine sometimes disappeared and reappeared during observation. That was interpreted due to collision between surface diffusing physisorbed pyridine and step-bounded pyridine. In Chapter 4, it was concluded that those two species were similar and exchangeable one with the same compounds with chemical formula, C_6H_5N. Nevertheless, in this case, the step-bounded species were not perturbed by terrace diffused adparticles during continuous STM observation, as is clearly seen in Fig.6.8. Moreover, topographic feature of the step-bounded particles was not the same as the terrace adsorbed ammonia species. While the height of adparticles on the terrace were 0.09±0.02 nm, the height of step-bounded particles was 0.05±0.02 nm. Besides, location of step-bounded species was slightly slipped off over the five-fold coordinated Ti^{4+} sites along the $[1\bar{1}0]$ direction, as show in Figs. 6.9(a) and (b). Figure 6.9(b) is the same image of Fig. 6.9(a) with adding the lines corresponding to the Ti rows, where the image center of the step-bounded particles was not on the Ti-rows, but on the middle position between Ti rows and O rows. Hence, the step-bounded species were seemed to be different from the terrace-adsorbed species. Figure 6.9(c) shows a bulk terminated structural model of a step along the $[1\bar{1}2]$ direction with circular mark representing the observed positions of step-bounded species. The circle lines include the four-fold coordinated Ti sites where ammonia can be molecularly or dissociatively adsorbed in view of the acid-base interaction in similar to the five-fold coordinated Ti sites. Thus one can imagine there were two candidates for the step-bounded species, while it was difficult to identify the chemical state by own STM image from this data. First was a molecularly adsorbed NH_3 with slanting toward the lower terrace, since the topographic height of the step-bounded species lower than that of terrace-adsorbed species. Indeed, slanting adsorption geometry on the $[1\bar{1}2]$ step was expected, because the step was geometrically identical to the micro terrace of (157) plane in view of the crystallography. Second was the dissociative species of ammonia, NH_x (X=1,2) with forming O_s-H species, as was similar to water dissociation [11], though no other species were found on the bridging oxygen adjacent to the step-bounded species during STM observation.

The activity of the four-fold coordinated Ti sites were also depended on the direction of steps in azimuth in similar to the pyridine case. Figure 6.10 shows a typical STM image of inactive step sites for adsorption of ammonia. While a few terrace-bounded species near the steps and fragmented shapes of terrace adsorbed species were imaged, the step-bounded species was not observed on the steps along the $[1\bar{1}1]$ direction. Although a nitrogen atom of ammonia can interact chemically with even the five-fold coordinated Ti sites between protruding bridging oxygen rows on the terrace, the four-fold coordinated Ti sties along the $[1\bar{1}1]$ direction was not active for adsorption of ammonia. Therefore the inactivity was not caused of the loss effect of hydrogen atoms, and the activity dependence of adsorption was interpreted in similar way as is mentioned in Chapter 4. The activity of the four-fold coordinated Ti sites must be affected by the arrangement of atoms of second nearest neighbor or further. The results of ammonia also indicated that the activity dependence was not related to the steric hindrance of the neighbor atoms surrounding the Ti sites, since the effective molecular size of ammonia was much smaller than that of aromatic ring of pyridine without consideration of molecular orientation. Although the theoretical calculations must be needed, the difference of electronic states between the two types of step sites was expected as a possible candidate for explanation of activity dependence.

6.4 Conclusions

Throughout this work, it was concluded that $TiO_2(110)$ surface was basically inactive for adsorption of ammonia, and the cause of less active for adsorption was discussed. From the sequential STM measurements, it was found that adparticles originated from ammonia were able to adsorb in the areas where hydrogen atoms on the bridging oxygen rows were absence. The effective area of a hydrogen atom was estimated to be reached six Ti sites on the terrace. On the other hand, the immobile step-bounded species and their activity dependence of adsorption on the four-fold coordinated Ti sites were similarly found in the pyridine case. While the corrugation profiles of adparticles did not in themselves solve an issue of interpretation of their composition, both of the adparticles on the terrace and the step was thought as chemisorbed or dissociative species of ammonia, but not physisorbed ammonia. Accordingly, it was concluded that ammonia molecules adsorbed as Lewis base molecules on the five-fold coordinated Ti sites on the terrace, but their activity was strongly restricted by adsorbed hydrogen atoms on the bridging oxygen rows. Besides, although the activity dependence of the four-fold coordinated Ti sites could not be precisely understood from this study, the results revealed the activity dependence was not related to steric effect due to molecular size.

The present study revealed apparently the same results of pyridine and 4-methylpyridine that the molecules did not preferentially chemisorbed, and a few molecules chemically interacted with specific sites. However, this issue involved a difference topic in the chemisorption sites. Ammonia could interact chemically with all of the five-fold coordinated Ti sites in a particular area where hydrogen atoms on the bridging oxygen rows were absence, whereas 4-methylpyridine chemically interacted only at the surface specific sites of Ti atoms, perhaps near the oxygen vacancies of the bridging oxygen, see Chapter 5. Therefore, understanding the cause of inactivity in the ammonia case could provide a suggestion for the interpretation of the inactivity of the Ti sites in the pyridine case. From the present study, it was found that the five-fold coordinated Ti sites on $TiO_2(110)$ was originally active for chemisorption of base molecules, but other effects were decisive factor of the effective Lewis acidity. Other effects were expected as follows, steric hindrance due to molecular size, hydrogen atoms on the bridging oxygen rows, and negative charge from the bridging oxygen. As is discussed in Chapter 3, the first candidate was hardly to consider, because there was actually the room to access for the base molecules into the five-fold coordinated Ti sites in the groove of oxygen rows. The second candidate could not be applied for the pyridine case since from the above reason. Hence, the third candidate was applicable to interpret as the reason why pyridine did not chemisorb at the five-fold coordinated Ti sties on $TiO_2(110)$.

References

[1] H. Onishi and Y. Iwasawa, Langmuir 10 (1994) 4414.

[2] H. Onishi and Y. Iwasawa, Chem. Phys. Lett. 226 (1994) 111.

[3] S. Kittaka, T. Sasaki, N. Fukuhara and H. Kato, Surf. Sci. 255 (1993) 282.

[4] S. Kittaka, T. Umezu, H. Ogawa, H. Maegawa and T. Takenaka, Langmuir 14 (1998) 832.

[5] J. B. Peri, J. Phys. Chem. 69 (1965) 231.

[6] J. B. Peri, J. Phys. Chem. 70 (1965) 2937.

[7] J. B. Peri, J. Phys. Chem. 69 (1965) 220.

[8] T. Kataoka and J. A. Dumesic, J. Catal. 112 (1988) 66.

[9] L. Q. Wang, A. N. Shultz, D. R. Baer and M. H. Engelhard, J. Vac. Sci. Technol. 14 (1996) 1532.

[10] M. A. Henderson, Surf. Sci. 355 (1996) 151.

[11] M. A. Henderson, Langmuir 12 (1996) 5093.

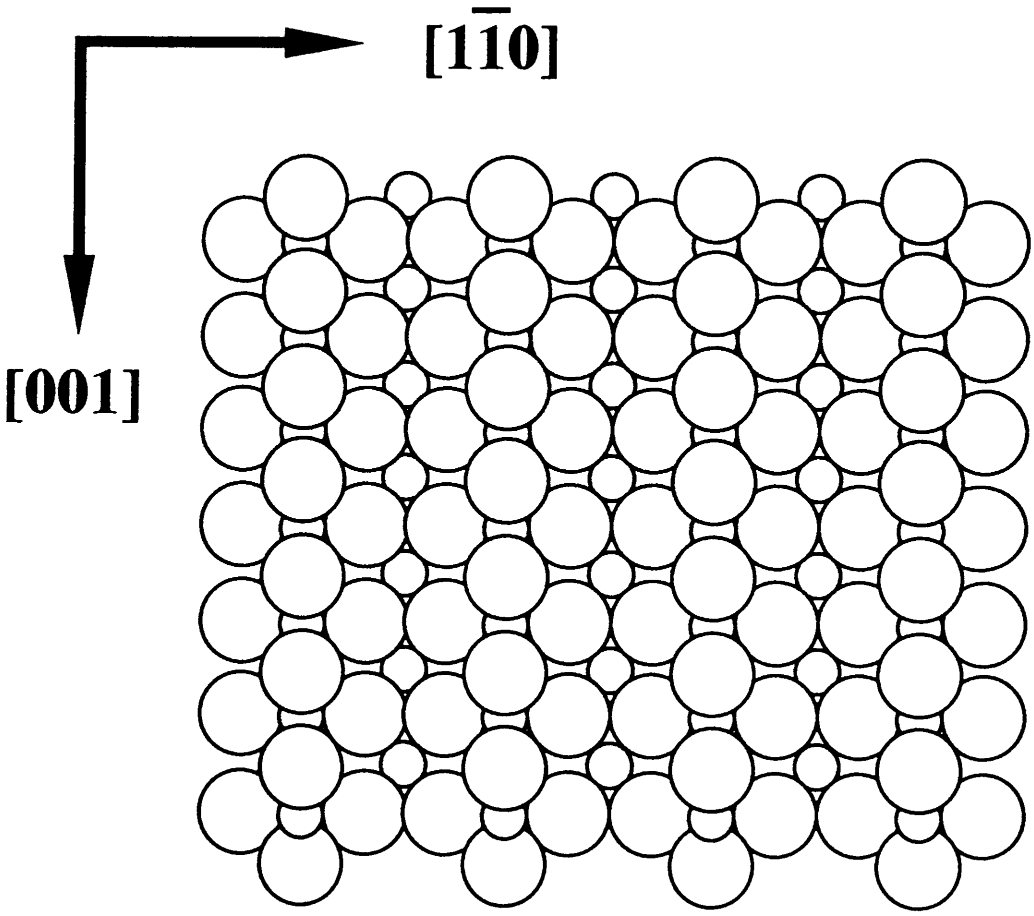

Figure 6.1 The model of TiO$_2$(110)-(1x1) surface (top view). Filled and open symbols represent titanium and oxygen atoms, respectively.

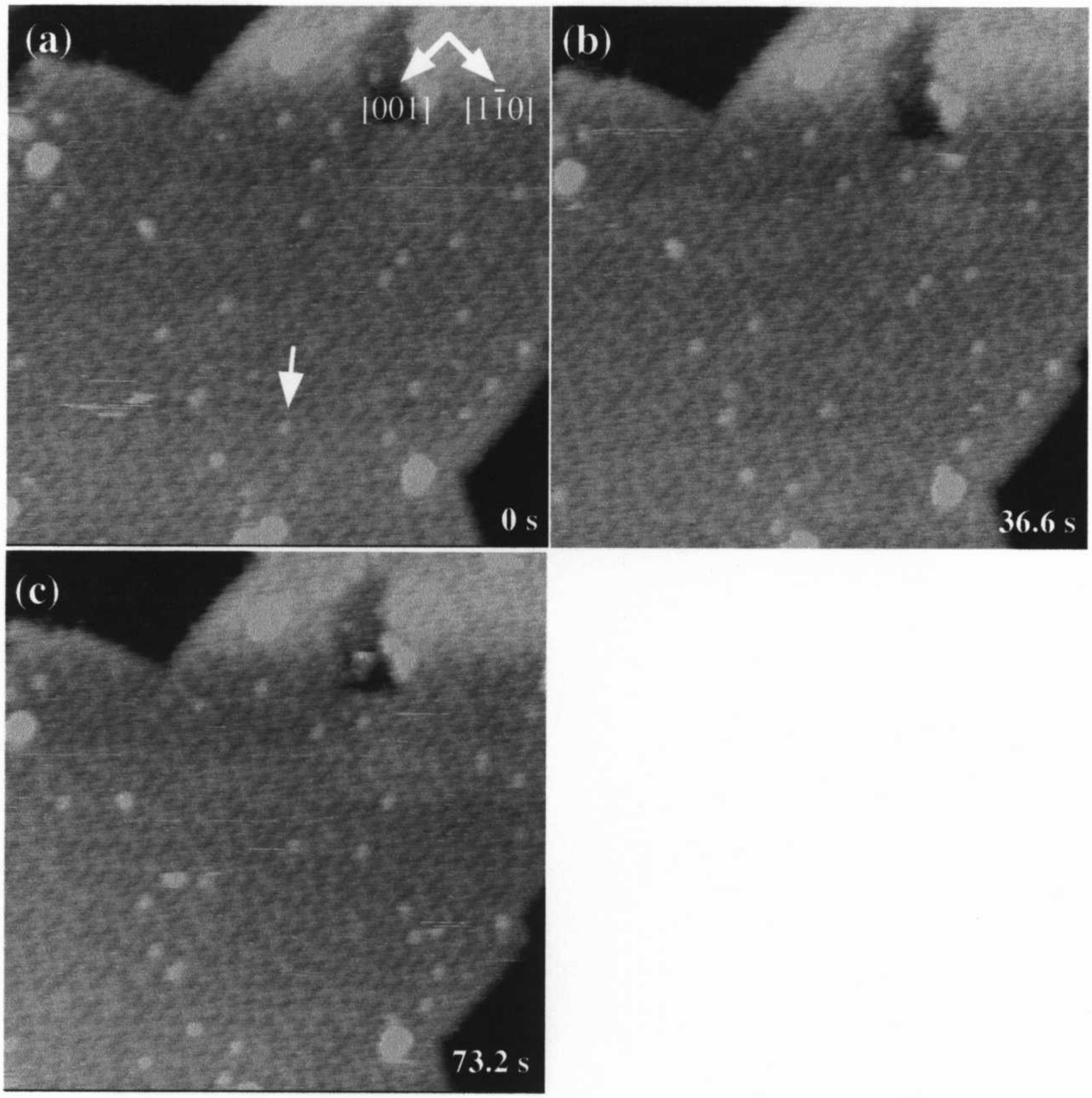

Figure. 6.2 Constant current STM images of a ammonia-exposed $TiO_2(110)$-(1x1) surface. Image (a) was recorded at room temperature on the surface exposed to 3 L ammonia vapor. Images (a), (b), and (c) were sequentially recorded at an interval of 36.6 s; sample bias voltage: +1.0 V, tunneling current: 0.05 nA, 27x27 nm^2.

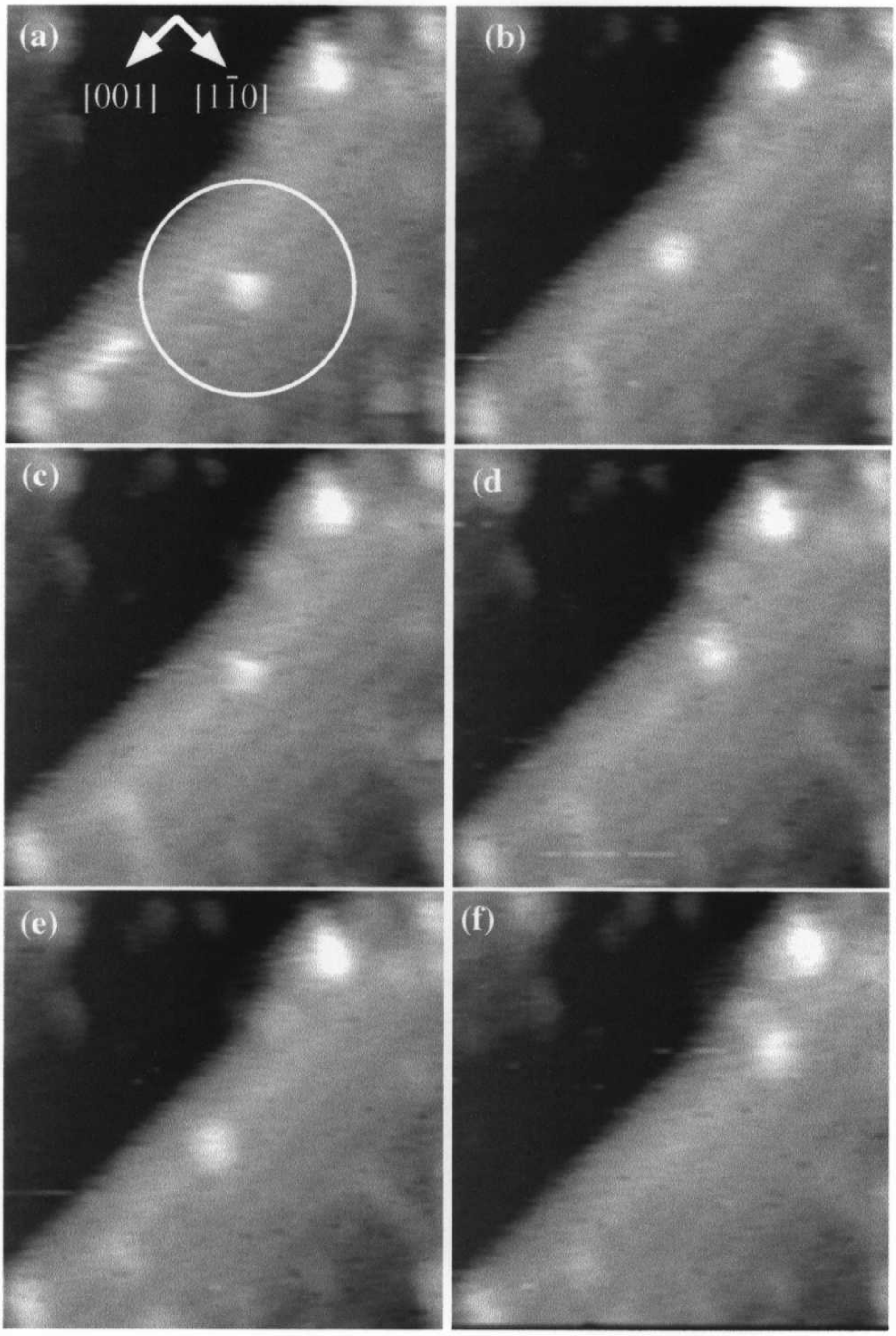

Figure. 6.3 Constant current STM images of a ammonia-exposed $TiO_2(110)$-(1x1) surface. Image (a) was recorded at room temperature on the surface exposed to 3 L ammonia vapor. Images (a) to (f) were sequentially recorded at an interval of 18.3 s; sample bias voltage: +1.0 V, tunneling current: 0.05 nA, 8x8 nm^2.

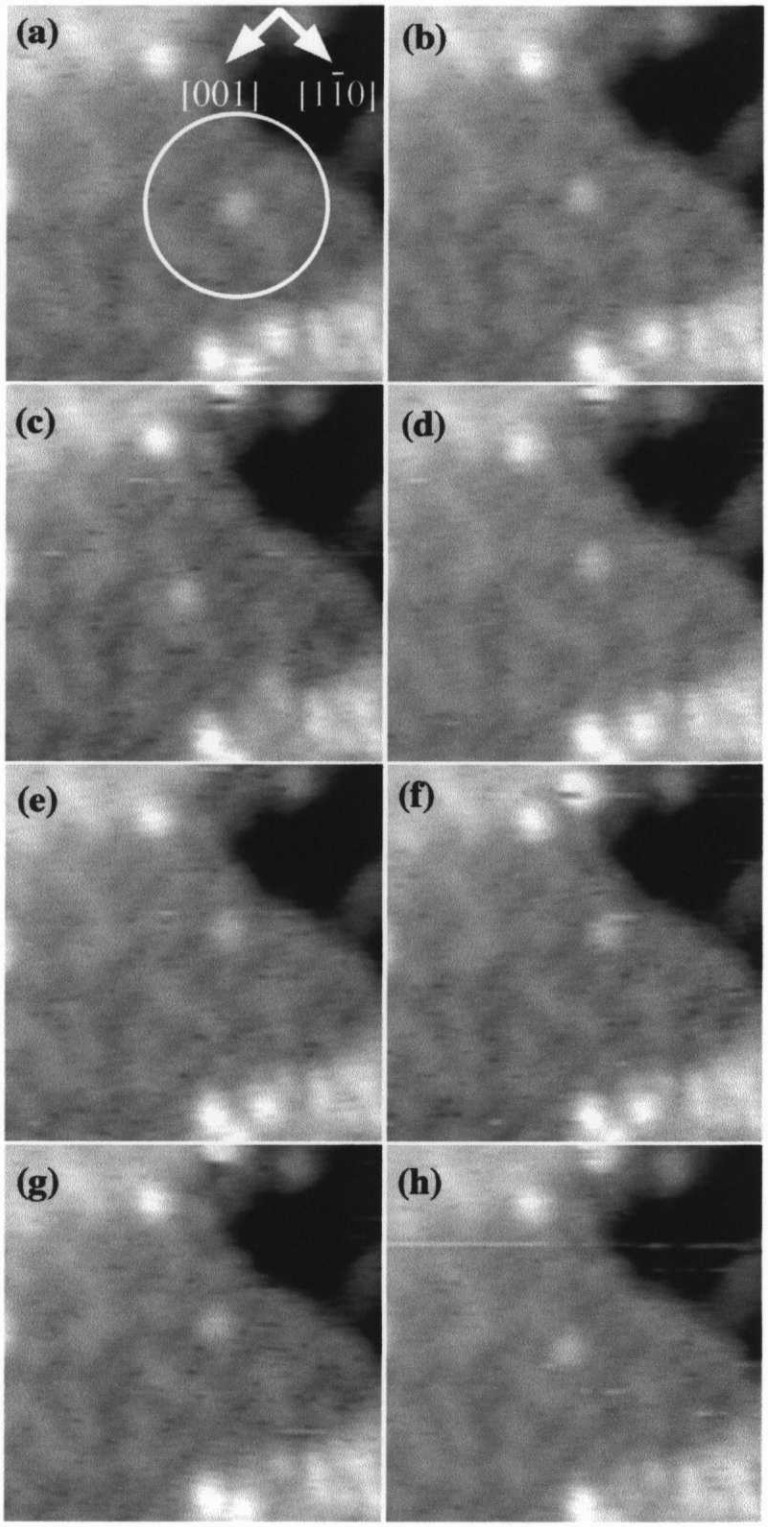

Figure. 6.4 Constant current STM images of a ammonia-exposed $TiO_2(110)$-(1x1) surface. Image (a) was recorded at room temperature on the surface exposed to 3 L ammonia vapor. Images (a) to (h) were sequentially recorded at an interval of 18.3 s; sample bias voltage: +1.0 V, tunneling current: 0.05 nA, 8x8 nm^2.

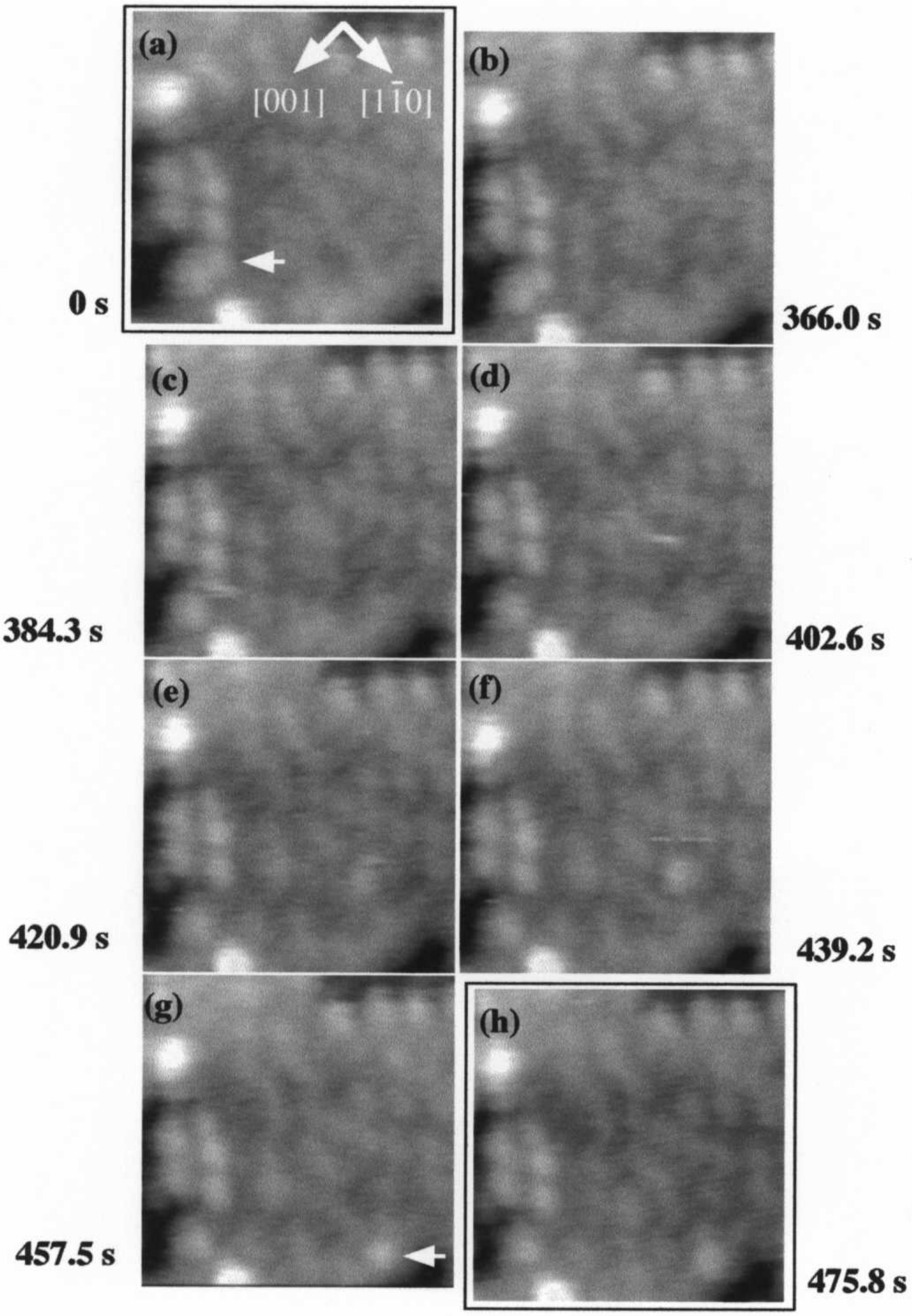

Figure. 6.5 Constant current STM images of a ammonia-exposed $TiO_2(110)$-(1x1) surface. Image (a) was recorded at room temperature on the surface exposed to 3 L ammonia vapor. Twenty and eleven frames were omitted between Figs. 6.5(a) to (b) and Figs. 6.5(g) to (h) with time interval of 366.0 s and 201.3 s, respectively. Figs. 6.5(b) to (g) show sequential STM images with time interval of 18.3 s; sample bias voltage: +1.0 V, tunneling current: 0.05 nA, 8x8 nm^2.

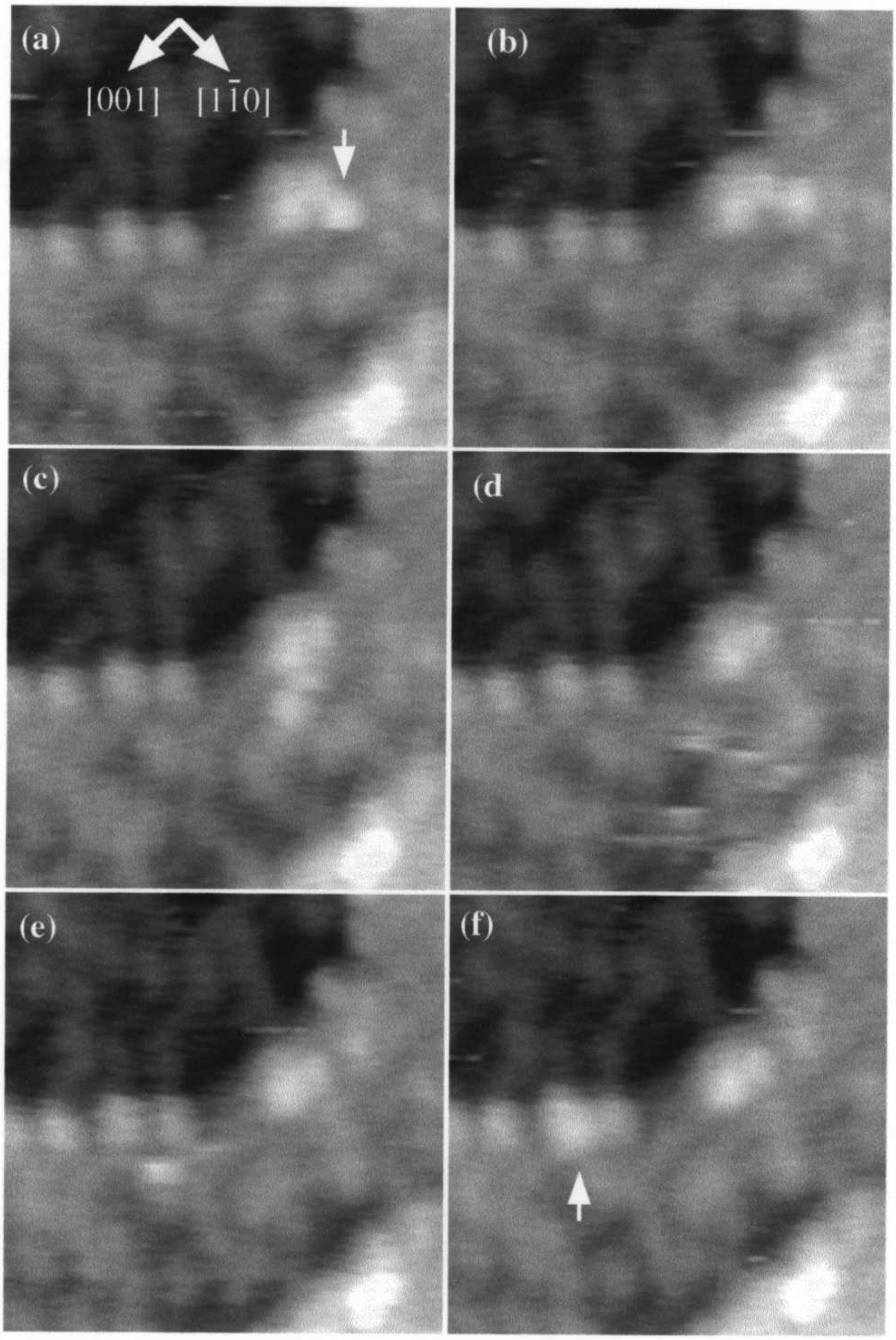

Figure. 6.6 Constant current STM images of a ammonia-exposed $TiO_2(110)$-(1x1) surface. Image (a) was recorded at room temperature on the surface exposed to 3 L ammonia vapor. Images (a) to (f) were sequentially recorded at an interval of 18.3 s; sample bias voltage: +1.0 V, tunneling current: 0.05 nA, 8x8 nm^2.

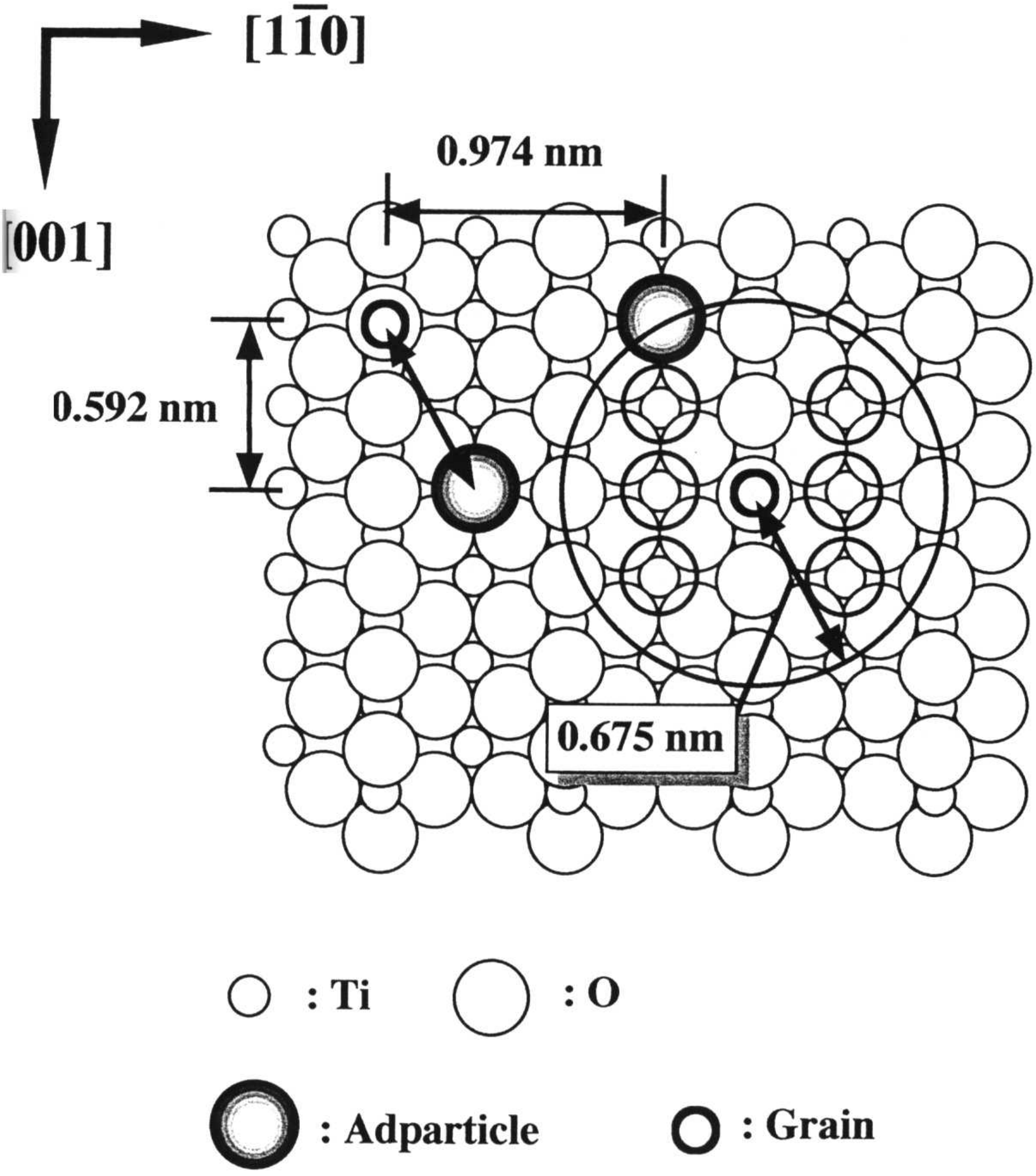

Figure 6.7 The schematic representation of the observed adaparticle and the grains on the model of TiO_2(110)-(1x1) surface (top view). The length between two species indicated in the model corresponds to the shortest distance actually observed by STM.

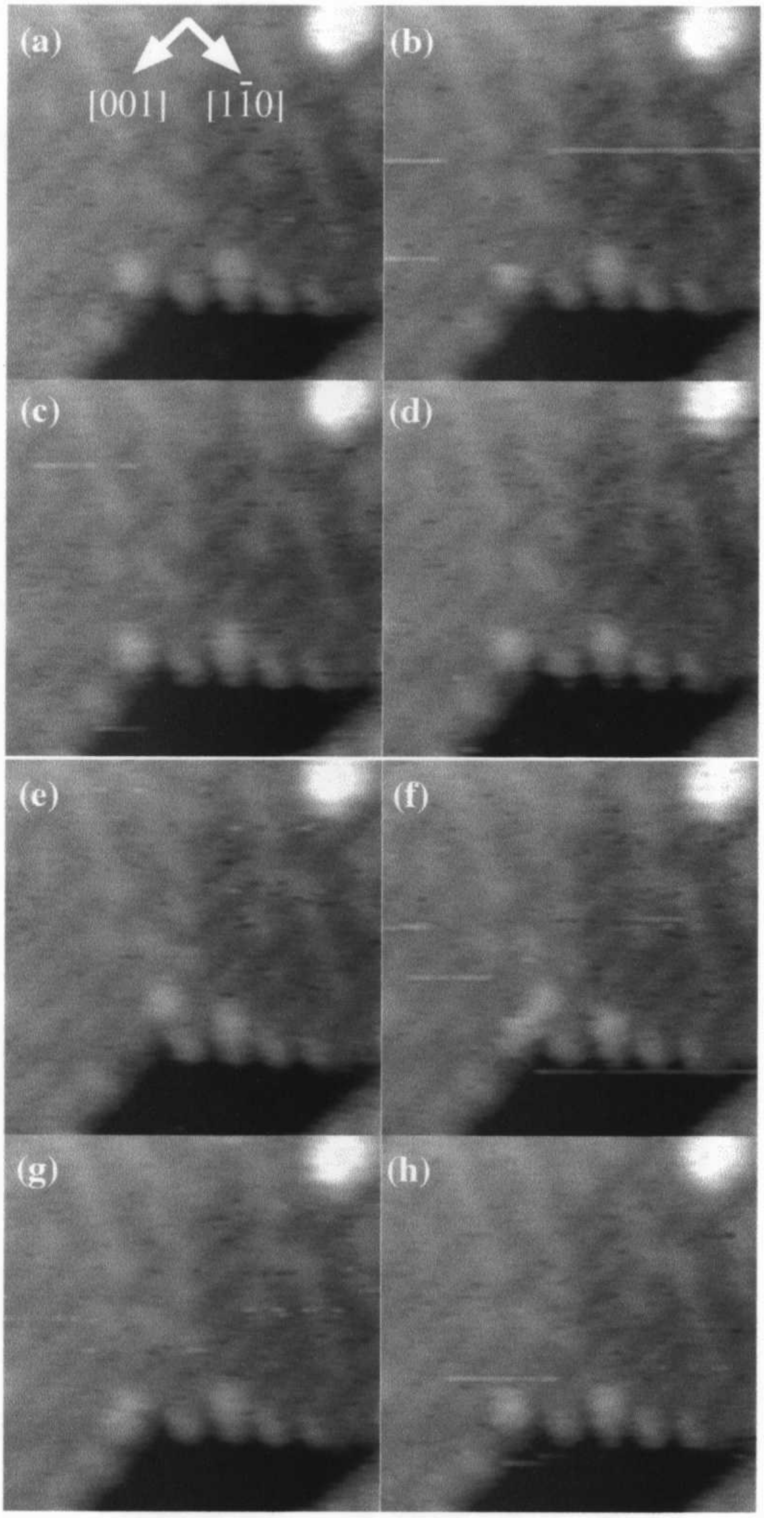

Figure. 6.8 Constant current STM images of a ammonia-exposed $TiO_2(110)$-(1x1) surface. Image (a) was recorded at room temperature on the surface exposed to 3 L ammonia vapor. Figs. 6.7(a) to (h) show sequential STM images with time interval of 18.3 s; sample bias voltage: +1.0 V, tunneling current: 0.05 nA, 8x8 nm^2. Step-bounded species were observed along the step edges.

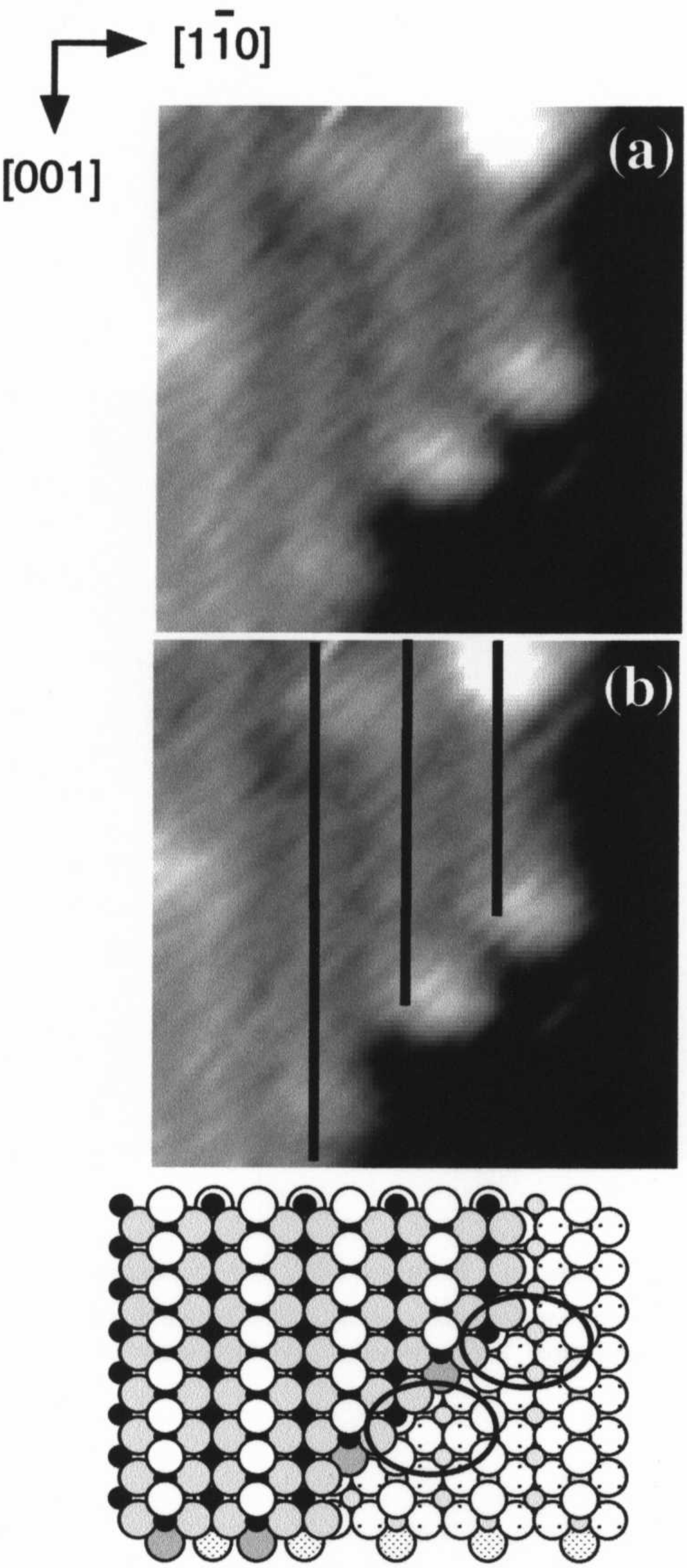

Figure 6.9 (a) An STM image of the ammonia-exposed TiO$_2$(110)-(1x1) surface. (b) the same image of (a) adding straight line representing Ti rows. (c) the corresponding structural model of the above image with circles representing the outline of the step-bounded species; sample bias voltage: +1.0 V, tunneling current: 0.05 nA, 4 x4 nm^2

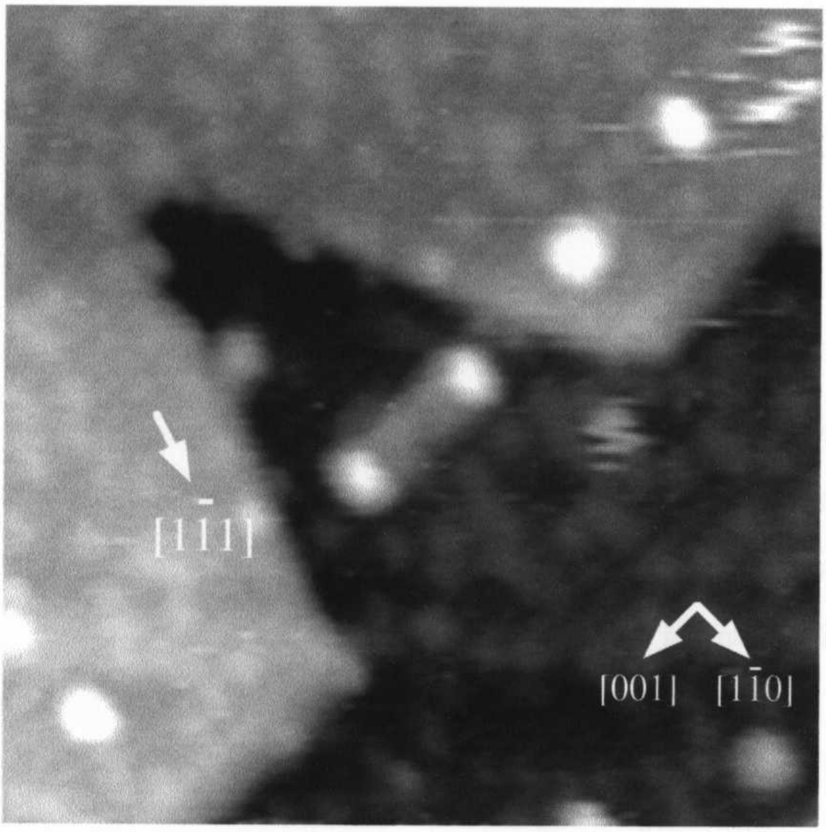

Figure. 6.10 Constant current STM images of a ammonia-exposed $TiO_2(110)$-(1x1) surface. Image was recorded at room temperature on the surface exposed to 3 L ammonia vapor; sample bias voltage: +1.0 V, tunneling current: 0.05 nA, 30x30 nm^2.

Chapter 7

The Condensation Reaction of Pyridine on $TiO_2(110)$: STM Observation in the Presence of the Reactant Atmosphere

Abstract

The thermally activated reaction of pyridine was studied by STM on a $TiO_2(110)$-(1x1) surface. At an unexpected low temperature of 350 K, the condensation reaction of pyridine is found. The formation and growth of the product particles were monitored in-situ on the surface heated at reaction temperatures (300-400 K) in the presence of pyridine atmosphere. A physisorbed pyridine molecule was activated at 350 K to form an intermediate, probably a partially dehydrogenated or chemisorbed state of pyridine. The intermediates aggregated into larger particles of nm-size. A gas-phase or physisorbed pyridine molecule is also directly involved in the particle growth reaction.

7.1 Introduction

In view of the acid-base concept, the reactivity of surface Lewis acid sites is directly related to their coordination number and evaluated by adsorption activity of base molecules on the sites. However, in the previous Chapters, the activity of Lewis acid sites was controlled by not only their coordination number but also their surroundings including 2nd nearest neighbor or further. The in situ STM studies of adsorption of base molecules on $TiO_2(110)$ (Fig. 7.1) revealed the Lewis acidity of the five-fold coordinated Ti sites on the terrace was significantly controlled by surrounding structural features such as oxygen vacancies of oxygen bridging rows and hydrogen atoms on bridging oxygen rows. On the other hand, the adsorption activity of the four-fold coordinated Ti sites at the steps was depended on the arrangement of atoms including next neighbors or further from the Ti sites. Therefore, these studies provided the preliminary understanding to examine chemical reactions of molecules on $TiO_2(110)$.

Here, the thermally activated reaction of pyridine was examined on $TiO_2(110)$ by in situ dynamic study in the presence of pyridine vapor. At an unexpected low temperature of 350 K, the condensation reaction of pyridine was found, and formation of secondary or ternary products was monitored by sequential STM imaging at 350 K. The condensation reaction of pyridine was not observed at 400 K, and in the absence of pyridine vapor.

7.2 Experimental

The experiments were performed with an UHV compatible scanning tunneling microscope (JSTM-4500VT, JEOL) equipped with an Ar ion gun and low energy electron diffraction (LEED) optics. A polished rutile $TiO_2(110)$ wafer of 6.5 x 1 x 0.25 mm3 (Earth Chemicals) was annealed in air at 1100 K for 1 h to remove carbonaceous contamination.

Nickel film was deposited on the back side of the wafer for resistive heating on the microscope stage. The temperature of the wafer was measured with an IR radiation thermometer. After several cycles of ion sputtering at 3 keV, 0.3 μA and vacuum annealing at 900 K, the surface comprising flat terraces was obtained with a sharp (1x1) LEED pattern. The (1x1) surface was cooled to room temperature and then exposed to pyridine (research grade, Wako Pure Chemicals) vapor. Constant current topography of the pyridine-exposed surface was recorded continuously (typically at a rate of 36.6 s/frame) with an electro-chemically etched W tip. A positive sample bias voltage (*Vs*) of +2.5 V and a tunneling current *(It)* of 0.05 nA were employed in imaging. The relatively small *It* favored stable and continuous observation under a gaseous ambience.

7.3 Results and Discussion

When the TiO_2(110)-(1x1) surface maintained at 350 K was exposed to pyridine vapor of 1 x 10^{-6} Pa, particles of a round shape appeared on the surface. Figure 7.2 shows a series of STM images recorded over 100 min under the pyridine atmosphere. The topography was presented in a simple gray scale. Two (110)-(1x1) terraces separated by single-height (0.3 nm) steps were imaged. A white patch at the upper right part is a small (110) island crystallized on the upper terrace. White string structures running along the [001] axis are Ti_2O_3 double-strand rows [8, 9], that were inevitably formed on sputter-annealed TiO_2(110) surfaces. Panel (e) illustrates the stacked terraces. Pyridine vapor of $1\text{x}10^{-6}$ Pa was introduced in the microscope chamber at *t*=0 during the continuous STM imaging. Panels (a)-(d) were determined at *t*=45, 72, 90, and 110 min, respectively. The number of the particles increased with the reaction time, *t*.

As is mentioned above in Chapter 3, pyridine molecules were physisorbed on the perfect TiO_2(110)-(1x1) surface at room temperature with their aromatic ring parallel to the surface, on the basis of thermal desorption, XPS, theoretical calculation, and STM results. The round-shape particles observed here are different compounds from the physisorbed molecules. The physisorbed species were mobile over the surface at the reaction temperature (350 K), and gave topographies of scratch shapes in Fig. 7.2. Very mobile species of similarly fragmented image shapes were observed on the (110)-(1x1) terrace exposed to pyridine vapor at 300 K and assigned to the physisorbed state in similar to Chapter 3. A quickly migrating molecule cannot stay at a position long enough to be properly imaged with scanning microscopy. The round shape of the particles in Fig. 7.2 indicates that the mobility of the particles is much less than that of the physisorbed pyridine molecule has. In fact, many of the particles once formed were observed at the same position in the image sequence. The obvious difference in mobility suggests that the particles are produced in thermally activated reactions of pyridine on this single crystal surface.

The size of the particles was determined by cross section analysis. The height of the particles ranged from 0.22 - 0.50 nm, while the full width at half maximum (FWHM) of the particle cross sections that represents their in-plane size was 0.78 - 1.72 nm. The certain distributions in the vertical and in-plane dimensions suggest that the less-mobile particle was produced by the reaction of a pyridine molecule on the surface and then gradually grow in the presence of pyridine vapor. The single pyridine molecule in the physisorbed state gave a round image of 0.26 nm-height and 1.2 nm-FWHM of cross section when the surface migration was frozen out at 100 K [11].

To examine how the particles grow on the surface at 350 K, the image sequence in Fig. 7.2 was zoomed-in and shown as panels (a)-(f) of Fig. 7.3. Two particles marked with X in (a) migrated along the [001] axis in opposite directions with a rate of 0.85 nm/min in (b), and merged into a larger particle Y in (c). Larger Y became less mobile than X and stayed at the same position in the last panel (f). This is a reaction between two reaction intermediates adsorbed on the surface. On the other hand, a particle (Z) of similar size to Y appeared in (e) and grew larger in (f). Pyridine molecules in the gas phase or in the physisorbed state should participate in the formation and growth of Z, since any intermediates like X were not observed in vicinity of Z.

The height and FWHM of cross section of X were determined to be 0.20 - 0.24 and 0.84 - 1.00 nm, respectively. These dimensions were slightly smaller than those of the physisorbed pyridine molecules immobilized at 100 K (0.26 nm-height and 1.2 nm-FWHM of cross section [11]). This suggests that X was produced from one pyridine molecule. A chemisorbed state of pyridine of the upright geometry ($C_5H_5N\text{-}Ti^{4+}$) or partially dehydrogenated state ($C_5H_{5-x}N$) are probable interpretations for X. The size of larger products like Y and Z was 0.3 - 0.5 nm in height and 1.08 - 1.72 nm in the FWHM of cross section. They are likely the products of condensation reaction of several pyridine molecules, though their composition is not known.

At 350 K, the particle formation reactions took place in the presence of pyridine vapor as presented above. At 300 K, the reaction proceeded so slow that few product particles were obtained by the reaction over one hour. This positive temperature dependence of reactivity indicates the thermal activated character of the reaction. However, the reaction did not occur on the surface exposed to a pyridine ambience of the same pressure at 400 K. Figure 7.4 shows the STM image of the surface exposed to the ambient for 60 min at 400 K and recorded at this temperature. Product particles were not observed at all in the image. To interpret the restricted reactivity observed at the higher temperature, we have to assume that pyridine molecules in the physisorbed state played a key role as an intermediate in the condensation reaction, i.e. a physisorbed pyridine molecule was transformed to the intermediate X identified in Fig. 7.3. In thermal desorption experiments, the physisorbed pyridine molecules desorbed at 300 - 350 K, as shown in Chapter 3. The physisorbed state should be depleted and hence the formation of X was prohibited on the surface heated at 400 K even in the presence of the pyridine atmosphere of 1×10^{-6} Pa.

On the other hand, the amount of the product particles strongly depended on the vapor phase pressure of pyridine at the same temperature, 350 K. The TiO_2 surface was exposed to pyridine of 1×10^{-6} Pa at 300 K and the atmosphere was evacuated. Then the surface that was rich in physisorbed pyridine molecules was heated at 350 K in UHV (5×10^{-8} Pa) for 110 min. Very small amount of the particles were observed on this surface as shown in Figure 7.5. The presence of the reactant in the gas phase positively affected the reaction at the surface.

When the TiO_2 surface was exposed to benzene vapor instead of pyridine, product particles were not formed at all. Nothing happened on the surface exposed to a benzene atmosphere of 1×10^{-6} Pa for 120 min at 300, 350 K, or 400 K. This shows the key role of the nitrogen atom in the activation of the reactant.

Based on the experimental results, the mechanism of the particle formation and growth is considered. A pyridine molecule physisorbed on the $TiO_2(110)$-(1x1) terrace is thermally activated at 350 K to form intermediate X (probably a partially dehydrogenated or chemisorbed state of pyridine),

a physisorbed pyridine -> X. (1)

In this step, the chemical interaction between the nitrogen atom and the surface, which could be related to the acid-base interaction in Lewis's definition, is important for the activation of the aromatic ring. When one X meets with another X, they are condensed into a larger and less-mobile product Y,

$$X + X \rightarrow Y. \quad (2)$$

It is also possible that two Xs simply aggregated to one Y without a chemical reaction. In addition to the adsorbate-adsorbate condensation, a gas-phase or physisorbed pyridine molecule is directly involved in the particle growth reaction, as shown in the growth of Z in Fig. 7.2(f).

gas-phase or physisorbed pyridine molecules -> Z (3)

Finally, it is to be noted that the condensation reaction of weakly physisorbed pyridine into particles observed in the present study should not be expected on TiO_2 surfaces, particularly on the most stable (110) surface. In the traditional acid-base scale for catalyst, TiO_2 belonged to a class of solid acids of moderate strength on which pyridine is used to probe the acidic property [1-7]. Nobody expects the activation and the subsequent condensation reaction of the probe itself near room temperature. The amount of the product particles was too small to be detected by macroscopic techniques like photoelectron spectroscopy and IR. The ultimate sensitivity of STM to identify one single product molecule on a solid surface enabled us to find the unexpected condensation reaction on the single crystalline substrate.

In summary, the unexpected condensation of weakly physisorbed pyridine was found on the TiO_2(110)-(1x1) surface by STM observation. The formation and growth of the product particles were monitored in-situ on the surface heated at reaction temperatures (300-400 K) in the presence of pyridine atmosphere. A pyridine molecule physisorbed on the surface was thermally activated at 350 K to form an intermediate (probably a partially dehydrogenated or chemisorbed state of pyridine). The intermediates aggregated into larger particles of nm-size. A gas-phase or physisorbed pyridine molecule is also directly involved in the particle growth reaction. The present study demonstrates that in-situ STM on a model catalyst is a promising method to find unknown reactions like the thermally activated condensation of pyridine on TiO_2.

References

[1] H. Onishi, Y. Yamaguchi, K. Fukui and Y. Iwasawa, J. Phys. Chem. 100 (1996) 9582.

[2] H. Onishi and Y. Iwasawa, Langmuir 10 (1994) 4414.

[3] H. Onishi, K. Fukui and Y. Iwasawa, Colloids and Surfaces A 109 (1996) 335.

[4] A. M. Youssef, M. N. Alaya and M. A. Hamada, Thermochim Acta 235 (1994) 91.

[5] I. E. Wachs, Catal. Today 27 (1996) 437.

[6] C. Morterra, G. Ghiotti and E. Garrone, J. Chem. Soc. Faraday I 76 (1980) 2102.

[7] M. Waqif, J. Bachelier, O. Saur and J. C. Lavalley, J. Mol. Catal. 72 (1992) 127.

[8] H. Onishi, K. Fukui and Y. Iwasawa, Bull. Chem. Soc. Jpn., 68 (1995) 2447.

[9] H. Onishi and Y. Iwasawa, Phys. Rev. Lett., 76 (1996) 791.

[11] S. Suzuki, H. Onishi, K. Fukui and Y. Iwasawa, to be submitted.

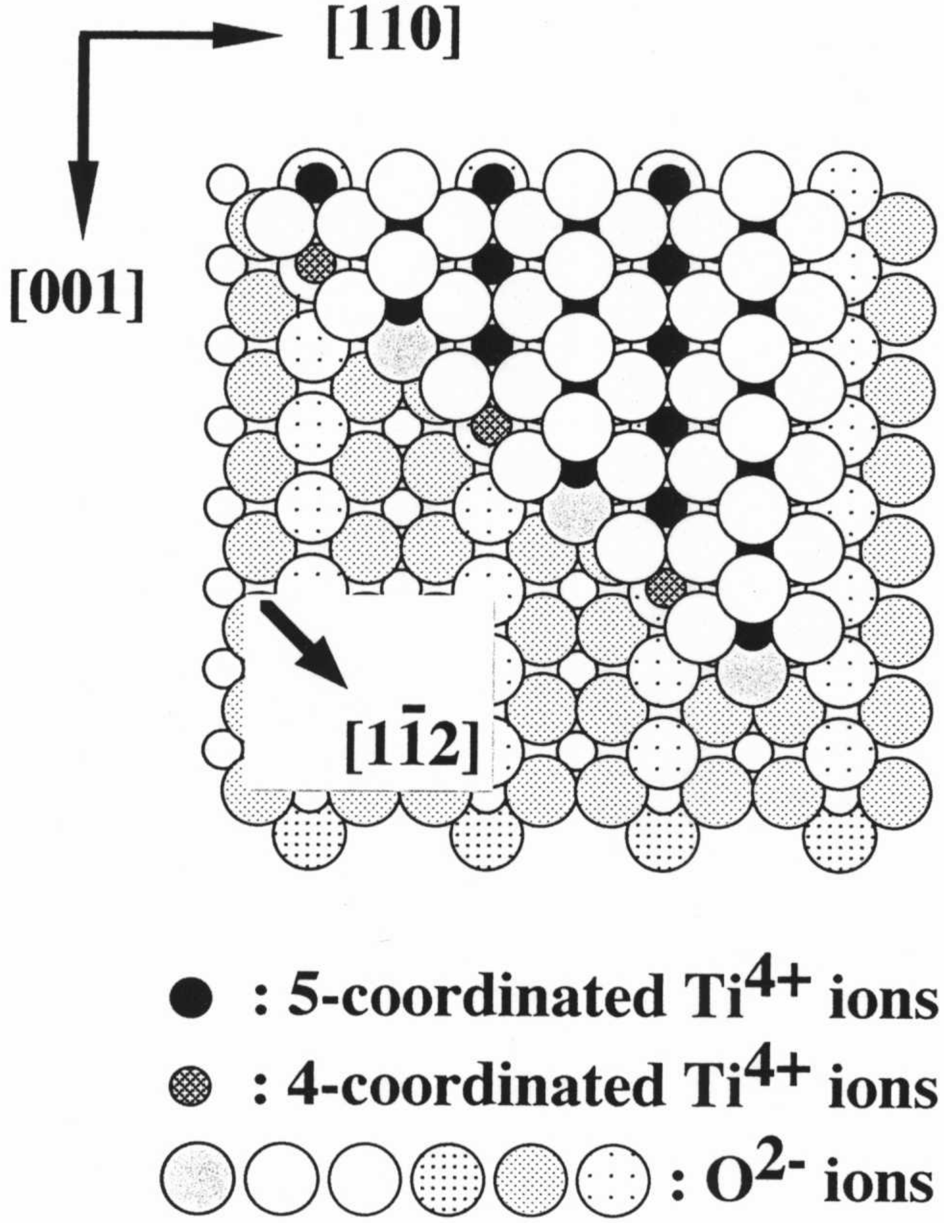

Figure 7.1. The top view of the TiO_2(110)-(1x1) surface with a single-height step along the direction.

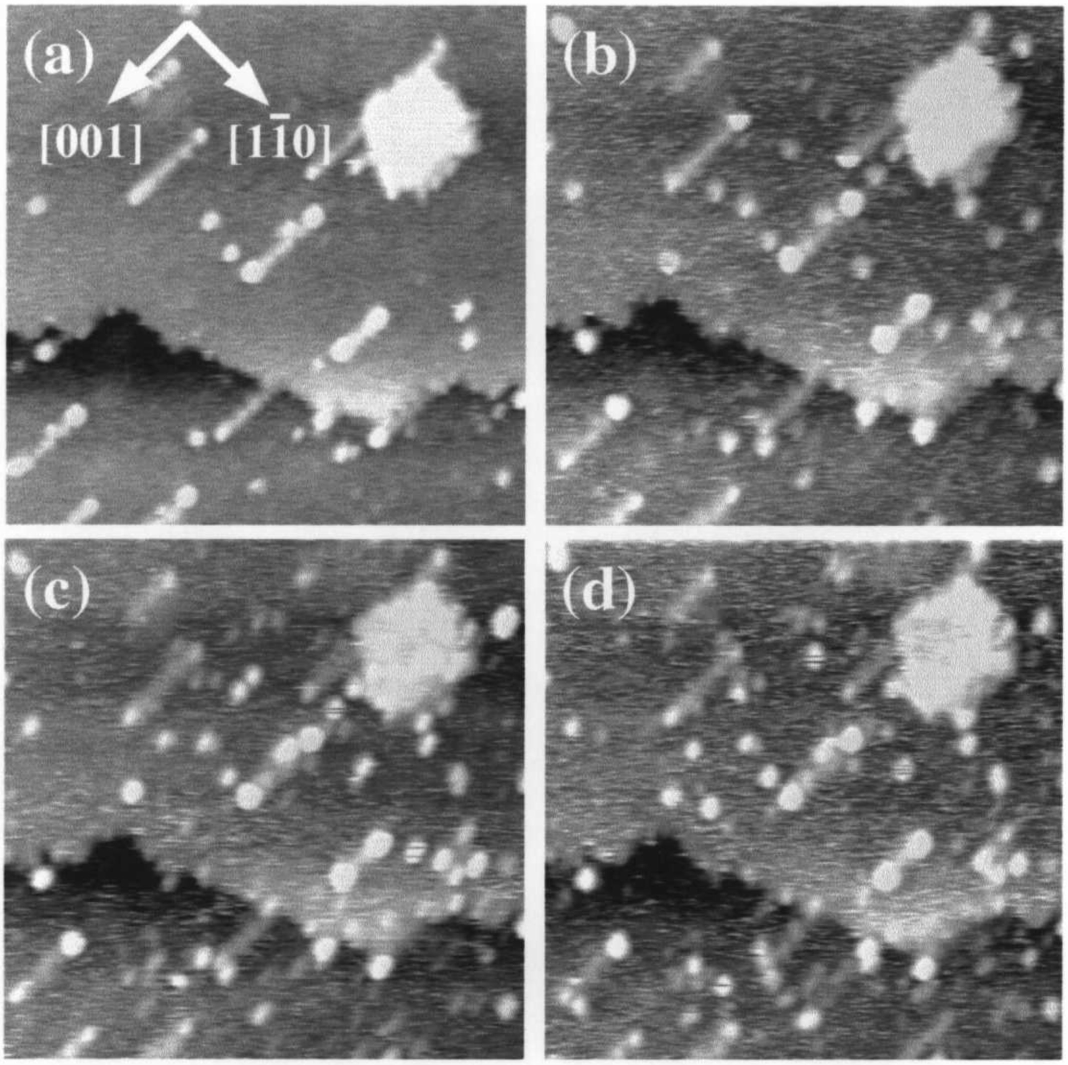

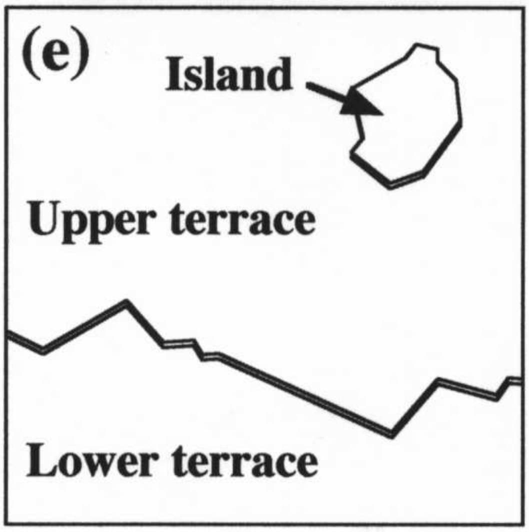

Figure 7.2. A series of STM images sequentially recorded on the $TiO_2(110)$-(1x1) surface heated at 350 K exposed to pyridine vapor of 1 x 10^{-6} Pa. Pyridine vapor was introduced in the microscope chamber at *t*=0. Images (a)-(d) were determined at *t*=45, 72, 90, and 110 min, respectively. Image size: 40x40 nm^2, sample bias voltage: +2.5 V, tunneling current: 0.05 nA. (e) illustrates the stacked terraces seen in (a)-(d).

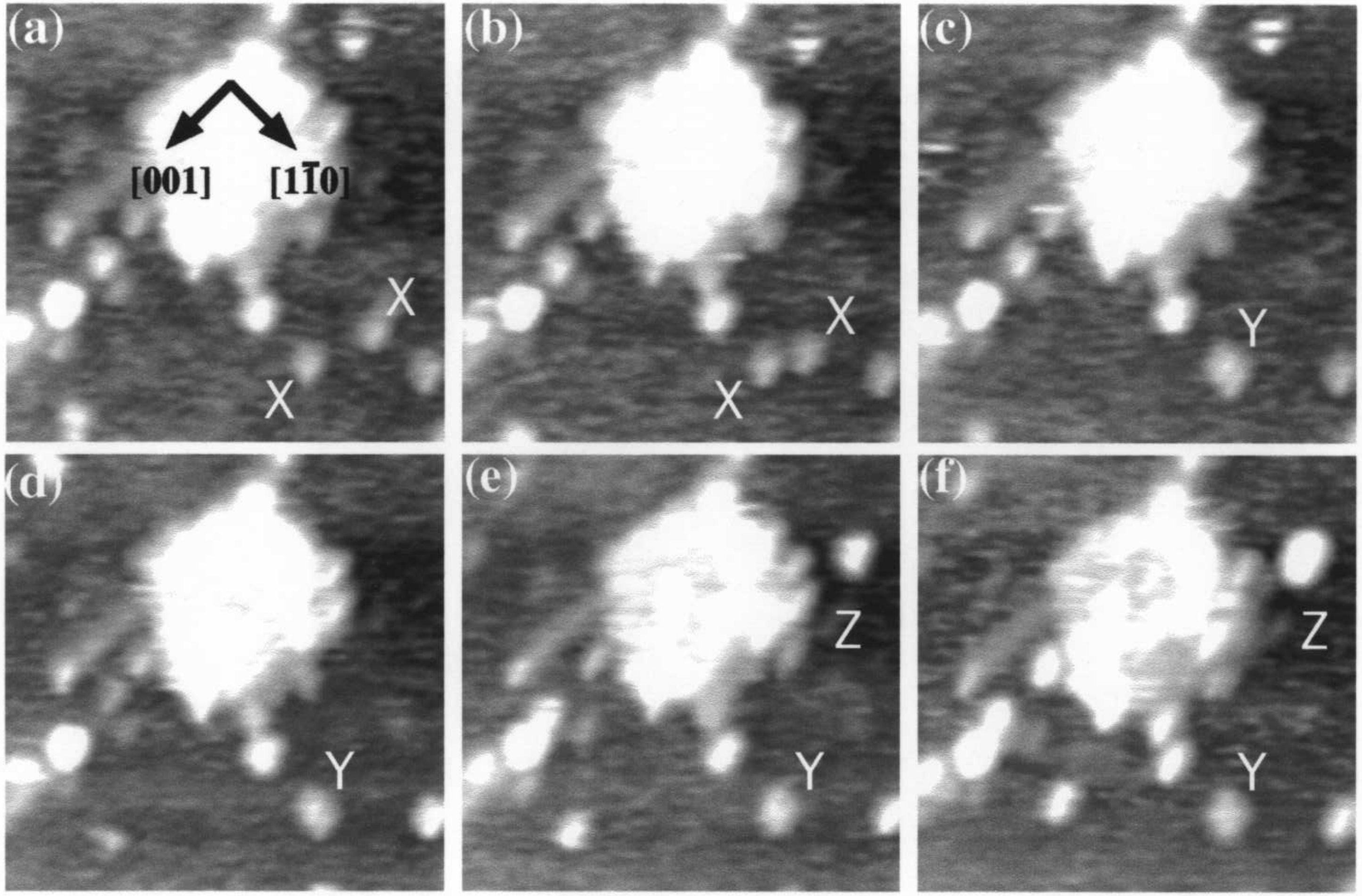

Figure 7.3. Zoomed-in images observed on the surface of Fig. 2. Images (a)-(f) were determined at *t*=73, 73.6, 74.2, 79.8, 84.7, and 87.7 min, respectively. Image size: 20x20 nm^2, sample bias voltage: +2.5 V, tunneling current: 0.05 nA.

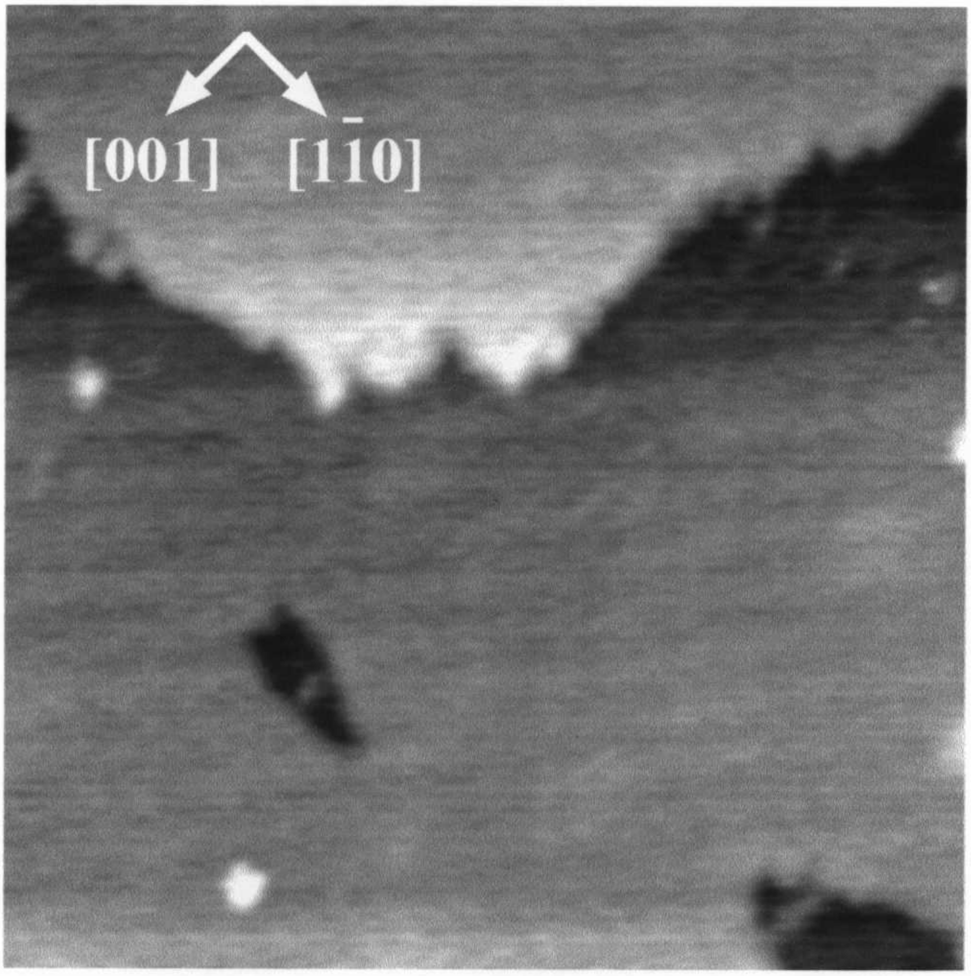

Figure 7.4. An STM image of the TiO_2(110)-(1x1) surface heated at 400 K and exposed to pyridine vapor of 1 x 10^{-6} Pa for 60 min. The image was determined on the surface maintained at 400 K. Image size: 42x42 nm^2, sample bias voltage: +2.5 V, tunneling current: 0.05 nA.

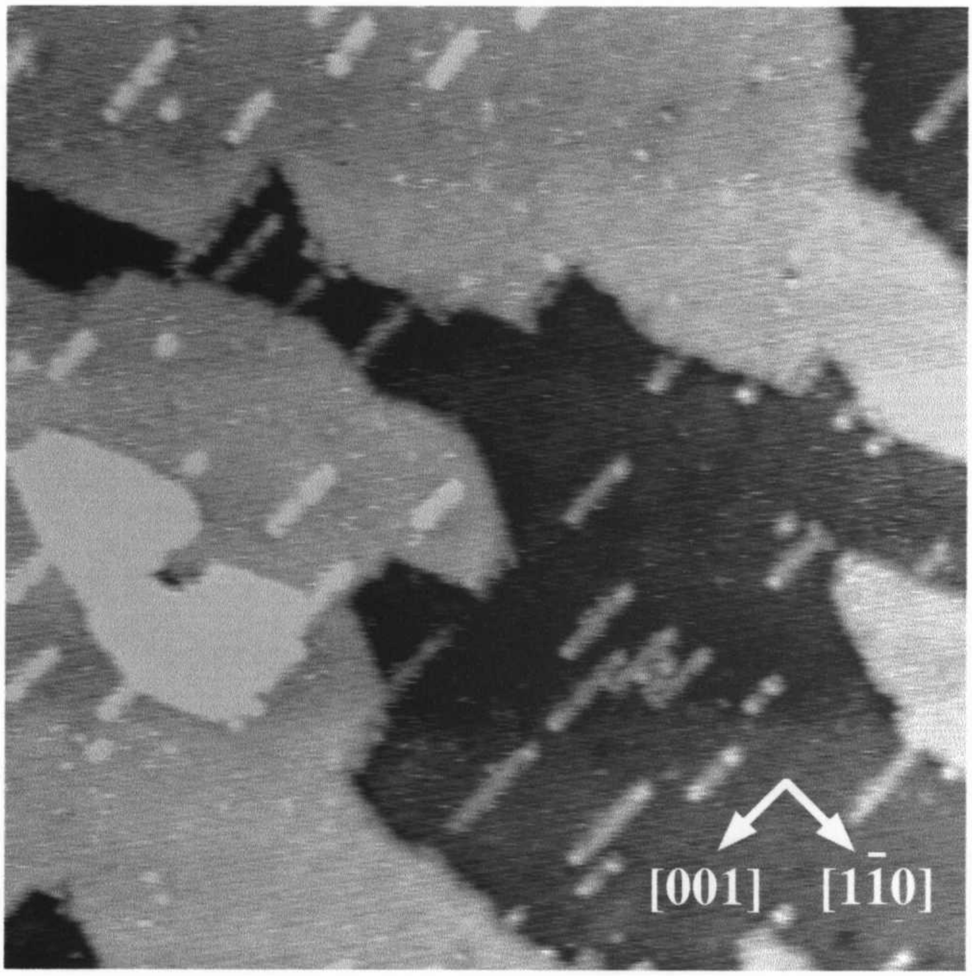

Figure 7.5. An STM image of the TiO_2(110)-(1x1) surface pre-exposed to pyridine of 1 x 10^{-6} Pa at 300 K and then heated at 350 K in UHV for 110 min. The image was determined on the surface at 350 K. Image size: 60x60 nm^2, sample bias voltage: +2.5 V, tunneling current: 0.05 nA.

Chapter 8

Hydrogen Adatoms on TiO_2(110)-(1x1) Characterized by Scanning Tunneling Microscopy and Electron Stimulated Desorption

Abstract

Hydrogen atoms adsorbed on TiO_2(110)-(1x1) surfaces have been characterized by scanning tunneling microscopy (STM) combined with electrons stimulated desorption (ESD) technique. Certain amount of H atoms are unexpectedly found on the TiO_2 surfaces annealed at 900 K. Two forms of adsorption were discriminated in STM images from the different sensitivity to ESD and tentatively assigned to hydroxyl-type (O-H) and hydride-type (Ti-H) species.

8.1 Introduction

Physics and chemistry of well-characterized metal oxide surfaces are of fundamental importance to develop industrial applications, such as catalysts, sensors, transparent electrodes, ceramics, bio-interfaces, etc. The application of surface science techniques to metal oxides has accepted increasing interests recently [1, 2]. Most of those studies, however, have mainly focused on characterization of clean surfaces (crystal wafers and thin films) as prepared by thermal annealing. Artificial control in composition and structure by using adatoms and admolecules as modifiers should be the forthcoming challenge to functionalize oxide surfaces.

In the present study, we examined hydrogen atoms adsorbed on TiO_2(110)-(1x1) surfaces by scanning tunneling microscopy (STM) combined with electrons stimulated desorption (ESD) technique. H atoms adsorbed on a metal oxide surface were individually visualized for the first time.

Hydrogen adatoms play a key role in reaction and modification at oxide surfaces. Some H atoms bound to surface oxygen of polycrystalline oxides are positively charged and hence exhibit affinity to electron-rich compounds [3]. Some others react with organometallic compounds to fix their metal cores on the oxide surface in a controlled manner [4, 5]. The creation and characterization of hydrogen adatoms on well-defined oxide surfaces is the first step for physical understanding and rational controlling of those phenomena. In addition, a hydrogen adatom is the simplest adsorbate convenient for theoretical calculation.

The (110) surface of rutile-type TiO_2 is the most extensively studied oxide surface as a model of stable truncation of transition metal oxide. A stoichiometric structure, shown in Fig. 8.1, has been proposed for the (1x1) phase [2], which is supported by physical techniques [6-11]. The unoccupied surface states localized on the exposed Ti atoms are imaged as bright lines or spots in STM topography determined with positive sample bias voltages [12].

8.2 Experimental

The experiments were performed in a scanning tunneling microscope (JEOL-JSTM4500VT). Polished $TiO_2(110)$ wafers of 6.5 x 1 x 0.25 mm^3 (Earth Chemicals) were calcined in air at 1000 K and then cleaned by cycles of Ar ion sputtering (3 keV, 0.3 μA, 2 min) and vacuum annealing (900 K, 30 s). The vacuum annealing made the wafers deep blue due to oxygen deficiency in the bulk. TiO_2 wafers thereby treated were transferred on the microscope stage without breaking vacuum. Constant current topography was determined at room temperature with Pt-Ir or W tip.

8.3 Results and discussion

A typical constant current topography of the $TiO_2(110)$-(1x1) surfaces is shown in Fig. 8.2a. Bright lines parallel to the [001] direction represent the rows of five-fold coordinated Ti atom [12]. Many bright spots of uniform size were observed in addition to the Ti-rows. The number of the spots was 143 which corresponds to and 0.07 monolayer (ML), where 1 ML is defined as the density of the (1x1) units, 5.2×10^{18} m^{-2}. The number density of the extra features ranged from 0.05 to 0.25 ML on the annealed wafers.

Topography of the extra features remarkably depended on sample bias voltage (V_s), as shown in Figs. 8.2a-d; They were presented as circular spots brighter than Ti-rows at Vs=+2.5 V (Fig. 8.2a). At V_s=+2.0 and +1.5 V (b and c), short rows in the $[1\bar{1}0]$ direction connected two [001]-oriented Ti-rows, so that we call them bridge-shaped features hereafter. At V_s=+1.0 V (d), the topographic height of the $[1\bar{1}0]$-oriented rows became close or slightly negative to the zero-level of the dark oxygen rows. Bias-dependent cross sections averaged over several images are illustrated in Fig. 8.2e. The extra features were located in the middle of Ti-rows at any bias voltages. The size of them was comparable with the out-of-plane amplitude and in-plane width of the periodic corrugation of Ti-rows. Thus, the bridge-shaped image is ascribed to one single adatom or atom-vacancy on the rows of protruding oxygen atoms.

When we attempted to observe the surface of Fig. 8.2 at V_s=+3.0 V, the bridge-shaped features disappeared. Figure 8.3 shows a zoomed-out image of the surface, where the 20 nm square at the center was scanned once with V_s=+3.0 V and tunneling current (I_t) of 0.30 nA. The features observed in Figs. 8.2a-d were removed, while those outside remained. This tip-induced phenomenon is easily interpreted as adatom manipulation driven by applied electric field, if one receives that the bridge-shaped topography comes from real particles adsorbed. In fact, formate ions ($HCOO^-$) adsorbed on TiO_2(110) were removed by a high-bias scan with V_s=+3.7 eV [13]. Atom vacancies would not be healed without any perturbations on the surface, even if some atoms were transferred from the tip to the surface during the high-bias scan. The high-voltage scan caused neither damage nor residuals on the surface. Titanium-rows were clearly seen in the manufactured area in Fig. 8.3. Thick bright lines in the [001] direction are Ti_2O_3 added rows formed on sputter-annealed TiO_2(110) surfaces [12], which are out of interest here.

Based on the arguments above, I presumed that an adatom creates a bridge-shaped image, and proceeded to determine the chemical identity of the adatom. Analysis by Auger and X-ray photoelectron spectroscopy failed to observe any impurities on the TiO_2 surfaces with the features. This absence of detectable impurity allows us to assume that hydrogen adatoms present bridge-shaped topography. A hydrogen atom adsorbed on a protruding, coordinatively unsaturated oxygen atom is stabilized as a hydroxyl group. The small topographic size (Fig. 8.2e) is consistent with the assumption. Adatoms of other elements likely exhibit larger topography than observed [14, 15].

To support this assumption of hydrogen adatoms, the electron stimulated desorption

(ESD) of the bridge-shaped features was examined. Knotek [16] observed desorption of H^+ and O^+ ions stimulated by electron irradiation on a $TiO_2(001)$ surface prepared by Ar ion sputtering and vacuum annealing at 1225 K. It is now established that core-level excitations and successive inter-atomic Auger decay processes cause the desorption. The H^+ desorption has a threshold at the O(2s) ionization potential (E~21 eV), whereas the O^+ desorption has a threshold at the Ti(3p) ionization (E~32 eV). Hence, we can expect the selective desorption of hydrogen from a TiO_2 surface by exposure to 20-eV electrons.

A sputter-annealed $TiO_2(110)$ surface was exposed to the electron beam generated by the LEED optics. The beam accelerated at 20 eV was focused on the grounded sample to create (1 0) diffraction spots on the screen. Beam current measured on the sample was 5.4 μA. Figures 8.4a and b present topography of the surface before and after electron irradiation for 360 min. The number of bridge-shaped features remarkably decreased in b without damaging the surface. Few large and bright particles are possibly impurities stemmed from the electron source. Number density of bridge-shaped features over several areas imaged was calculated. The density decreased from 0.13 to 0.04 ML during the first 60-min irradiation and became constant at 60-360 min, as shown in the left side of Fig. 8.4c. The two-step kinetics with the break at 60 min suggest that bridge-shaped features resident on the sputter-annealed surface contains two different types. A moderate order of ESD cross section, 10^{-23} m^2, was estimated for the desorbing species by assuming an exponential decay of density for the first 60 min. The observed ESD activity is strong evidence for the hydrogen adatom assumption. The irradiating electrons released Jourl heat of 0.1 mW on the surface and the according rise in temperature is negligible.

Finally, the electron-irradiated surface was exposed to atomic hydrogen and resultant H adatoms were imaged by STM. To make atomic hydrogen, a tungsten filament placed 50 mm away in front of the surface was heated up to ~1800 K, and H_2 gas (99.9995% purity) was leaked in the chamber at $1x10^{-6}$ Pa. The number of bright spots increased with exposure time and saturated at 0.23 ML as shown in the right side of Fig. 8.4c. The newly appeared bright spots in Fig. 8.4d exhibited the size and shape identical to those observed in Fig. 8.2. When the saturated surface in Fig. 8.4d was irradiated with 20-eV electrons, the number density of the spots was decreased again to the minimum of 0.04 ML.

To interpret all the results mentioned above, we propose that (1) hydrogen atoms adsorbed on the protruding oxygen rows present the bridge-shaped topography, (2) 20-eV electrons stimulate the hydrogen adatoms to desorb, and (3) the hydrogen adatoms still exist on TiO_2(110) surfaces prepared by the Ar ion sputtering and vacuum annealing.

One may ask how hydrogen atoms are provided on the sputter-annealed TiO_2 surfaces. Knotek [16] observed H^+ desorption on TiO_2(001). Souda [17] found hydrogen atoms covering $SrTiO_3$(100). A possible route is the dissociative adsorption of residual water molecules from gas phase. Water is dissociated at coordinatively unsaturated metal sites like oxygen vacancies [18]. Hydrogen diffusion from bulk to surface can also occur as proposed on $SrTiO_3$ [17]. The TiO_2 crystals used in the present study may contain small amount of water or hydrogen. They were grown by Bernoulli method where TiO_2 melted and crystallized in H_2-O_2 flame.

A fraction (0.04 ML) of bridge-shaped features remained on the TiO_2 surface irradiated by 20-eV electrons (Fig. 8.4). The minor species can be assigned to H adatoms trapped at oxygen vacancies. When a H atom is bound to a vacancy of protruding oxygen atom (Fig. 8.1c), a hydride-like Ti-H bond is formed. Knotek [16] observed thresholds at 21 and 32 eV in H^+ desorption yield as a function of electron energy, and interpreted them as the ionization thresholds of O(2s) and Ti(3p) levels, respectively. The H-atom on O-vacancy is thus stable against the bombardment with 20-eV electrons. The coverage of the remaining features was comparable to the amount of oxygen vacancies (0.03-0.01 ML) observed on TiO_2 surfaces annealed at 900 K by noncontact atomic-force microscopy [19].

Diebold et al. [20, 21] and Xu et al. [22] found extra spots in STM topography of a TiO_2(110) surface prepared by vacuum annealing. They proposed that an oxygen vacancy present the spot, by comparing the observed topography with theoretical prediction [20]. Topography of their spots (for example Fig. 8.4 of ref. [21]) is quite close of the bridge shape of the features imaged in the present study. If they observed the same objects as we observed, their assignment to oxygen vacancy should be re-examined. While a sputter-annealed $TiO_2(110)$ surface contains oxygen vacancies in general, it can be difficult to identify a simple hydrogen adatom, a simple vacancy of oxygen, and a hydrogen atom trapped at the vacancy, based on STM topography alone. To discriminate those related species, STM topography obtained experimentally and theoretically should be carefully compared. Local density of states observation by scanning tunneling spectroscopy (STS) will be helpful. Surface states localized on oxygen vacancies were observed on $SrTiO_3(100)$ [23]

8.4 Conclusion

Extra features were observed in constant current topography of $TiO_2(110)$ surfaces prepared by Ar ion sputtering and vacuum annealing. The coverage of the feature ranged at 0.25-0.05 ML being dependent on preparation history. They were assigned to hydrogen atoms adsorbed on rows of protruding oxygen atoms on the basis of the following experimental results; an atom size and bridge-shaped topography was observed at V_s=+2.5-1.0 eV. The features were removed from the surface without any damage or residuals, when the surface was scanned at V_s=+3.0 eV. 20-eV electrons stimulated a major part of the features to desorb with a cross section of 10^{-23} m^2. The number of bridge-shaped features increased by exposure to an atomic hydrogen flux. The minor species that 20 eV electrons could not stimulate to desorb are likely hydrogen atoms bound to oxygen vacancies.

References

[1] *Adsorption on Ordered Surfaces of Ionic Solids and Thin Films*, edited by E. Umbach and H.J. Freund (Springer, Berlin, 1993).

[2] V.E. Henrich and P.A. Cox, *The Surface Science of Metal Oxides* (Cambridge University Press, Cambridge, 1994).

[3] B.C. Gates, *Catalytic Chemistry* (Wiley, New York, 1992).

[4] *Tailored Metal Catalysts*, edited by Y. Iwasawa (Reidel, Dordrecht, 1986).

[5] Y. Iwasawa, Stud. Surf. Sci. Catal. (Proc. 11th Int. Congr. Catal., Baltimore) 101 (1996) 21.

[6] B.L. Maschhoff, J.-M. Pan, and T.E. Madey, Surf. Sci. 259 (1991)190 .

[7] G. Charlton, P.B. Howes, C.L. Nicklin, P. Steadman, *et al.*, Phys. Rev. Lett. 78 (1997) 495 .

[8] B. Hird and R.A. Armstrong, Surf. Sci. Lett. 420 (1999) L131 .

[9] M. Ramamoorthy, D. Vanderbilt, and R.D. King-Smith, Phys. Rev. B 49 (1994) 16721.

[10] S.P. Bates, G. Kresse, and M.J. Gillan, Surf. Sci. 385 (1997) 386 .

[11] N.M. Harrison, X.-G. Wang, J. Muscat, and M. Scheffler, Faraday Discuss. 114 (1999) in press.

[12] H. Onishi, K. Fukui, and Y. Iwasawa, Bull. Chem. Soc. Jpn. 68 (1995) 2447 .

[13] H. Onishi and Y. Iwasawa, Jpn. J. Appl. Phys. 33 (1994) L1338 .

[14] H. Onishi and Y. Iwasawa, Chem. Phys. Lett. 226 (1994) 111 .

[15] H. Onishi and Y. Iwasawa, Catal. Lett. 38 (1996) 89 .

[16] M.L. Knotek, Surf. Sci. 91 (1980) L17 .

[17] R. Souda, Phys. Rev. B 60 (1999) 6068 .

[18] R.L. Kurtz and V.E. Henrich, Phys. Rev. B 26 (1982) 6682 .

[19] K. Fukui, H. Onishi, and Y. Iwasawa, Phys. Rev. Lett. 79 (1997) 4202 .

[20] U. Diebold, J.F. Anderson, K.-O. Ng, and D. Vanderbilt, Phys. Rev. Lett. 77 (1996) 1322.

[21] U. Diebold, J. Lehman, T. Mahmoud, M. Kuhn, *et al.*, Surf. Sci. 411 (1998) 137 .

[22] C. Xu, X. Lai, G.W. Zajac, and D.W. Goodman, Phys. Rev. B 56 (1997) 13464 .

[23] H. Tanaka, T. Matsumoto, T. Kawai, and S. Kawai, Jpn. J. Appl. Phys. 32 (1993) 1405.

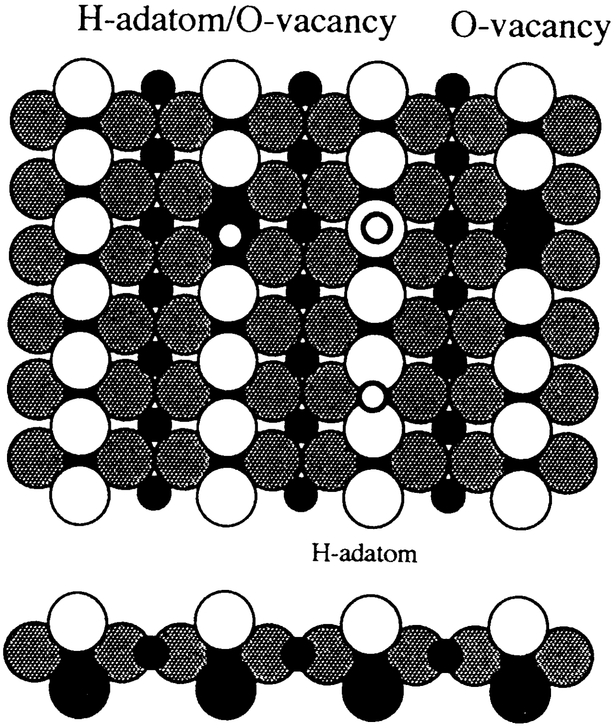

Figure 8.1. The stoichiometric structure of $TiO_2(110)$-(1x1) surface. Small filled spheres and large spheres represent titanium and oxygen atoms, respectively. A hydrogen atom adsorbed on a protruding oxygen atom(s), a vacancy of protruding oxygen atom, and a hydrogen atom trapped at the oxygen vacancy are illustrated. Top and side views are shown.

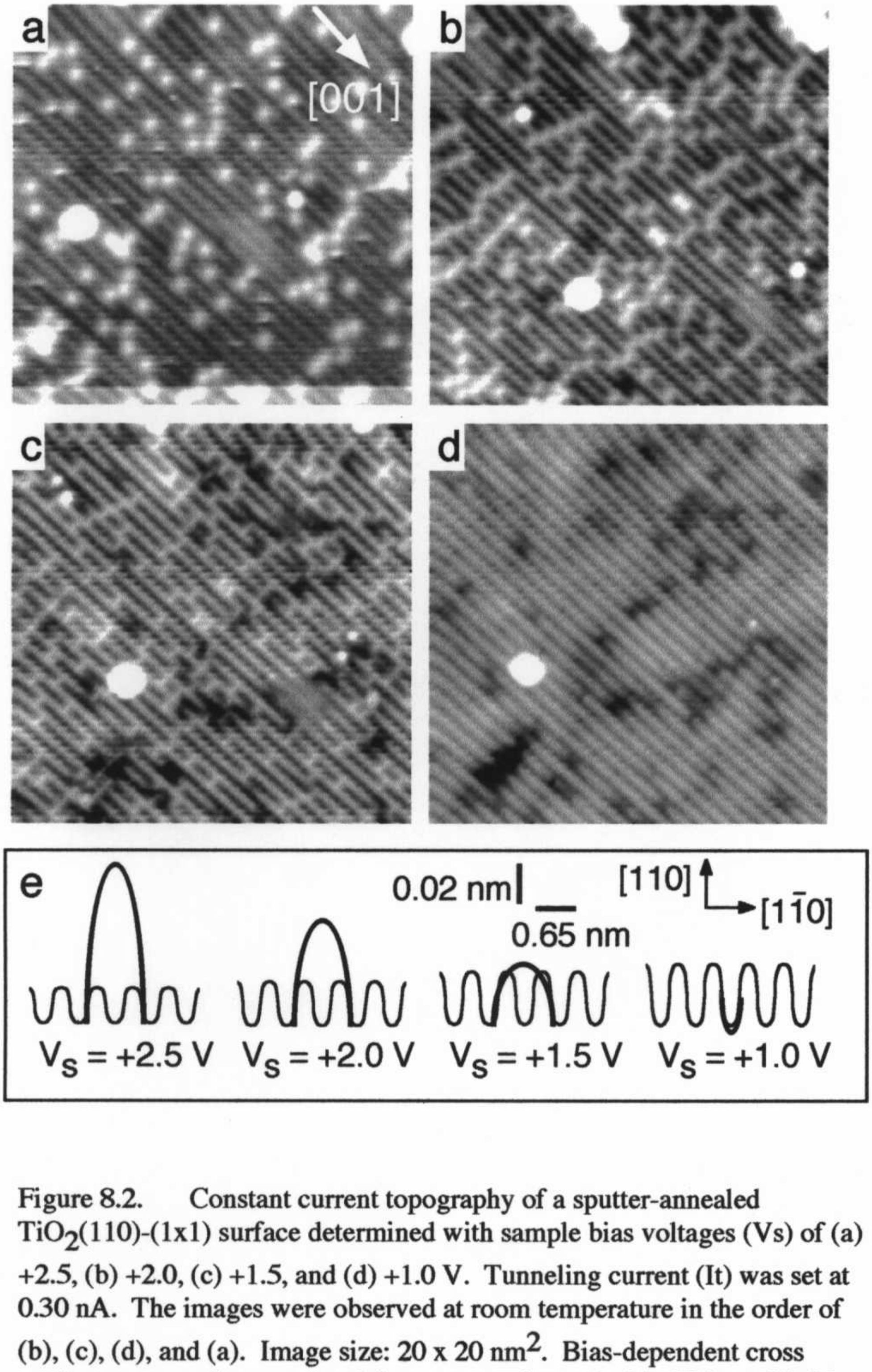

Figure 8.2. Constant current topography of a sputter-annealed TiO$_2$(110)-(1x1) surface determined with sample bias voltages (Vs) of (a) +2.5, (b) +2.0, (c) +1.5, and (d) +1.0 V. Tunneling current (It) was set at 0.30 nA. The images were observed at room temperature in the order of (b), (c), (d), and (a). Image size: 20 x 20 nm^2. Bias-dependent cross sections averaged over several features are shown in (e). Thin and bold lines show constant current topography of Ti-rows and the extra features.

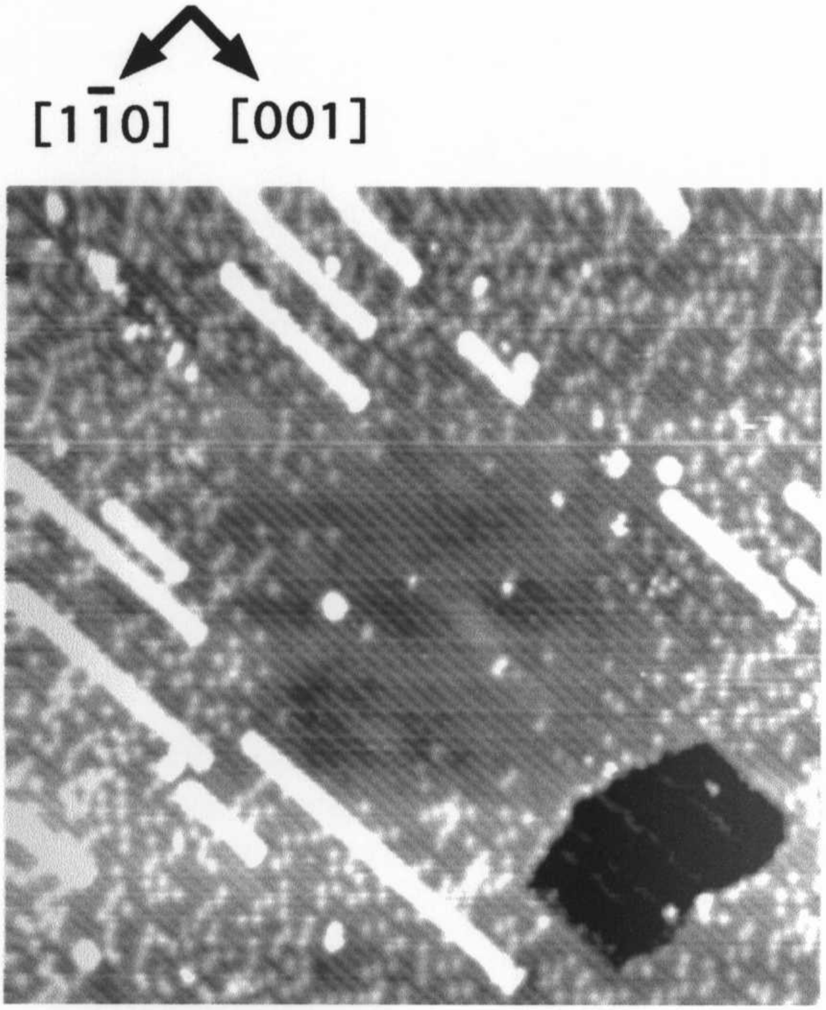

Figure 8.3. Constant current topography of the surface in Fig. 8.2 following a high-bias scan for manipulation. Manipulation scan: 20 x 20 nm^2, Vs=+3.0 V, It=0.30 nA; Imaging scan: 50 x 50 nm^2, Vs=+2.0 V, It=0.30 nA.

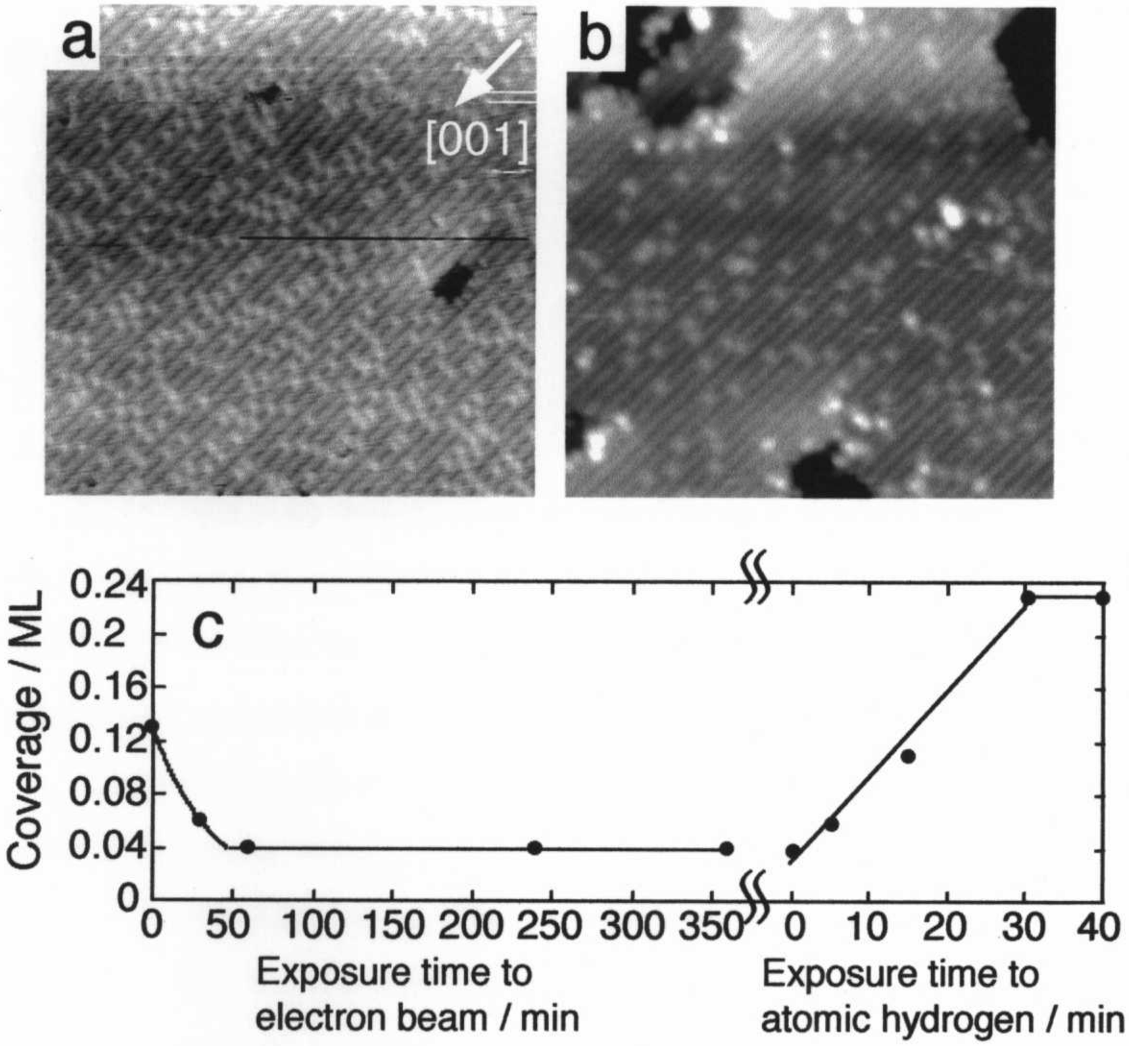

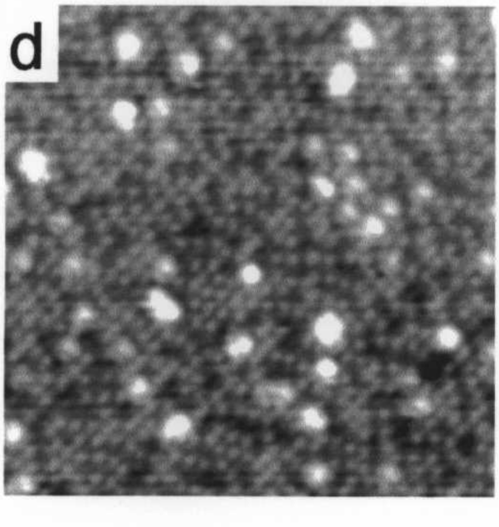

Figure 8.4. Constant current topography of a sputter-annealed $TiO_2(110)$ surface (a) before and (b) after exposure to electrons accelerated at 20 eV for 360 min. Image size: 25 x 25 nm^2, Vs=+1.5 V, It=0.05 nA. Number density of bridge-shaped features is plotted in the left side of (c) as a function of irradiation time. (d) Constant current topography of the surface in Fig. 4b exposed to hydrogen atoms for 30 min. Image size: 25 x 25 nm^2, Vs=+1.5 V, It=0.05 nA. Number density of bridge-shaped features is plotted in the right side of (c) as a function of exposure time.

Chapter 9

Concluding Remarks

All the study of my doctoral thesis has been done by in situ STM observation along the purpose of exposing essentials for catalytic reaction on a metal oxide. In particular, understanding the relation between catalytic reactions and the acid-base concept in view of structural features at the atomic level was main issue throughout this thesis.

The contents were divided into about three parts. Chapters 3, 4, 5, 6 and 7 were the first part, devoted to the studies of adsorption of base molecules: pyridine, its derivatives and ammonia on the $TiO_2(110)$ surface. The results in these Chapters revealed that not only their coordination number but also their surroundings including 2nd nearest neighbor or further controlled the activity of Lewis acid sites. The five-fold coordinated Ti sites on the terrace was originally active, but their activity was significantly controlled by their surroundings such as oxygen vacancies of bridging oxygen rows and hydrogen atoms on that in the case of aromatic base molecules and in the case of ammonia, respectively. The adsorption activity of the four-fold coordinated Ti sites at the steps was also depended on the next neighbor atoms or further from the Ti sites. Since such activity dependence was not related to the size of base molecules, the electronic structure decided by atom arrangements involving next nearest neighbor or further was perhaps dominant factor. As is traditionally mentioned, these Chapters indicated that there was a difference certainly in evaluation of Lewis acidity when aromatic base molecules and ammonia were selected. However, it was important that the difference was not due to own molecule, the molecular size effect sometimes pointed out, but the intrinsic nature of the

$TiO_2(110)$ single crystal. The above Chapters also provided the preliminary understanding to examine chemical reactions of molecules on $TiO_2(110)$ for the present.

The second part was the study actually examining in situ STM observation of chemical reaction of pyridine at the atomic level under reaction conditions. The purpose of this study was to exhibit the direct evidence on the relation between the active sites for the reaction and the Lewis acidity. Chapter 7 demonstrates surface reactions of pyridine at 350 K under gaseous reactants. As a mater of fact, the reaction of pyridine at such low temperature was unexpectedly observed by STM under gaseous reactants. In this experiment, sequential recording of STM images have been successfully done for 5 h at the maximum, though scan area fixing was hand-operated tracking. Individual physisorbed or chemisorbed pyridine, and processes of forming products were visualized directly at the atomic level, although the surface reaction sites could not been specified, unfortunately. However, such chemical processes was probably related to oxygen vacancies of bridging oxygen rows, since the oxygen vacancies was the only site which can chemically interact with weakly adsorbed pyridine. The surface reaction of pyridine at 350 K was truly unexpected, because pyridine was conventionally used as a base probe molecule. The reason why pyridine is a base molecule is having stability of thermal reaction in such temperature region. The experiments might only demonstrate the condensation reaction of pyridine occurred under the truly specific condition. However, what makes exception of the macroscopic study may occurred from the overlooking like this.

The content of Chapter 8 as the third part provided the solution of controversy whether the oxygen vacancies or hydroxyl-like species were imaged as the bright spots upon the bridging oxygen rows, and the result was strongly related to the study of ammonia in Chapter 6. Indeed, the bright spots corresponded to hydrogen atoms on the bridging oxygen rows, namely hydroxyl-like species were imaged. However, it was noted that the character of the hydroxyl-like species was not similar to conventional hydroxyls, or rather it exhibited the converse nature as far as the adsorption of ammonia was concerned. As a matter of fact, the chemisorption of ammonia was obstructed by the presence of hydroxyl-like species near the five-fold coordinated Ti sites. In this meaning, this expression as "hydroxyl-like" may not be correct. But the most important things involved in these studies in Chapters 6 and 8 was that the Lewis acidity of $TiO_2(110)$ was expected to be controllable by the coverage of hydrogen atoms, i.e. electron exposure and exposure of hydrogen atoms to the surface. The proof was not offered in this thesis, but the experiments to confirm this expectation were not seemed to be difficult.

In view of technical aspects of STM, the thesis also contributed much to the progress of surface science. First, it was demonstrated that even single physisorbed molecule can be imaged at room temperature under UHV conditions. In general, the physisorbed molecule was interacted very weakly with the surface, therefore it was believed that a cooling procedure of the sample surface was needed for suppression of thermal diffusion process of molecule. In this case, the oxygen-protruded ridges may play a role of suppression of thermal diffusion process of molecule, the physisorbed pyridine, 2, 6-dimethylpyridine, benzene (not stated), and 4-methylpyridine were successfully imaged in STM images. In particular, the topographic feature of the flat lying and the upright geometries of 4-methylpyridine were identified. That was useful to classify into the physisorbed and chemisorbed species of 4-methylpyridine on the surface. The thesis also proved that STM had a potential of uncovering new or overlooked surface reactions. The ultimate resolution of STM promised the presence of further unexpected reaction like a treasure for advancing and developing the surface science and catalytic chemistry. Furthermore, such study will give insight for more establishments and understanding "science for the next 21st century" with getting over boundaries of finely divided science fields.

Acknowledgment

All the studies in my doctor thesis have been carried out at the Department of Chemistry, Graduate School of Science, the University of Tokyo during 1995-1999 under supervision of Prof. Y. Iwasawa. I wish to express my greatest gratitude to Prof. Iwasawa for his guidance, valuable discussions, and suggestions. I would like to make a grateful acknowledgment to Dr. H. Onishi, the project leader in Kanagawa Academy of Science and Technology for his constructive suggestions, fruitful discussions, and helpful encouragement throughout my work. I could not have been done my work without him. I also greatly appreciate Dr. K. Fukui for his invaluable advice, instructive discussions, and continual encouragement. Special acknowledgement is made to Assistant Prof. T. Sasaki for his kind advice and warm encouragement. I deeply appreciate Prof. K. Asakura in Hokkaido University for his helpful advice, heartwarming encouragement, and thoughtfulness. Also, I am grateful to Dr. T. Shido for his warm and helpful encouragement.

I am grateful to all the member of Iwasawa Lab. including alumni, Post Doctor fellows, and visiting scientists for their kind encouragement and valuable advice on my work, especially Prof. T. Oyama, Prof. Y. Yuen, Dr. E.M. Gaigneaux, Dr. R. Mulukutla, Dr. H. Liu, Dr. A. Kozlov, Dr. A. Kozlova, Dr. T. Inoue, Dr. T. Sueyoshi, Dr. K. Okumura, Dr. W.-J. Chun, Dr. Y. Yamaguchi, Dr. T. Kubota, Dr. K. Tomishige, and Dr. N. Ichikuni. Also, I thank all the staffs in the Department of Chemistry for their technical and official supports.

Finally, I sincerely thank my parents and my younger brother for their warmth and continual encouragement.